THESE DE L'UNIVERSITE DE LYON
Délivrée par
L'UNIVERSITE CLAUDE BERNARD LYON 1
ECOLE DOCTORALE
Interdisciplinaire Sciences-Santé
Pour l'obtention du
DIPLOME DE DOCTORAT
(Arrêté du 7 août 2006)

Olivia Monica SIGOVAN

Superparamagnetic iron oxide based nanoparticles in atherosclerosis detection and characterization by high resolution magnetic resonance imaging

JURY :

Dr Florence GAZEAU	Rapporteur
Pr Jean-Baptiste MICHEL	Rapporteur
Pr Philippe DOUEK	Examinateur
Dr Nicolas PROVOST	Examinateur
Dr Philippe ROBERT	Examinateur
Pr David SALONER	Examinateur
Pr Emmanuelle CANET-SOULAS	Directeur de thèse

UNIVERSITE CLAUDE BERNARD - LYON 1

Président de l'Université   **M. le Professeur L. Collet**

Vice-président du Conseil Scientifique   M. le Professeur J-F. Mornex

Vice-président du Conseil d'Administration   M. le Professeur G. Annat

Vice-président du Conseil des Etudes et de la Vie Universitaire M. le Professeur D. Simon

Secrétaire Général   M. G. Gay

COMPOSANTES SANTE

Faculté de Médecine Lyon Est – Claude Bernard   Directeur : M. le Professeur J. Etienne

Faculté de Médecine Lyon Sud – Charles Mérieux   Directeur : M. le Professeur F-N. Gilly

UFR d'Odontologie   Directeur : M. le Professeur D. Bourgeois

Institut des Sciences Pharmaceutiques et Biologiques   Directeur : M. le Professeur F. Locher

Institut des Sciences et Techniques de Réadaptation   Directeur : M. le Professeur Y. Matillon

Département de Formation et Centre de Recherche en Biologie   Directeur : M. le Professeur P. Farge
Humaine

COMPOSANTES SCIENCES ET TECHNOLOGIE

Faculté des Sciences et Technologies   Directeur : M. Le Professeur F. Gieres

UFR Sciences et Techniques des Activités Physiques et Sportives Directeur : M. C. Collignon

Observatoire de Lyon   Directeur : M. B. Guiderdoni

Institut des Sciences et des Techniques de l'Ingénieur de Lyon   Directeur : M. le Professeur J. Lieto

Institut Universitaire de Technologie A   Directeur : M. le Professeur C. Coulet

Institut Universitaire de Technologie B   Directeur : M. le Professeur R. Lamartine

Institut de Science Financière et d'Assurance   Directeur : M. le Professeur J-C. Augros

Institut Universitaire de Formation des Maîtres   Directeur : M R. Bernard

Table of Contents

French Summary

Résumé Français

En raison de ses performances, l'imagerie par résonance magnétique (IRM) est une méthode de choix pour les investigations cardiovasculaires non-invasives. Cette technique offre une image anatomique du système cardiovasculaire avec une bonne résolution spatiale et temporelle grâce aux avancements techniques et au développement des nouvelles séquences d'imagerie et des systèmes de synchronisation. De plus, l'utilisation d'agents de contraste ciblés ou non, permet une approche moléculaire et fonctionnelle.

Les maladies cardiovasculaires représentent la principale cause de mortalité dans les pays développés. L'athérosclérose est une maladie artérielle complexe et diffuse, dont l'inflammation est reconnue comme un dénominateur commun d'évolution maligne. La détection *in vivo* de l'inflammation est alors essentielle dans le diagnostic et le suivi thérapeutique. Une approche fonctionnelle pour la caractérisation de l'inflammation et en particulier des macrophages dans la plaque d'athérosclérose est l'administration intraveineuse des agents de contraste à base de nanoparticules superparamagnétiques d'oxyde de fer (USPIO).

Le besoin clinique est de suivre l'évolution de cette inflammation et de pouvoir en donner un score, une forte inflammation étant liée à un risque accru de rupture de plaque. Par conséquent, l'objectif des nombreuses études précliniques, réalisé sur des modèles animaux, est le développement et la caractérisation d'agents de contraste et de protocoles d'imagerie permettant ce suivi. Il est maintenant bien reconnu que l'inflammation dans la plaque d'athérosclérose accroît le risque de rupture et thrombose, mais les techniques permettant d'évaluer *in vivo* de manière non-invasive l'état inflammatoire sont limitées.

Les travaux présentés ici s'inscrivent dans cette thématique. L'objectif de la thèse a été le développement et l'optimisation de protocoles d'imagerie par résonance magnétique dédiés à l'application des agents de contraste superparamagnétiques au diagnostic de l'inflammation dans la plaque d'athérosclérose.

Cette thèse débute par un chapitre d'introduction qui est suivi par l'exposé de la recherche effectuée, où les travaux sont présentés dans cinq chapitres sous forme de manuscrits, publié ou soumis en vue de publication à des journaux scientifiques. La présentation des résultats de la recherche est structurée sur deux grands axes : le premier regroupe des travaux sur l'évaluation et optimisation des protocoles d'imagerie pour la détection et la caractérisation des agents de contraste superparamagnétiques (deux chapitres),

et le deuxième concerne l'application de ces techniques à l'IRM cardiovasculaire (trois chapitres).

Le premier chapitre de la thèse est structuré en deux parties. L'objectif de la première partie est d'introduire l'athérosclérose, l'application biomédicale de ces travaux ; la deuxième section offre une vue générale sur les nanoparticules à base d'oxyde de fer avec une discussion détaille sur leur utilisation comme agents de contraste pour l'IRM et sur l'état de l'art des techniques d'IRM employées pour leur détection caractérisation dans le domaine cardiovasculaire.

La détection des particules superparamagnétiques est généralement réalisée à l'aide des séquences d'imagerie en écho de gradient (GE), compte tenu des propriétés magnétiques de ces agents de contraste. Deux voies différentes basées sur les séquences écho de gradient peuvent être explorées pour détecter la présence des nanoparticules dans les tissus et essayer de quantifier la teneur tissulaire. Dans les images obtenues, les voxels avoisinants les particules magnétiques présentent une forte diminution du signal : c'est le contraste T2* caractéristique, appelé aussi contraste négatif. La mesure de T2* (temps de relaxation transversale apparent) représente la première voie. Plusieurs limitations peuvent être identifiées dans les techniques de cartographie par IRM, comme la nécessité d'une méthode capable d'évaluer une large gamme de concentrations de fer, telle que celles trouvées dans l'inflammation vasculaire.

Récemment, des techniques d'imagerie ont été développées qui permettent de conserver le signal de ces voxels. Ces techniques de 'contraste positif' permettent d'obtenir un nouveau type de contraste basé sur l'effet de susceptibilité magnétique des particules et sont obtenues en modifiant des séquencés classiques écho de gradient (GE) et écho de spin (SE). L'importance de ce type de séquences par rapport aux techniques T2* standard est leur capacité potentielle d'améliorer la sensibilité de détection des agents de contraste. Elles ouvrent aussi une nouvelle direction pour la quantification de la concentration tissulaire des particules.

Le deuxième chapitre s'inscrit dans cette dernière, et présente l'application d'une séquence de contraste positif. La séquence choisie a été décrite par Seppenwolde et al. (2003) et appliqué ensuite par V. Mani et al. (2006) sous le nom de « GRASP » à l'imagerie des agents superparamagnétiques. Afin de conserver le signal, le gradient local induit par le perturbateur magnétique est compensé par la modification de l'amplitude du gradient de

rephasage de coupe d'une séquence classique. Cette séquence a été comparée avec une séquence en contraste négatif dans le cadre d'un suivi de 3 jours après l'administration du nouveau produit dans le muscle de la cuisse chez la souris.

La variation du contraste mesuré dans les images au cours du temps a été différente entre les deux séquences, ce qui indique que le contraste positif peut être dans certains contextes plus efficace pour la visualisation et la caractérisation des particules dans leur environnement biologique.

Le troisième chapitre décrit une quantification *in vitro* de différentes concentrations des particules en état libre. Compte tenu du fait que les propriétés des USPIO sont mieux exploitées avec des séquences GE en pondération T2*, la stratégie utilisée a été le calcul des cartographies T2*. Les images ont été acquises avec une séquence GE qui permet d'utiliser des temps d'écho en dessous de la milliseconde grâce a l'imagerie 3D et à l'acquisition partielle de l'espace de k. L'étude a été réalisée sur des imageurs corps entier à trois champs différents. Les cartographies ont été établies à partir des images acquises en augmentant TE avec des incréments croissants jusqu'à une valeur finale de 50 ms, utilisant un ajustement exponentiel des intensités du signal. Les mesures ont été réalisées pour l'agent de contraste utilisé dans toute la partie d'application biologique ; il s'agit d'un USPIO (ultrasmall superparamagnetic iron oxide) développé par le Laboratoire Guerbet (Paris, France) avec un diamètre de la particule hydratée de 21 nm et un rapport de relaxivité r2/r1 de 2,53 mesuré dans l'eau à 0.47T (données commerciales, Guerbet). La relaxivité transversale R2* (1/T2*) montre une dépendance linéaire avec la concentration dans la gamme explorée (allant jusqu'à 8.55 µM Fe). Cette gamme de concentrations est retrouvée dans les applications *in vivo* chez l'animal.

La suite des travaux de recherche (chapitres IV, V et VI) présentent l'application de l'IRM haute résolution à la détection et le suivi de l'inflammation vasculaire dans l'athérosclérose. Il est maintenant connu que les nanoparticules superparamagnétiques de petite taille (USPIO, diamètre de la particule hydratée < 50 nm) sont des marqueurs d'inflammation. Dans l'application cardiovasculaire, ces particules vont être accumulées dans la paroi vasculaire rendue perméable par l'inflammation mais vont être aussi captées par cellules immunitaires, soit résidentes dans la paroi, soit dans le sang par des cellules qui migrent ensuite au niveau de la lésion. Les propriétés physico-chimiques des particules sont responsables de leur biodistribution et de leur efficacité de marquage.

Une contrainte dans l'utilisation des agents superparamagnétiques en clinique est le délai important entre l'administration du produit et l'imagerie post-contraste. Dans le cas du Ferumoxtran-10 (Sinerem®, Guerbet, France), l'imagerie est réalisée 24 heures après l'administration de la dose clinique, 45µM Fe/kg. En ce qui concerne les études précliniques, les doses administrées sont beaucoup plus importantes, du fait que la pharmacocinétique est différente entre l'homme et l'animal. Le Ferumoxtran-10 est administré habituellement chez l'animal à une dose de 1000µM Fe/kg et avec une fenêtre optimale d'imagerie post-contraste à 72 heures post administration.

Un USPIO caractérisé par une pharmacocinétique rapide (le P904) a été développé au Laboratoire Guerbet, Paris, pour essayer de s'affranchir de la contrainte présentée ci-dessus, l'hypothèse étant qu'une fenêtre précoce d'imagerie post-contraste sera disponible. Par conséquent l'objectif du quatrième chapitre a été l'évaluation du P904 dans la détection de l'inflammation vasculaire chez un modèle animal d'athérosclérose induite par chirurgie, le lapin Néo-Zélandais.

Nous avons réalisé les suivis post administration d'un produit standard (Sinerem®, Guerbet) et du nouveau produit, en utilisant un protocole IRM haute résolution multi-contraste, avec une pondération en densité de protons et en T2* et une séquence d'angiographie (MRA). Les résultats ont montré que le P904 induit un effet similaire à celui produit par le Sinerem, mais seulement 24 heures post administration, comparé aux 7 jours pour ce dernier. En effet, les deux produits vont être accumulés tôt dans les lésions inflammatoires, mais la forte concentration du Sinerem dans le sang, due à sa pharmacocinétique, induit un effet de susceptibilité magnétique très étendu qui empêche la visualisation de la paroi vasculaire.

La diminution de l'intervalle de temps entre le moment de l'administration de l'agent de contraste et l'imagerie est un facteur clé qui va influencer l'utilisation clinique des USPIO dans le diagnostic de l'athérosclérose.

Un autre modèle animal d'athérosclérose est la souris transgénique déficiente en apolipoprotéine E (ApoE$^{-/-}$) qui développe des lésions similaires à celles humaines. Une première étude a été réalisée sur ce modèle animal et fait l'objet du chapitre cinq de la thèse. L'objectif a été d'évaluer l'état inflammatoire de la paroi vasculaire au niveau de la crosse aortique en fonction du temps. Le P904 a été utilisé comme marqueur de l'inflammation avec la méthode de calcul développée dans le chapitre trois pour l'analyse d'image. La

performance du système de synchronisation, essentiel pour l'imagerie à ce niveau anatomique, a permis l'acquisition d'images de bonne qualité qui montrent un épaississement progressif de la paroi aortique jusqu'à des lésions hétérogènes avec une possible présence de calcifications. Ces observations sont soutenues par les résultats des cartographies T2* pré-contraste qui indiquent l'apparition des composantes avec des T2* plus courts. Les artefacts de susceptibilité dus à l'accumulation du fer dans la paroi ont montré un maximum au point d'imagerie à 16 semaines (âge des animaux) et une décroissance pour le restant du suivi, tendance trouvé pour la surface occupée par les macrophages suite à l'analyse histologique. La distribution des valeurs T2* post-contraste (48h) a été similaire entre le point d'imagerie à 10 semaines et le dernier point à 34 semaines ce qui indique une diminution de l'inflammation.

Cette étude a démontré la faisabilité de l'IRM avec USPIO dans le suivi de l'état inflammatoire lié à la progression temporelle de la plaque d'athérosclérose chez la souris transgénique.

Les connaissances acquises nous ont permis ensuite de réaliser une seconde étude sur le même modèle animal avec l'objectif d'évaluer un médicament anti-inflammatoire. Le protocole d'imagerie a été mis en place sur un imageur avec une intensité de champ plus élevée, 7T, qui a permis de gagner en intensité de signal. En plus, la sensibilité de détection de la technique de cartographie a été améliorée par l'utilisation d'un temps d'écho plus court (TE = 2,1 ms). Ce travail est présenté dans le sixième chapitre. Nous montrons que l'IRM haute résolution permet de suivre un effet inhibiteur sur la progression de la plaque chez des souris sous traitement pharmacologique. La mesure de T2* avant et après l'injection permet d'objectiver l'évolution de l'inflammation. Cependant, on peut noter dans certains cas une persistance du fer injecté lors du précédent examen dans les organes lymphoïdes, mais également dans la paroi vasculaire.

Le troisième manuscrit a été publié en *Radiology (August 2009), le* premier manuscrit est soumis pour publication dans *European Radiology*; le quatrième manuscrit est soumis en vue de publication dans *Investigative Radiology ;* le deuxième et le cinquième manuscrit vont être soumis.

D'autres études dans lesquelles les protocoles d'imagerie développées au cours de cette thèse ont été utilisés sont résumées brièvement en annexe à la fin du manuscrit.

Le protocole IRM développé et décrit dans le quatrième manuscrit a été utilisé pour étudier le ciblage de la plaque d'athérosclérose par des macrophages marqués magnétiquement administré en intraveineux chez la souris ApoE2.

Concernant la séquence de contraste positif, les expériences réalisées au niveau de la crosse aortique chez la souris ApoE$^{-/-}$ ont montrés que la méthode n'étais pas fiable dans cette localisation en raison de la petite taille de la paroi vasculaire et des artefacts de flux sanguin. Par contre, elle a été appliquée avec succès dans la détection et quantification des macrophages marquées magnétiquement injectées par stéréotaxie intracérébrale chez la souris.

Cette thèse a été réalisée au Laboratoire CREATIS-LRMN, Université Lyon1, dans le cadre d'un projet ANR, ″Inflam″. Une partie des travaux expérimentaux ont été réalisés au Laboratoire des Sciences Radiologiques (RSL), Lucas Center, Université Stanford, Etats-Unis, dans le cadre d'un projet de collaboration France-Stanford. Une étude clinique a été menée en parallèle à Lyon pour étudier l'inflammation dans la plaque carotidienne à l'aide d'agents de contraste standard et a été publiée dans *Journal of Magnetic Resonance Imaging*. Les travaux réalisés à Stanford sur des imageurs corps entier (1,5, 3 et 7 Tesla) entraient également dans cette stratégie de transfert clinique de nos protocoles.

Organization of the thesis

A state of the art introductory chapter is followed by the research work presented in five chapters written as manuscripts published or submitted for publication in scientific journals.

The first part of the introductory chapter will present a general view on atherosclerosis; the pathologic vessel wall will be portrayed along with the non-invasive imaging techniques that are commonly used to detect and characterize it. The second part will introduce superparamagnetic iron oxide based MR contrast agents ((U)SPIO); their physico-chemical properties, *in vivo* applications and effect on the MR signal will be thoroughly discussed with a focus on MR sequences adapted for these contrast agents in the cardiovascular field.

The research work studies are organized on two main axes. The goal of the first part of the experimental work was to evaluate and optimize MR imaging protocols for the detection and characterization of superparamagnetic iron oxide based contrast agents (two chapters). This is followed by the application of these methods to MRI of atherosclerosis, which represents the second part (three chapters).

For the detection and characterization of (U)SPIO two MR strategies were explored. Chapter II presents the implementation of a positive contrast imaging technique, called the "white marker" that enables a selective signal recovery from the voxels surrounding magnetic particles. This sequence was used for the detection of non-radioactive superparamagnetic nano-capsules designed for brachy-therapy.

The third chapter presents an *in vitro* quantification essay performed on a wide range of contrast agent concentrations that could be expected for *in vivo* applications. A short echo time (TE) sequence was used to calculate T2* of the different concentrations of free particles and magnetically labeled cells at three different magnetic fields.

The aim of the work presented in chapter IV was to evaluate the use of a new USPIO (P904, Guerbet, Paris, France) for MRI detection of vascular inflammation in a rabbit model of induced atherosclerosis.

The same contrast agent was than used in a study performed on a transgenic mouse model of atherosclerosis. The goal of this work, presented in chapter V, was to characterize

by USPIO-enhanced MRI the age related inflammatory status related to atherosclerosis lesion progression in ApoE$^{-/-}$ mice.

The advances in knowledge and the developed tools in our previous work allowed us to set the basis for a drug evaluation study. Chapter VI presents this follow up study, performed at a higher field strength on the same animal model and using the same contrast agent.

The first study was submitted for consideration in *European Radiology*, study three has been published in *Radiology (August 2009),* study four has been submitted for consideration in *Investigative Radiology* and studies two and five will be submitted.

The MRI protocol developed and reported in study four was used in a study of magnetically labeled cell tracking in atherosclerotic lesions. The purpose was to evaluate M1 macrophage recruitment in atherosclerosis after adoptive transfer of iron oxide-labeled macrophages in ApoE2 ki mice. This work is presented in Annex I. The manuscript has been submitted for consideration in *Investigative Radiology*.

The positive contrast sequence presented in the first study did not seem to be adapted for *in vivo* imaging of atherosclerosis in our experimental conditions. It has been however successfully applied for a quantification trial of magnetically labeled cells *in vivo* in the mouse brain. This study is presented in Annex II.

Part of the MRI protocol was transferred to the clinical 1.5 and 3T magnets for carotid plaque imaging. It was first optimized to evaluate plaque contrast in patients with a clinically approved contrast agent and published in *Journal of Magnetic Resonance Imaging* (Annex III).

This thesis was performed at the Lyon 1 University, in CREATIS-LRMN laboratory. Part of the work was conducted within the framework of an ANR project "Inflam". Another part was conducted in Stanford University in the framework of a France-Stanford collaboration program that funded the experiments.

The MRI sessions were conducted on two Bruker magnets, a 4.7T and a 7T, facilities of Créatis-LRMN at the University of Lyon1, Lyon and on three whole body GE magnets, 1.5T, 3T and 7T, facilities of The Lucas Center, Radiology Department, Stanford University, United States. The patient study was performed on a 1.5T Philips System with the Radiology Department of the Cardiovascular Hospital of Lyon. Histopathological analyses were performed by Guerbet, Paris and Genfit, Lille.

Chapter I

I. ATHEROSCLEROSIS

Cardiovascular disease is the leading cause of death worldwide. The atherothrombosis disease (atherosclerosis with its thrombotic complications) is a diffuse complex condition that involves the aorta, carotid and coronary arteries as well as the peripheral arteries (1). It is characterized by the thickening of the arterial wall to form an atherosclerotic plaque. Cholesterol deposition, oxidation, extracellular matrix, chronic inflammation and thrombus formation play major roles in triggering clinical manifestations. Very important advances in understanding the pathogenesis of atherosclerosis have been achieved during the last century (2).

In the beginning of this sub-chapter a short depiction of the normal vessel wall will be performed for an easier understanding of the pathological changes that will be discussed afterwards.

I.1 The arterial wall

A large artery consists of three morphologically distinct layers. The intima, the innermost layer, is bounded by a monolayer of endothelial cells on the luminal side and a sheet of elastic fibers, the internal elastic lamina, on the peripheral side. The anatomy of a normal artery is shown in Figure 1.
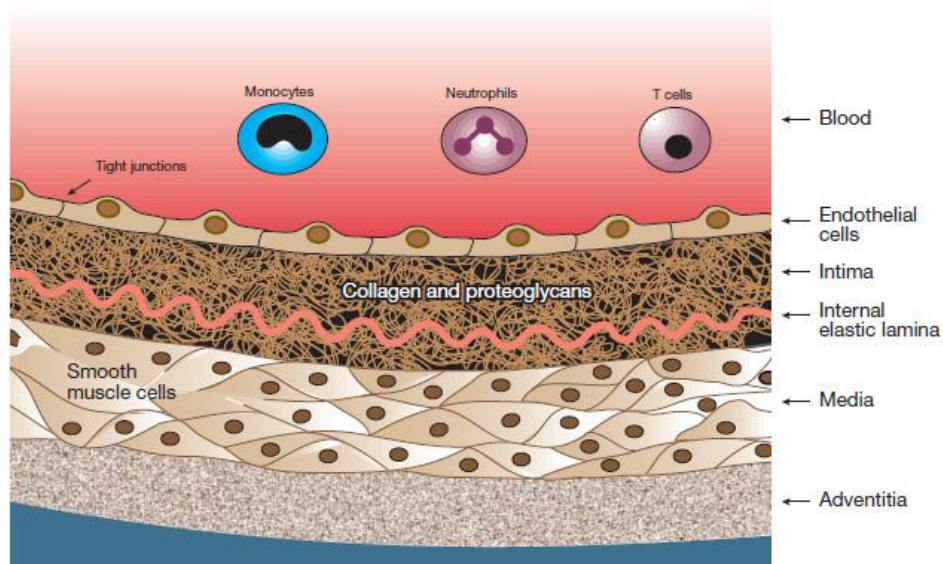

Figure I.1. *Simplified representation of the structure of a normal large artery. The proportion of the intima compared to the other layers is exaggerated. Reproduced from Lusis et al. Nature, 2000*

The normal intima is a very thin region and consists of extracellular connective tissue matrix, primarily proteoglycans and collagen and it has the main role in atherosclerosis formation. The media, the middle layer, consists of smooth muscle cells (SMCs) and also elastic fibers and collagen. The adventitia is the outer arterial layer and consists of connective tissue, fibroblasts and SMCs (3). The nourishment of the vessel wall is ensured by the vasa vasorum, or 'vessels of a vessel'. They form a network of micro-vessels that lies in the adventitia and can penetrate the outer media (4). The role of the connective tissue of the intima is to filter blood plasma that crosses the vessel and will reach the vasa vasorum after an exchange of metabolites and useful molecules. Among these useful molecules there are lipoproteins and free fatty acids, major source of energy for certain organs like the myocardium.

There are three types of lipoproteins: low density lipoproteins (LDL) containing 25% proteins, 20% triglycerides and 55% cholesterol; high density lipoproteins (HDL) containing 50% proteins, 37% triglycerides and 13% cholesterol and finally the very low density lipoproteins (VLDL) with 10% proteins, 65% triglycerides and the rest cholesterol.

The lipoproteins have been discussed since atherosclerosis is a progressive disease characterized by the accumulation of lipids and fibrous elements in the large arteries. Valuable information was obtained from studies in animal models that helped clarifying the events of atherosclerosis. Mice deficient in apolipoprotein E (apoE) or the LDL receptor develop advanced lesions and are the most often used models in genetic and physiological studies (5).

I.2 The phases of atherosclerosis

Atherosclerosis progression was studied intensively in animal models, usually involving a high fat, high cholesterol diet. The accumulation of lipoproteins is the first change observed in the arterial wall. After a few weeks, monocytes adhere to the surface of endothelial cells and will then transmigrate in the intima. Here they transform into macrophages, take up the accumulated lipoproteins and become foam cells. An important part of the necrotic core of lesions is formed by dead foam cells and their lipid content. The next step is the migration of some SMCs from the media into the intima where they will secrete fibrous elements. The result of this process is an increase in size of the lesion and transformation into fibrous plaques. The so called "shoulder" region of plaques represents a

weak point as mononuclear cells from the blood will continue to migrate through this region into the lesion (3). Also, plaque rupture usually occurs at this level.

Considering its location, magnitude and metabolic activity, the endothelium plays a pivotal role in maintaining vascular homeostasis by regulating vascular tone, smooth muscle cell proliferation, and the inflammatory and reparative responses to local injury. It was recognized that endothelial dysfunction is the promoter of atherosclerosis (6, 7). The disease progresses through lipid core expansion and macrophage accumulation at the edges of the plaque (1). Concerning the adventitia, its role of supportive tissue and nourishment provider for the other layers was reconsidered based on evidence gathered form animal model studies. The fibroblasts from this layer in conjunction with SMCs will proliferate, migrate and be involved in neointima formation and vascular remodeling (6).

A depiction of plaque formation and progression up to thrombosis can be seen in figure I.2.

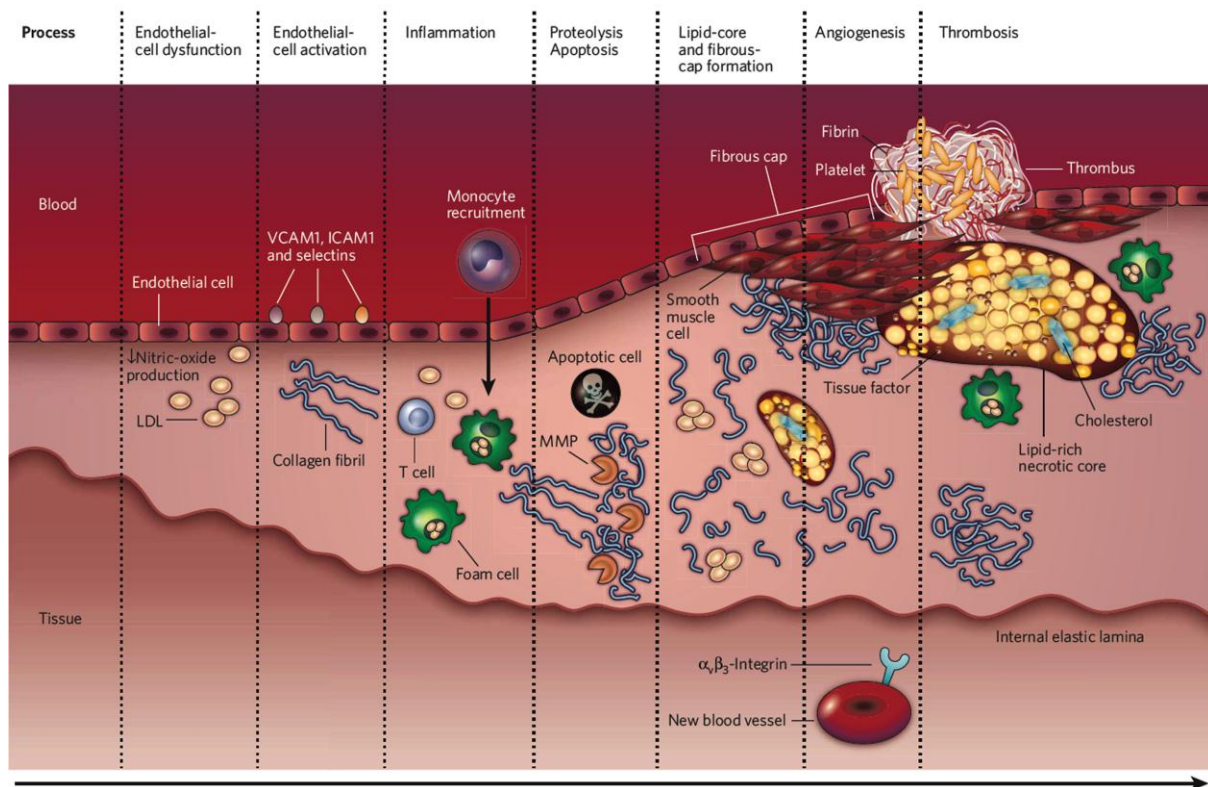***Figure I.2.*** *Depiction of the progression of an atherosclerotic lesion developing from a normal blood vessel (far left) to a vessel with an atherosclerotic plaque and superimposed thrombus (far right). Reproduced form Sanz et al., Nature, 2008*

I.3 Atherosclerosis lesion classification

The American Heart Association (AHA) Committee on Vascular Lesions set the criteria for lesion classification. Thus plaque progression can be subdivided into five phases, as described in the following paragraphs and figure I.3.
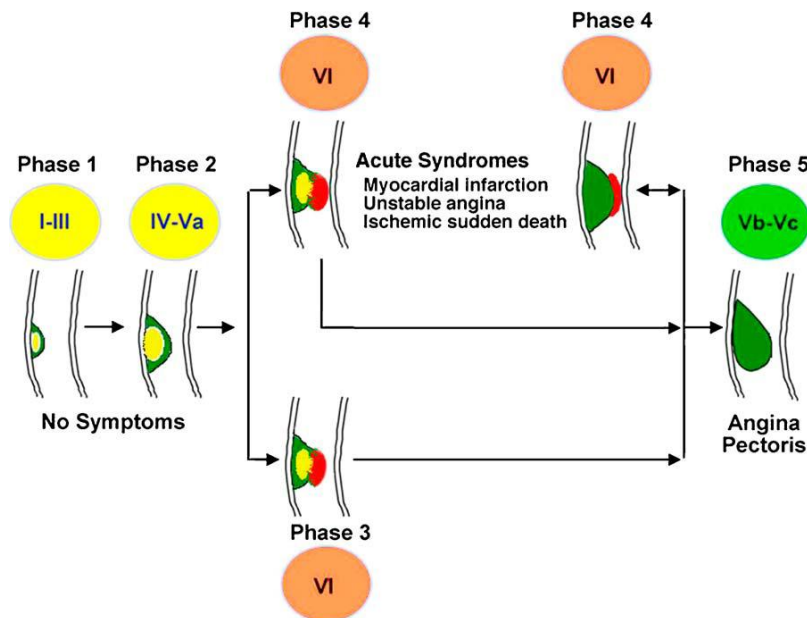

***Figure I.3**. Schematic representation of the different phases of atherosclerosis from asymptomatic lesions to symptomatic atherothrombosis. Reproduced from Corti el al., J Thromb Thrombolysis 2004.*

The early lesions of **Phase 1** are small and commonly seen in people under the age of 30. They are categorized into three types as follows: type I lesions, containing macrophage-derived foam cells (lipid droplets rich cells); type II lesions, contain macrophages, smooth-muscle cells and mild extracellular lipid deposits; finally, type III lesions, consist of smooth-muscle cells surrounded by extracellular connective tissue, fibrils and lipid deposits.

The advanced lesions are included in **Phase 2.** These lesions may be prone to rupture because of a high lipid content, increased inflammation and thin fibrous cap. They are categorized in two variants: type IV lesions, consisting of a high density of cells with a high amount of extracellular lipid intermixed with normal intima; or type Va lesions, characterized by an extracellular lipid core covered by a fibrous cap. Phase 2 plaques can evolve into the acute phases 3 and 4 and either of these can evolve in phase 5.

Phase 3 lesions are characterized by acute "complicated" type VI lesions, originating from ruptured (type IV and Va) or eroded lesions, and leading to mural, non-obstructive thrombosis. This process is clinically unapparent, but may lead to angina.

Phase 4 lesions are characterized by acute complicated type VI lesions, with fixed or repetitive occlusive thrombosis. This process becomes clinically apparent in the form of an acute coronary syndrome (ACS). About two-thirds of ACS are caused by occlusive thrombosis on a non-stenotic plaque, although in about one-third, the thrombus occurs on the surface of a stenotic plaque. In phases 3 and 4, changes in the geometry of ruptured plaques, as well as organization of the occlusive or mural thrombus by connective tissue, can lead to the occlusive or significantly stenotic and fibrotic plaques.

Finally, **Phase 5** lesions are characterized by type Vb (calcific) or Vc (fibrotic) lesions that may cause angina; however, if preceded by stenosis or occlusion with associated ischemia, the myocardium may be protected by collateral circulation and such lesions may then be clinically unapparent (1, 6).

Thus an outline of the main components of atherosclerotic plaques can be represented as follows: 1) connective tissue extracellular matrix, including collagen, proteoglycans, and fibronectin elastic fibers; 2) crystalline cholesterol, cholesteryl esters and phospholipids; 3) cells such as monocyte-derived macrophages, T-lymphocytes, and smooth-muscle cells; and 4) thrombotic material with platelets and fibrin deposition. Varying proportions of these components give rise to the spectrum of lesions seen above.

As it was mentioned in the lesion classification paragraph, symptoms occur late in the course of the disease. They are caused by the narrowing of the vascular lumen, which can be either a gradual phenomenon (a result of progressive plaque growth) or a sudden one (a result of plaque rupture and, subsequently, thrombosis) (2). The most common consequences are coronary heart disease and stroke; and the rupture of vulnerable plaques is responsible for these events. It is now well established that plaque vulnerability is linked mainly to plaque composition and not necessarily to the degree of luminal narrowing (8). When we talk about plaque stability, three parameters must be taken into account: the lipid core, the thickness of the fibrous cap and finally inflammation within the cap (9). Thus we can make the difference between a vulnerable, rupture-prone, plaque and a stable one. The vulnerable lesion presents a thin fibrous cap (thinner than 65μm) around a large lipid core and high macrophage infiltration.

The diagnosis of atherosclerosis used to be based on detecting a narrowing of the arterial lumen (stenosis) or evaluating the effect of stenosis on organ perfusion and it was only possible at advanced stages of disease. New imaging techniques currently allow the assessment of blood vessel morphology, luminal stenosis, plaque volume and composition

(2). These are invasive techniques such as x-ray angiography, intravascular ultrasound, angioscopy (visualization of the blood vessel lumen with a narrow bore flexible endoscope), still used to this day, present a potential risk related to post intervention complications such as bleeding or arterial dissection; and non invasive techniques like magnetic resonance imaging (MRI) and computed tomography (CT). CT provides a quantification of plaque size and some characterization of the composition. It is well suited for the study of any vascular territory and it has long been used for the detection of calcium deposits within the vessel wall. However, it requires potentially nephrotoxic contrast agents and ionizing radiations. The advantage of MRI over other techniques is that it provides information on plaque chemical composition and does not require iodine contrast agents or radiation.
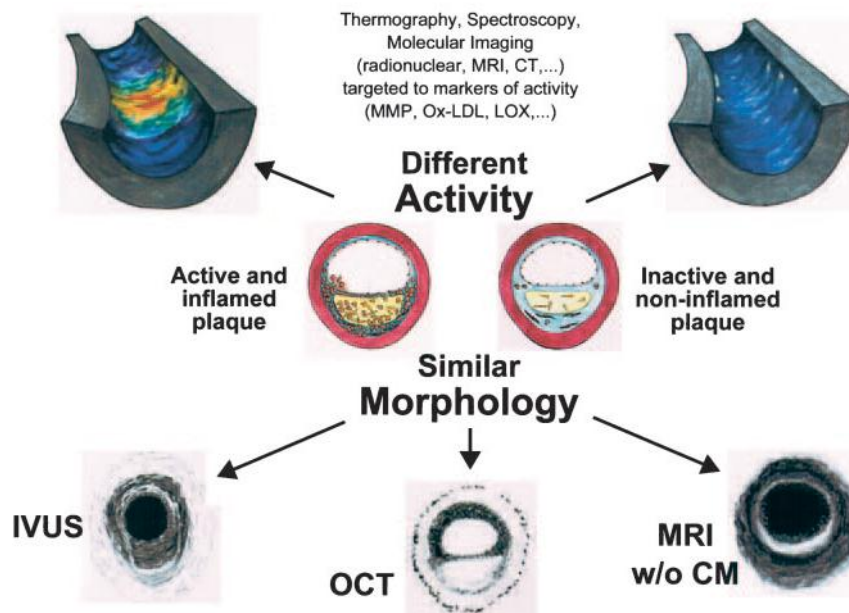

Figure I.4. Morphology and functional imaging, The importance of diagnostic methods capable of detecting activity is shown in the case where similar morphology can be found for lesions that are very different from a physiological view point. Reproduced from Naghavi et al., Circ. 2003 (IVUS – Intravascular ultrasound; OCT – Optical coherence tomography; MMP – Matrix metalloproteinase; Ox-LDL – oxidized low density lipoproteins)

Furthermore, it should be stated here that for a better detection of vulnerable patients (at high-risk of atherosclerosis related clinical events), plaque composition detection alone is not completely satisfactory. A case where plaques with similar morphologies are very different from an activity point of view is presented in figure I.4 (10). Research is directed towards imaging techniques capable of combining detection of plaque components and markers of inflammation, as these techniques will have an impact on patient-care strategies.

I.4 MR characteristics of atherosclerotic plaques and MR imaging techniques

The principle of MRI will be briefly discussed below. The MR examination is performed in the presence of a magnetic field. The proton spins of the water molecules will be aligned on the direction of this field and create a macroscopic magnetization. By applying one or more radio-frequency pulses, the net macroscopic magnetization of proton spins is perturbed out of its alignment parallel to the applied field. The MR image is obtained by collecting the signal of the relaxation back to the initial state using a radiofrequency coil. The relaxation back to equilibrium of the magnetization is governed by two exponential time constants: T1, longitudinal relaxation time, for the component along the *z* axis, and T2 the transverse relaxation time, for the component perpendicular to *z*. Thus, tissue components with short T1 values will be associated with higher signal intensities compared to those components that have longer T1 values on T1-weighted MR images. On what concerns the other time constant, short T2 values are associated with low signal intensities on T2-weighted MR images, since the magnetization available for detection is smaller.

The contrast of an MR image can be related to one of the time constants or to the proton density of tissue components. This is called image weighting and is obtained through manipulation of the MR sequence parameters such as the repetition time (TR) and echo time (TE). Atherosclerosis plaque components have different MR properties as described in Table 1. This is the basis of multi-contrast investigations that allow the non-invasive characterization of lesion types.

Table I.1. *Findings on MR imaging of plaque components*

Histological Features	Relative MR signal intensity		
	T1-Weighted	Proton Density Weighted	T2-Weighted
Fibrosis	Isointense	Isointense	Isointense
Calcification	Hypointense	Very Hypointense	Very hypointense
Lipid core	Hyperintense	Hyperintense	Hypointense
Thrombus	Variable	Variable	Variable

Note. Variable signal intensity may be related to thrombus age

An important number of studies both *ex vivo* (11-14) and *in vivo* (15-18) have proven the MR efficiency in differentiating between plaque components. The essential sequences for differentiating the four tissues in multi-contrast plaque characterization are T2-w spin echo

(SE) and T1-w gradient echo (GE) (16). The role of diffusion weighted imaging in differentiating between fibrous tissue, necrotic core and hemorrhage has been explored by Ronen et al., however this sequence is not currently used in routine carotid investigations (14). Intra-plaque hemorrhage is known to stimulate the progression of atherosclerosis and promote instability of carotid plaques. It has been shown that it can be accurately detected with the use of a 3D high resolution T1-w spoiled GE sequence (19). High spatial resolution sequences are generally combined with an angiography sequence in diagnosis protocols. Bright-blood techniques allow calcification visualization in the intima and assessment of fibrous cap thickness and integrity. It has been demonstrated by Hatsukami et al. that a time-of-flight (TOF) sequence enables differentiation between intact, thick or thin fibrous caps from ruptured fibrous caps in vivo in human carotid arteries (20).

Some important parameters need to be taken into account when considering and imaging protocol. One is spatial resolution that needs to allow a correct visualization of the investigated vessel and also the distinction between different plaque components. In vivo human plaque imaging is generally performed at a magnetic field of 1.5T and using a sub-millimeter pixel size and a slice thickness between 2 and 5 mm (21).

Another parameter is sequence gating that is essential for investigations of the thoracic region to avoid motion artifacts. Clinical sequences are gated on the patient's cardiac signal (EKG) and acquisitions are performed on breath hold or free breathing for the neck region. This parameter is important since it influences the total acquisition time and thus also the image weighting. Acquisition time needs to be kept at a minimum for patient comfort. The minimum TR given by the heart rate can prove to be too long for a correct T1 weighting (T1-w) in post-gadolinium imaging. A study aiming at rendering a high resolution T1-w sequence virtually heart rate-independent was performed with the Radiology Department of the Cardiovascular Hospital of Lyon on a 1.5T Philips System (22). This study is briefly described in the Annex Studies chapter.

Finally, for a better delineation of the vessel wall, preparation pulses are used to cancel the signal from fat and from blood. Black blood pulses perform a double inversion recovery (180°) where the first RF is non-spatially selective and is followed after a delay called inversion time (TI) by a second RF that will restore the signal of tissue only on the investigated slice. TI gives the null point of blood and is calculated based on its T1 as follows:

$$TI = T_{1blood} \cdot (\ln 2 - \ln[1 + \exp(-TR/T_{1blood})])$$

Other more complex preparation pulses have been investigated for black blood that also allow the investigation of a reduced field of view (FOV) (23-25).

Following today's tendency of going to higher field strengths in clinical practice special attention needs to be given to image interpretation. Differences were found in the measured size of particular regions, like calcifications, probably due to the increase of susceptibility effects (26). However, it has been shown that tissue contrast criteria developed at 1.5 T for carotid plaque interpretation are applicable at 3T (Figure I.5) and better SNR improves detection of plaque components.
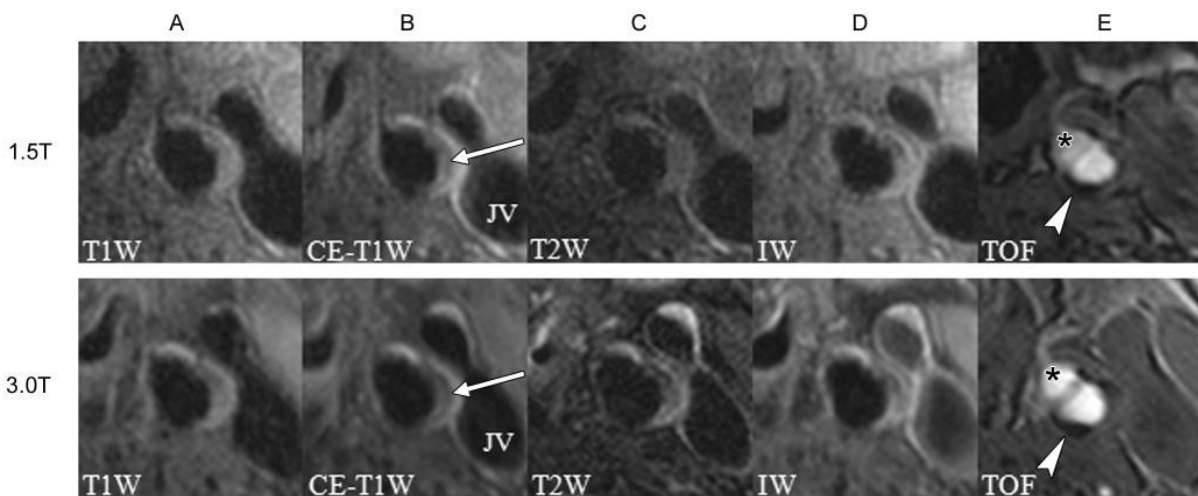

Figure I.5. Cross-sectional images of left carotid bifurcation (axial plane) acquired at 1.5 T (top) and 3.0 T (bottom). A lipid-rich necrotic core (column B, arrows) is visible owing to the decrease in signal intensity on the contrast-enhanced T1-w image (CE-T1-w) compared with that on the precontrast T1-w image and in surrounding fibrous tissue. Also to be noted, the isointense signal on the TOF image in this region is consistent with an absence of hemorrhage at this location; the superficial calcification (arrowheads, column E) present with both platforms, and a branching vessel (* in column E). IW – intermediate weighted, JV – jugular vein. Reproduced from Underhill et al., Radiology 2008

So far plaque characterization without contrast enhancement was discussed. However, commercially available gadolinium (Gd) based extracellular contrast are useful plaque characterization. It has been shown in patient studies that the administration of these agents improved differentiation of atherosclerotic tissue types compared with non-enhanced imaging (27, 28).

In the field of contrast agent use in atherosclerosis, one of the most exciting developments concerns the ability to detect specific targets, as for example immune cells, receptors on the cell surface or specific proteins. This is the field of molecular imaging.

Superparamagnetic iron oxide based contrast agents, originally developed for liver imaging, have shown to be an efficient inflammation marker for atherosclerosis. The

following subchapter is dedicated to a detailed presentation of this type of contrast agents and their application to atherosclerosis.

References:

1.   Fuster V, Moreno PR, Fayad ZA, et al. Atherothrombosis and high-risk plaque: part I: evolving concepts. J Am Coll Cardiol 2005; 46:937-954.

2.   Sanz J, Fayad ZA. Imaging of atherosclerotic cardiovascular disease. Nature 2008; 451:953-957.

3.   Lusis AJ. Atherosclerosis. Nature 2000; 407:233-241.

4.   Scotland RS, Vallance PJ, Ahluwalia A. Endogenous factors involved in regulation of tone of arterial vasa vasorum: implications for conduit vessel physiology. Cardiovasc Res 2000; 46:403-411.

5.   Tamminen M, Mottino G, Qiao JH, et al. Ultrastructure of early lipid accumulation in ApoE-deficient mice. Arterioscler Thromb Vasc Biol 1999; 19:847-853.

6.   Corti R, Hutter R, Badimon JJ, et al. Evolving concepts in the triad of atherosclerosis, inflammation and thrombosis. J Thromb Thrombolysis 2004; 17:35-44.

7.   Wu JC, Bengel FM, Gambhir SS. Cardiovascular molecular imaging. Radiology 2007; 244:337-355.

8.   Briley-Saebo KC, Shaw PX, Mulder WJ, et al. Targeted molecular probes for imaging atherosclerotic lesions with magnetic resonance using antibodies that recognize oxidation-specific epitopes. Circulation 2008; 117:3206-3215.

9.   Libby P. Molecular bases of the acute coronary syndromes. Circulation 1995; 91:2844-2850.

10. Naghavi M, Libby P, Falk E, et al. From vulnerable plaque to vulnerable patient: a call for new definitions and risk assessment strategies: Part I. Circulation 2003; 108:1664-1672.

11. Serfaty JM, Chaabane L, Tabib A, et al. Atherosclerotic plaques: classification and characterization with T2-weighted high-spatial-resolution MR imaging-- an in vitro study. Radiology 2001; 219:403-410.

12. Morrisett J, Vick W, Sharma R, et al. Discrimination of components in atherosclerotic plaques from human carotid endarterectomy specimens by magnetic resonance imaging ex vivo. Magn Reson Imaging 2003; 21:465-474.

13. Ronen RR, Clarke SE, Hammond RR, et al. Resolution and SNR effects on carotid plaque classification. Magn Reson Med 2006; 56:290-295.

14.   Ronen RR, Clarke SE, Hammond RR, et al. Carotid plaque classification: defining the certainty with which plaque components can be differentiated. Magn Reson Med 2007; 57:874-880.

15.   Yoshida K, Narumi O, Chin M, et al. Characterization of carotid atherosclerosis and detection of soft plaque with use of black-blood MR imaging. AJNR Am J Neuroradiol 2008; 29:868-874.

16.   Cappendijk VC, Cleutjens KB, Kessels AG, et al. Assessment of human atherosclerotic carotid plaque components with multisequence MR imaging: initial experience. Radiology 2005; 234:487-492.

17.   Hofman JM, Branderhorst WJ, ten Eikelder HM, et al. Quantification of atherosclerotic plaque components using in vivo MRI and supervised classifiers. Magn Reson Med 2006; 55:790-799.

18.   Yuan C, Mitsumori LM, Ferguson MS, et al. In vivo accuracy of multispectral magnetic resonance imaging for identifying lipid-rich necrotic cores and intraplaque hemorrhage in advanced human carotid plaques. Circulation 2001; 104:2051-2056.

19.   Bitar R, Moody AR, Leung G, et al. In vivo 3D high-spatial-resolution MR imaging of intraplaque hemorrhage. Radiology 2008; 249:259-267.

20.   Hatsukami TS, Ross R, Polissar NL, et al. Visualization of fibrous cap thickness and rupture in human atherosclerotic carotid plaque in vivo with high-resolution magnetic resonance imaging. Circulation 2000; 102:959-964.

21.   Fayad ZA, Fuster V. Clinical imaging of the high-risk or vulnerable atherosclerotic plaque. Circ Res 2001; 89:305-316.

22.   Boussel L, Herigault G, Sigovan M, et al. Modified electrocardiograph-triggered black-blood turbo spin-echo technique to improve T1-weighting in contrast-enhanced MRI of atherosclerotic carotid arteries. J Magn Reson Imaging 2008; 28:533-537.

23.   Yarnykh VL, Yuan C. T1-insensitive flow suppression using quadruple inversion-recovery. Magn Reson Med 2002; 48:899-905.

24.   Yarnykh VL, Yuan C. Multislice double inversion-recovery black-blood imaging with simultaneous slice reinversion. J Magn Reson Imaging 2003; 17:478-483.

25.   Yarnykh VL, Yuan C. Simultaneous outer volume and blood suppression by quadruple inversion-recovery. Magn Reson Med 2006; 55:1083-1092.

26.   Underhill HR, Yarnykh VL, Hatsukami TS, et al. Carotid plaque morphology and composition: initial comparison between 1.5- and 3.0-T magnetic field strengths. Radiology 2008; 248:550-560.

27. Yuan C, Kerwin WS, Ferguson MS, et al. Contrast-enhanced high resolution MRI for atherosclerotic carotid artery tissue characterization. J Magn Reson Imaging 2002; 15:62-67.

28. Wasserman BA, Smith WI, Trout HH, 3rd, et al. Carotid artery atherosclerosis: in vivo morphologic characterization with gadolinium-enhanced double-oblique MR imaging initial results. Radiology 2002; 223:566-573.

II. SUPERPARAMAGNETIC IRON OXIDE BASED CONTRAST AGENTS

Currently, contrast media are applied in approximately 30% of all MRI procedures. There is a dominance of extracellular, low molecular-mass Gd chelates such as Gd-DTPA (1). However, over the last 15 years, nanoparticulate superparamagnetic iron oxide based MR contrast agents have been the subject of intensive research. With their development an important field in MRI research was opened. Several different types of agents have been optimized for a wide range of applications; these include imaging of the liver and spleen (2), bone marrow, lymph node, vascular inflammation and MR angiography. Their biodistribution, pharmacokinetics, physicochemical and proton relaxation properties have been modified by altering the particle core size, by the choice of surface coating material and the surface charge (3, 4). The nanoparticles are taken up by the monocyte–macrophage system. This is why, if they are not entirely captured by the liver and spleen, they are widely evaluated as MRI markers for the diagnosis of inflammatory and degenerative disorders associated with high macrophage phagocytic activity (5).

It is noteworthy here that the use as contrast agents for this nanoparticulate system in only one of their many applications in the wide field of nanomedicine. Several review papers aimed at portraying their different medical applications (6-8). Four important applications stand out: (i) magnetic separation – separating specific biological entities from their biological environment, this involves a prior labeling with a magnetic material; (ii) drug delivery – a cytotoxic drug is attached to a biocompatible magnetic nanoparticle carrier, following the administration high-gradient magnetic fields are used to concentrate the complex at a specific target site with the aim of reducing the amount of systemic distribution of the cytotoxic drug and the dosage required for an efficient effect; (iii) hyperthermia treatments – the procedure involves heating magnetic particles that have been dispersed in a target tissue by applying an alternating magnetic field and is applied to cancer ablation; and (iv) MRI contrast enhancement.

In this work, only the role of MR contrast agent of superparamagnetic nanoparticles is considered. The term (U)SPIOs (ultrasmall) superparamagnetic iron oxide will be used when referring to the entire class of superparamagnetic iron oxide based contrast agents.

1.1 Synthesis of (U)SPIOs

A series of literature reviews have discussed the chemical aspects of superparamagnetic iron oxide nanoparticles synthesis and characterization, along with their biomedical

applications. A recent review by Laurent et al. offers a more complete view of (U)SPIOs as it includes greater emphasis on synthesis and characterization. These techniques, with details on the coprecipitation method are summarized in the paragraphs below.

(U)SPIOs consist of iron oxide crystals (diameter in the range 4-10 nm), such as magnetite (Fe_3O_4) and maghemite (γFe_2O_3), or other ferrites, insoluble in water (9). Ferrites are characterized by their saturation magnetization at 300 K (92 emug^{-1} for magnetite and 78 emug^{-1} for maghemite). Synthesis of superparamagnetic nanoparticles is a complex chemical process. The main challenge is to obtain a monodisperse size, since the properties of the nanoparticles strongly depend upon the dimension of the magnetic grains (10). Another great challenge is to optimize a process that can be easily performed on an industrial scale, without any complex purification procedures or the use of dangerous reactants and solvents.

Numerous chemical methods (microemulsions, sol-gel syntheses, sonochemical reactions, hydrothermal reactions, hydrolysis and thermolysis of precursors, flow injection syntheses and electrospray syntheses) can be used to synthesize magnetic nanoparticles for medical imaging applications. The classical synthesis of (U)SPIO agents involves the coprecipitation of iron oxide in an aqueous solution of ferrous and ferric salts. The formation can be written as follows:

$$Fe^{2+} + 2\ Fe^{3+} + 8OH^- \rightarrow Fe_3O_4 + 4\ H_2O$$

Magnetite (Fe_3O_4) is very sensitive to oxidation and is transformed into maghemite (γFe_2O_3) in the presence of oxygen, according to the following expression:

$$Fe_3O_4 + 2\ H^+ \rightarrow \gamma Fe_2O_3 + Fe^{2+} + 2\ H_2O$$
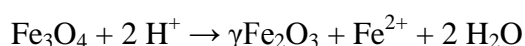
The advantage of the method is that large quantities can be synthesized; it is thus applied on an industrial scale for the synthesis of commercially available products. Although this classical coprecipitation method allows modification of the mean size of nanoparticles by adjusting pH, ionic strength, temperature, or the ratio of Fe(II) over Fe(III), control of particle size distribution is limited. Recently developed methods that will not be discussed here enable a more precise control of size dispersity, but are not yet applicable on an industrial scale (11).

After synthesis of the magnetic nanoparticle, coating is required to prevent destabilization and agglomeration of the colloid. There are several classes of stabilizers that can be used: inorganic materials (silica, gold), monomeric stabilizers (carboxylates, phosphates) (the contrast agent used in the experimental part, P904 Guerbet Laboratories, is included in this class) and polymer stabilizers (dextran, polyethylene glycol, polyvinyl alcohol, alginate, chitosan) (10). Superparamagnetic particles dedicated for *in vivo* use are generally coated with dextran and dextran derivatives thanks to their good biocompatibility.

However, other composites such as starch, albumin and arabinogalactan have been used (12). The biocompatible coating material allows a safe intravenous administration. The nature of the coating needs also to be optimized in order to prevent any aggregation and sedimentation of the superparamagnetic nanoparticle providing a stable solution for injection. Together with the geometric arrangement on the surface, the nature of the coating plays a significant role in pharmacokinetic and biodistribution properties (13).

Targeted nanoparticles, also called biovectors, capable of recognizing a biological target are obtained by functionalizing the nanoparticles with a specific ligand that must be grafted onto the surface of the coating. Generally used ligands are antibodies or their fragments, oligosaccharides, proteins, peptides and peptidomimetics. One protein target on the cellular surface is the alpha v beta 3 integrin ($\alpha_v\beta_3$) present in angiogenesis and malignant growth of tumors. Zhang et al. have demonstrated the efficiency of $\alpha_v\beta_3$ integrin–targeted ultrasmall superparamagnetic iron oxide particles (USPIOs) to label endothelial cells in a tumor model (14). E-selectin, expressed on the cellular surface in inflammatory conditions, is another target for molecular imaging. An anti-murine E-selectin monoclonal antibody, MES-1, was conjugated with ultrasmall superparamagnetic iron oxide (USPIO) nanoparticles and proved to be efficient in MR imaging of the activated vascular endothelium (15). Another more recent study showed efficient targeting of a pegylated USPIO grafted with an E-selectin ligand in an animal model of muscle inflammation (16).

Second generation targeted nanoparticles are obtained from cross-linked iron oxides (CLIO), nanoscale structures with dendritic arms that allow attachment of fluorescent labels, for example, creating a single contrast agent with optical and magnetic properties. The targeting ligands can be antibodies or enzyme substrates (17). Kang et al., have reported preliminary evidence of the feasibility of direct imaging of E-selectin by MR using targeted CLIO particles (18). Conjugation of annexin V to CLIO represents a strategy for the development of a MRI imaging probe for apoptosis detection (19). Small-molecule surface modification allowed the formation of a nanoparticle library that recognizes different cell types and also different physiological states of the same cell type based on cellular uptake. It comprises 146 nanoparticles decorated with different synthetic small ligands (20). It is clear that these targeted agents will have a tremendous impact on molecular imaging strategies; however they will not be further discussed here.

By using an appropriate anticancer drug in the synthesis formulation, therapeutic magnetic nanoparticles can be obtained. Recently, a radiopharmaceutical agent based on superparamagnetic nano-capsules containing non-activated Rhenium was synthesized by

Hamoudeh et al. for local radiation therapy and MRI detection (21, 22). The second study of the experimental part of this thesis presents a nano-capsulate system designed for local radiation therapy to which superparamagnetic crystals were added to render it visible by MRI.

II.2 Physicochemical properties of (U)SPIOs

Nanoparticles present a great scientific interest because they are the bridge between bulk materials and atomic or molecular structures. Compared to the bulk material of same composition, a nanoparticle has new and exciting size-dependent properties, such as the superparamagnetism in magnetic materials.

Different methods can be used to determine the 'sizes' characterizing nanoparticles: the size of the crystalline part of the core (ordered), the size of the whole iron core (ordered and disordered or amorphous part), of the shell and of the hydrated layer. Transmission electron microscopy (TEM) reports a mean value for the particle core and provides details on the size distribution and shape; this measurement has to be performed by image analysis on a statistically significant number of particles.
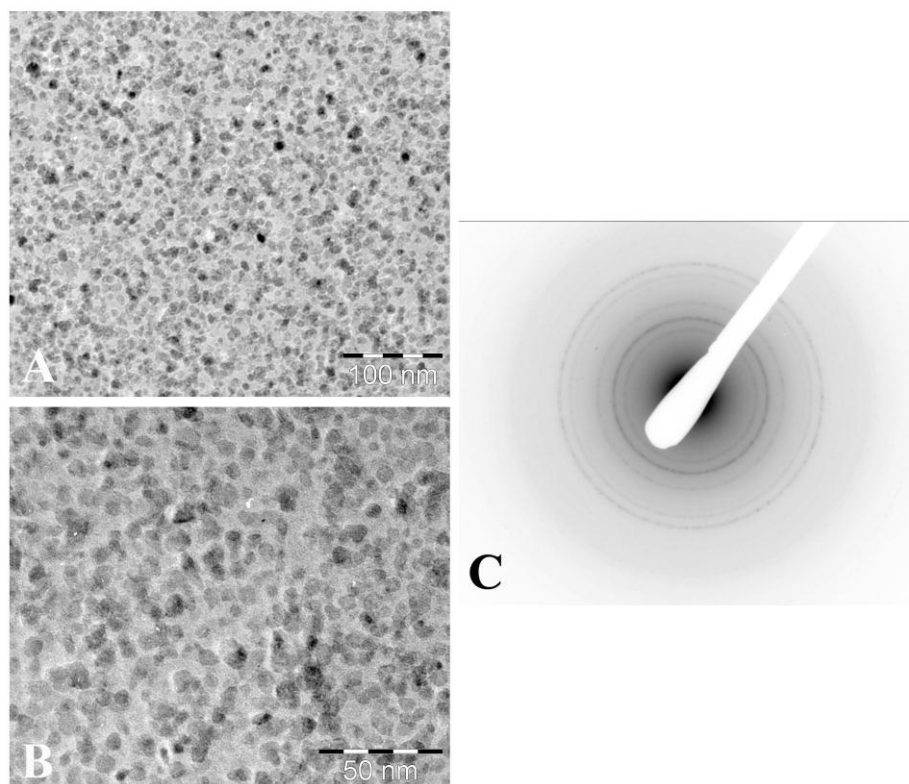

Figure II.1. *TEM images of P904 (USPIO, Guerbet Laboratory) showing a dispersion of nanoparticles with a mean size of 30 nm are presented in A (scale 100 nm) and B (scale 50 nm); C – diffraction pattern proving the crystalline nature of the nanoparticles. The TEM analysis was performed in LPMCN Laboratory, Lyon1 University*

An example of TEM images of a USPIO developed by Guerbet Research, obtained in the LPMCN Laboratory of Lyon1 University, is given in figure II.1. Performed in a high resolution mode (HRTEM), electron microscopy offers a view of the atomic arrangement. Furthermore, the diffraction mode will on one hand validate the crystalline nature of the iron oxide and on the other will give the space group symmetries in the crystal. The crystalline structure can also be obtained by X-ray diffraction (XRD). This technique enables the quantification of the iron oxide proportion formed in a mixture.

The *hydrodynamic diameter* is used to describe the total particle size, the iron oxide crystals with the coating material. This characteristic is measured by means of Photon Correlation Spectroscopy (PCS), also called Dynamic Light Scattering (DLS), a common technique to obtain the nanoparticle size (diffusion of light in a solution indicates the average particle sizes)(Table 1).

II.3 Classification of superparamagnetic iron oxide based contrast agents

As mentioned above and described in the next paragraph, the size of the particles is a major factor responsible for both biological and magnetic properties. Thus, iron oxide based contrast agents are generally divided into three groups depending on the mean particle diameter. The first one is the ultrasmall superparamagnetic iron oxide (USPIO) class and refers to mono-dispersed or mono-crystalline iron oxide particles with a diameter of less than 50 nm; superparamagnetic iron oxide (SPIO) corresponds to aggregated iron oxide cores and a mean particle diameter larger than 50 nm and the third group contains micron size particles (MPIO) (23, 24). The interest in using

Of these agents, the MPIO are used for cell labeling because they distort the magnetic field homogeneity creating high contrast effects larger than their size that can extend to a distance at least 50 times their physical diameter (25-27). Many of the SPIO and USPIO are either clinically approved or in trials, or at the experimental study stage. There are two kinds of SPIO agents, the large oral SPIO used for gastrointestinal imaging and smaller injectable colloidal suspensions. Two SPIO compounds are commercialized for intravenous use: dextran coated ferumoxides (Endorem® – Europe, Feridex® in the USA and Japan) and carboxydextran coated ferucarbotran (Resovist® – Europe and Japan), with liver tumours as clinical targets (13).

The prototype of USPIO was developed by Weissleder et al. in 1990 in the need of having particles small enough to be able to migrate across a capillary wall. That study proved the possibility of synthesizing particles in the size range of ~15 nm in order to increase their

half-life and without decreasing to much the relaxation properties. This opened the way for new medical applications such as lymphatic system and bone marrow imaging, brain and heart perfusion and even organ-targeted contrast agents (28). Several USPIO have been investigated in humans for several imaging applications, such as ferumoxtran-10 (dextran), VSOP (citrate) (29), feruglose (pegylated starch) or SHU555C (carboxydextran).

Table II.1. *Characteristics of iron oxide nanoparticles, that are commercially available or under clinical investigations. Relaxometric properties were measured at 1.5 T, 37 °C, in water or in plasma; the half-life is given for the clinical dose; the hydrodynamic size was obtained by laser light scattering. (Adapted from Corot et al., Advanced Drug Delivery Reviews 58 (2006) 1471–1504)*

Names	Company	Applications	Relaxometric properties 1.5 T $mM^{-1} s^{-1}$	T1/2 in human hours (μmol Fe/kg)	Coating agent	Hydrodynamic size (nm)
Ferumoxides AMI-25 Endorem®/Feridex®	Guerbet Advanced Magnetics	Liver imaging	$r_1 = 10.1$	2	Dextran T10	120–180
		Cellular labelling	$r_2 = 120$	(30)		
Ferumoxtran-10 AMI-227 BMS-180549 Sinerem®/Combidex®	Guerbet Advanced Magnetics	Metastatic lymph node imaging				
		Macrophage imaging	$r_1 = 9.9$	24–36		
		Blood pool agent	$r_2 = 65$	(45)	Dextran T10, T1	15–30
		Cellular labelling				
Ferumoxytol Code 7228	Advanced Magnetics	Macrophage imaging				
		Blood pool agent	$r_1 = 15$	10–14	Carboxylmethyl-dextran	30
		Cellular labelling	$r_2 = 89$	(18–74)		
Ferumoxsil AMI-121 Lumirem®/Gastromark®	Guerbet Advanced Magnetics	Oral GI imaging	n.a.	Oral	Silicon	300
Ferucarbotran SHU-555A Resovist®	Schering	Liver imaging	$r_1 = 9.7$	2.4–3.6	Carboxydextran	60
		Cellular labelling	$r_2 = 189$	(8–12)		
SHU-555C Supravist®	Schering	Blood pool agent	$r_1 = 10.7$	6		21
		Cellular labelling	$r_2 = 38$	(40)	Carboxydextran	
Feruglose NC100150 Clariscan®	GE-HC (abandoned)	Blood pool agent	n.a.	6 (36)	Pegylated starch	20
Ferristene Abdoscan®	GE-Healthcare	Oral GI imaging	n.a.	Oral	Sulphonated styrene–divinylbenzene copolymer	3500
VSOP-C184	Ferropharm	Blood pool agent	$r_1 = 14$	0.6–1.3	Citrate	7
		Cellular labelling	$r_2 = 33.4$	(15–75)		

II.4 In vivo application of (U)SPIO

The major drawback of clinically approved nonspecific Gd based agents is their massive and rapid extravasation in the interstitial space and their urinary excretion, as it limits their use for applications that require longer imaging sequences for higher spatial resolution. This can be overcome by increasing the agent's circulation time. USPIO agents together with large polymeric Gd chelates or small Gd chelates that express intravascular behavior by transient albumin binding show a slower clearance from the blood. These agents have in common a long elimination half-life; they are confined to the blood compartment and their body clearance is restricted (30).

Compared to other MR contrast agents, (U)SPIO toxicity is low. Also, the amount needed for clinical imaging is lower than the physiological iron stores.
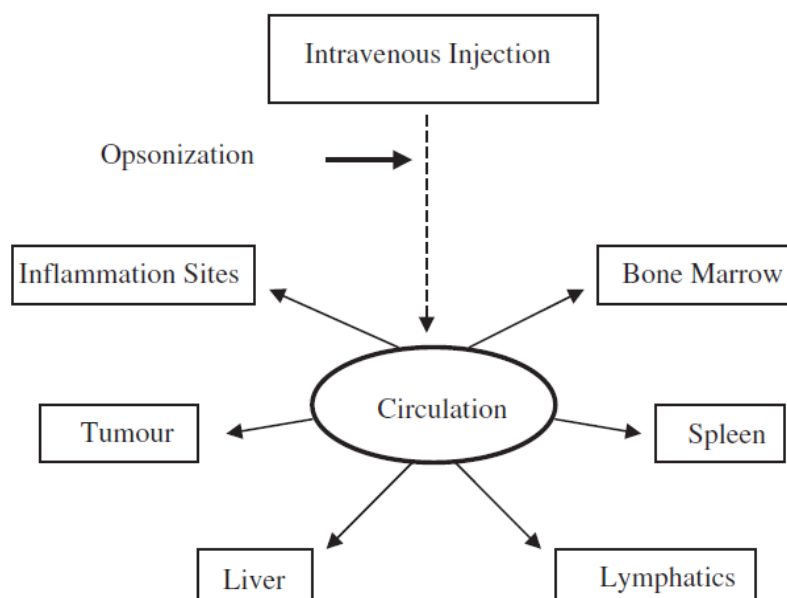

Figure II.2. The fate of nanoparticles after intravenous injection (31).

The different biological events taking place after (U)SPIO *in vivo* administration will be discussed hereafter. The pharmacokinetic properties characterise the circulation phase after their intravenous administration.

The first phenomenon that occurs immediately after injection in the blood stream is particle *opsonisation* (Figure II.2). This rapid coating with blood components, such as plasma proteins, is responsible for making the particles easily recognizable by the body's defences, the reticulo-endothelial system (RES) (31). Some coating materials have been designed to minimize or delay opsonisation (such is the case of PEG(poly-ethylene-glycol)-coated particles). Nanoparticles are usually taken up by macrophages and accumulated in the liver

(Kupffer cells), spleen and bone marrow, which are easily accessible macrophage-rich tissues. This is the second step and it leads to their elimination.

In addition to making them biocompatible, surface coating modifications may ensure a greater stability of the particles towards the RES. Particles having a slightly hydrophobic surface will be efficiently coated with proteins and thus will be rapidly removed from circulation. A hydrophilic surface will increase the blood clearance time (31).

Another strategy considered for longer circulation times (delayed recognition by the RES) is to decrease particle size. A recent study investigated the influence of particle size on the toxicity of metal oxides. Particle ability to cause cell death, mitochondrial damage, DNA damage and oxidative DNA lesions were evaluated after exposure of the human cell line A549. Nanoparticles of CuO were much more toxic compared to CuO micrometer particles and micrometer particles of TiO2 caused more DNA damage compared to the nanoparticles; however, in the case of iron oxides no clear difference was seen between the different particle sizes and showed overall low toxicity (32).

It has become common knowledge that particle size influences the cellular uptake of (U)SPIO, and thus cell labeling properties for cellular imaging. Consistent with previous studies on mice macrophage endocytosis (33), Sun et al., in an *in vitro* study performed on human mesenchymal fibroblasts (MSU), immortalized Lewis rat progenitor cells (LPC), and human epithelial derived hepatoma cells (HEP-G2), showed higher cell labeling efficiency of SPIO as compared with USPIO. Furthermore, both particle types showed a dose dependent uptake over more than 5 hours showing no toxicity in concentrations between 0.1 to 10 µmol Fe/ml (34). A higher labeling efficiency of human monocytes for SPIO (Endorem®, Guerbet) compared to USPIO (Sinerem®, Guerbet) was found by Engberink et al. in a more recent study (35). Although results indicate that SPIO is far more suitable for in vitro labeling of primary monocytes, the long blood pool half-life of USPIO makes it the most frequently used iron oxide for *in vivo* labeling in sites other than the liver or the spleen. The coating material also has an influence on cell internalization, as shown by the study of Berry et al. performed on magnetic nanoparticles synthesised and derivatised with dextran, compared to similar underivatised plain particles; their results indicated that both the uncoated and the dextran-derivatised particles were taken up by cells (human fibroblasts), however, the derivatised particles induced alterations in cell behaviour and morphology distinct from the plain particles. Membrane disruptions were far more pronounced in response to the later ones (36).

The long term outcome of (U)SPIO, once administered *in vivo* has not been intensively studied. *In vitro* studies performed on cell cultures have shown that the intracellular

metabolism depends on the chemical composition of the particles; for example Ferumoxtran-10 is degraded within 7 days inside macrophage lysosomes (13). The hypothesis is that the iron is incorporated in the red blood cell production and other natural uses of iron, like ferritin, and is eventually secreted from the body (3). Because of very different coating composition between the different iron oxide nanoparticles, their pharmacokinetic properties, biodistribution and metabolism can not be predicted by extrapolation from similar products.

II.5 Magnetic properties and effects on the MR signal

As mentioned before, the *superparamagnetism* is a size-dependant property of magnetic nanoparticles. This phenomenon occurs when crystals are smaller than a magnetic mono-domain, usually between 4 and 18 nm. When regions containing unpaired spins are sufficiently large that they can be considered single-domain particles and are named magnetic domains (3). The magnetic moments of magnetic domains reflect the interaction between individual unpaired electrons and the resultant moment is larger than that of a paramagnetic substance. The specific magnetic susceptibility of the particulate system exceeds that of the corresponding paramagnetic species because of the reordering of dipole moments in an applied magnetic field (37).

The crystalline nature of superparamagnetic nanoparticles is anisotropic; and as a consequence, the magnetic moment tends to align along privileged axes called axes of easy magnetization. At each time point, the magnetization is not zero, even in the absence of an external magnetic field. However, the magnetic moment jumps from one easy direction to another, which cancels the time-averaged magnetization. This magnetic fluctuation is called the Néel relaxation process and is characterized by a correlation time τ_N. When a static external field Bo is applied, the magnetic moment is forced to align with Bo and the correlation time τ_N has an infinite value (38). When the external magnetic field is removed, the magnetic moments of individual domains loose their collective orientation, thus the net magnetic moment becomes zero. Because superparamagnetic substances have no remnant magnetization, the (U)SPIO agents will not self-aggregate. This is an essential property for their *in vivo* application.

The principle of MRI has been briefly discussed in the previous subchapter and will be restated here for an easier understanding of contrast agent effects on the MR signal. The application of radio-frequency pulses will perturb the net macroscopic magnetization of proton spins out of its alignment parallel to the external field; the relaxation back to

equilibrium is governed by two exponential time constants: T1 (longitudinal relaxation time describing spin-lattice interactions) and T2 (transverse relaxation time describing spin-spin interactions). In the presence of magnetic inhomogeneities the transverse relaxation is governed by a shorter time constant, T2* (called the apparent transverse relaxation time). On T1-weighted MR images components with short T1 values will be associated with higher signal intensities compared to those components with longer T1 values. On T2-weighted images short T2 components are associated with low signal intensities, since the magnetization available for detection is smaller.

During relaxation, spins lose phase coherence between each other; rephasing them leads to the generation of an echo, used during image acquisition. There are two ways of obtaining an echo: by a refocusing 180° RF pulse and it is called a spin echo or by using gradients in which case it is called a gradient echo. The later method of image acquisition is sensitive to magnetic field inhomogeneities as spins under their influence are not being refocused, thus a T2* weighting is obtained.

(U)SPIO effects on signal intensity depend on various factors such as: particle composition and size, concentration of particles in the imaging voxel and sequence parameters.

The relaxivity defines the *efficiency* by which the contrast agent can accelerate the proton relaxation rate, as follows:

$$R_{1,2} = R_{1,2}^0 + r_{1,2} \cdot C$$

where $R_{1,2}$ (units s^{-1}) describe the longitudinal and transverse relaxation rates of protons in the presence of the contrast agent (respectively, $R_{1,2}^0$ are the relaxation rates in the absence of the contrast agent, $1/T_{1,2}$); C is the agents concentration (unit mM) and $r_{1,2}$ is the proportionality constant (units s^{-1}mM^{-1}) called relaxivity, a measure of how much the proton relaxation rate is increased per unit of concentration of contrast agent (4, 13). Relaxivity, $r_{1,2}$, is defined as the slope of the dependence of water relaxation rates on the concentration of the contrast agent (39).

The nuclear magnetic relaxation properties of a compound are ideally obtained by the study of its NMRD (nuclear magnetic resonance dispersion) profile. These curves give the relaxivity evolution versus the external magnetic field (10). Figure II.3 presents the NMRD

profile of an USPIO agent on a logarithmic scale. It can be observed that at clinical field intensities the longitudinal relaxivity decreases.
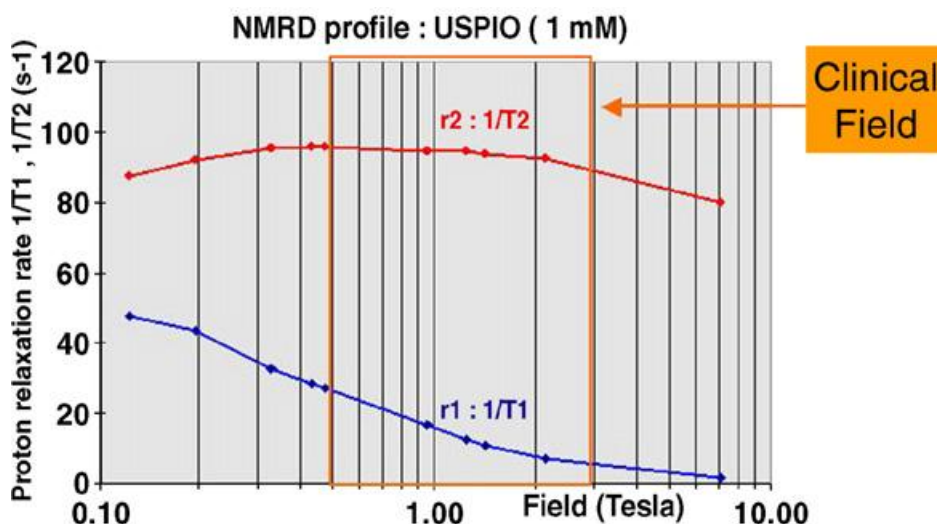

Figure II.3. *NMRD profile of an USPIO (Adapted from Corot C, Adv Drug Deliv Rev 2006; 58:1471-1504) (13)*

The theory of the (U)SPIOs induced relaxation mechanism is built upon the classical theory developed for paramagnetic systems. The inner-sphere contribution to the relaxation is minor and often completely negligible as compared to the dominant outer-sphere contribution. The relaxation of superparamagnetic particles after an RF excitation is governed by the Néel relaxation time that describes the reorientation of the electronic magnetic moment in the nanoparticle. The outer-sphere relaxation is produced by the movement of the water protons near the local magnetic field generated by the superparamagnetic particle. This magnetic field fluctuates because of the macromolecule motion and the relaxation induced by its presence is known as the Curie relaxation. Superparamagnetic crystals have a higher Curie relaxation than paramagnetic agents and the classical theory was modified to take it into account (40).

The interaction between proton spins and the magnetic moment is a dipolar interaction and its mechanism is modulated by a global correlation time (τ_C) that takes into account the Néel relaxation (τ_N) and relative diffusion of the magnetic particle and the water molecules described by the translational correlation time (τ_D): $1/\tau_C = 1/\tau_D + 1/\tau_N$. The dipolar interaction fluctuates because of the translational diffusion time of the water molecule and the Néel relaxation process. Thus in order for a fluctuation to be efficient and relax the protons, its correlation time must be shorter than the precession period of spins.

Nanoparticle aggregation has two consequences on proton relaxation. Firstly it concerns he geometry of the entire aggregate and the magnetic field induced by it (increasing R2*) and secondly it concerns the inner part of the aggregate (decreasing R1) (10). The increase of R2* is due to the so-called susceptibility effects that come from the magnetization difference (ΔM) between particles and tissue within a given voxel. R1 is decreased because the access of protons in the vicinity of the metallic component is restricted. Magnetic susceptibility is a constant that gives the effect of an applied magnetic field on the material's magnetization and its definition assumes a linear relationship between the two. However, under *in vivo* conditions the linearity in not fulfilled. Furthermore, this relationship between a magnetic field and the induced magnetization in the material can vary significantly for iron oxides depending on the size of the crystal core and aggregation. It is given by the Langevin function as follows: $M = Nm \cdot \left[\coth\left(\frac{\mu_0 mH}{kT} \right) - \left(\frac{kT}{\mu_0 mH} \right) \right]$, where N is the number of atoms per unit volume, m is magnetic moment per atom, k is the Boltzmann constant, μ_0 is the magnetic permeability of free space and T is the temperature in °K (4).

A Glossary of the terms introduced above is presented at the end of this subchapter.

II.6. (U)SPIOs dedicated imaging techniques in the Cardiovascular field

Dedicated imaging techniques currently used for (U)SPIOs imaging will be discussed below. The clinical cardiovascular field is expanding rapidly owing to new faster MR sequences that are able to provide better contrast between blood and tissue. As stated before, contrast agents are extensively used, but they are mostly Gd based products. However, given their special physico-chemical and pharmacokinetic properties, superparamagnetic nanoparticles have been proven efficient in a series of applications like vascular imaging, cardiac perfusion and viability and inflammation evaluation in the heart and atherosclerotic plaques.

Concerning vascular imaging, this was generally performed with sequences that use the motion of blood to obtain a higher signal in the vessels compared to the surrounding tissue (time of flight – TOF and phase contrast). The introduction of contrast agents opened the possibility to image vessels with slow or turbulent blood flow. Iron oxide nanoparticles have a higher T1 shortening effect, compared to Gd based agents (r_1 is generally 4-5 times higher), and they also have the advantage of prolonging this effect thanks to the longer blood half-life (30, 41-43). Furthermore the use of superparamagnetic particles has proved efficient in

increasing the signal to noise ratio in phase contrast imaging (44, 45). The fact that first-pass MRA is no longer performed because for longer circulation time, the venous system is also enhanced. This may be viewed as an inconvenient as well as an opportunity for diagnosis venous pathologies, like deep venous thrombosis (46-48). Thus, low doses of USPIO will induce a T1 effect and can be used for contrast enhanced MR angiography (CE-MRA) (49).

At higher doses, however, the benefit of increasing the T1 relaxation times might not be exploited fully because these agents simultaneously decrease the signal as a result of their pronounced T2 and T2* shortening effect (one order of magnitude higher than Gd based agents) especially when it is not possible to use minimal echo times (30). In applications, the intensity of the susceptibility effect depends on the tissue, on magnetization differences and on the type of the imaging sequence.

Studies evaluating the possibility of obtaining cardiac perfusion data have been reported on patients with coronary vessel disease using iron oxide particles. The advantage of USPIO over Gd agents is the fact there is no tissue leakage for nanoparticles. The T1 as well as the T2/T2* shortening effects can be used during first-pass of USPIO agents with a series of rapid sequences like T2-w spin-echo with echo-planar imaging (EPI) or T1-w fast low angle shot (FLASH) (50).

Weissleder et al. used iron oxide nanoparticles coupled with antimyosin to specifically target the infarcted cardiac muscle (51). This is one example, performed *ex vivo*, on tissue viability assessment with iron oxide. These studies are generally based on visualizing the distribution of the contrast agent in the infarct tissue. Special care needs to be taken when choosing the imaging sequences that should be optimized according to the expected T1 and T2/T2* effects that may not be detected if the sequence is not sensitive enough.

Finally, the application that represents the main topic of this thesis, vascular inflammation, will be discussed below. As stated previously the biodistribution of iron oxide nanoparticles is related to their size and coating material. Large particles (SPIO) are rapidly taken up by the reticulo-endothelial system (RES) in the liver and spleen, compared to the smaller ones (USPIO) that generally have longer circulation times. Owing to this property, smaller particles are more effectively accumulated in other parts of the body characterized by high macrophage activity. Vascular inflammation is translated by an increase of the permeability of the endothelium. Given these two phenomena, USPIO are found under two forms in inflamed atherosclerotic plaques: as free particles in the extracellular space and aggregated inside macrophages. The intra-cellular accumulation leads to a strong reduction of T2 and T2*.

Numerous preclinical (52-56) and clinical studies (57) have proven the efficiency of USPIO in the assessment of atherosclerosis. The sequences generally used are angiography, T1-w spin echo and T2*-w gradient echo sequences. Regions of signal loss on the T2*-w post-contrast images were proven to be related to iron accumulation in the vessel wall as detected on slides. The combination between a blood T1 effect and a T2* signal loss in the vessel wall offers a clear view of the spatial extent of vascular lesions. This strategy has been tested and is presented in the third manuscript of the thesis (58).

The basic strategy for atherosclerosis assessment is the evaluation of the contrast variation or of the size of the susceptibility artefact induced by iron accumulation. However, given the high magnetic moment of iron oxide nanoparticles, other strategies based on the traditional, susceptibility sensitive, gradient echo sequence can be considered for this application.

One strategy is the use of so called *'positive contrast' sequences* that enable the preservation of the MR signal of spins that are in the proximity of magnetic field perturbers. Due to their high magnetic moment, superparamagnetic iron oxide nanoparticles will induce in their environment local magnetic field gradients that are responsible for a Larmor frequency shift of the surrounding spins and also for a rapid intravoxel dephasing. The positive contrast methods are compensating for these effects in order to conserve the signal of spins surrounding the magnetic nanoparticles. This can be achieved in several different ways that will be reviewed in the following lines. Three main strategies seem to have been considered: compensation of the local gradient field with a modified GE sequence, off-resonance excitation with specially designed RF pulses and data post-processing. In the scientific literature, the gradient compensation method has been described as the most robust compared to the others (59). The slice rephasing gradient of a standard GE sequence is modified to take into account the amplitude of the local magnetic inhomogeneity and compensate for it. Thus only spins that are under the influence of the local magnetic inhomogeneity will be refocused and appear bright on the MR image (60-63). It is also known as the 'White marker' technique and it has been implemented on the scanners in our laboratory and tested for different applications. A study of radio-therapeutic superparamagnetic particles detection where this method is compared to the standard one is presented in the second manuscript of the thesis. Another method developed by Cunningham et al. uses two spectrally selective RF pulses to excite and refocus spins that have a precise frequency shift compared to on-resonance water protons (64). This method, originally non-spatially selective has been improved with the addition of a novel RF pulse that enables slice

selection (65). The IRON technique, developed by Stuber et al. is based on the saturation of on-resonance water (Inversion Recovery with ON-resonant water suppression) (66). The post-processing techniques use the information in the k space (complex data, phase data or the susceptibility induced echo shift) to obtain positive contrast images. An example of positive contrast images obtained with the different techniques is presented in figure II.4. The susceptibility gradient mapping (SGM) is based on the calculation of the positive contrast image from complex data acquired with a standard 3D GE sequence using a 1D FFT over a subset of neighbouring voxels to obtain the echo shift in a certain spatial dimension (67).
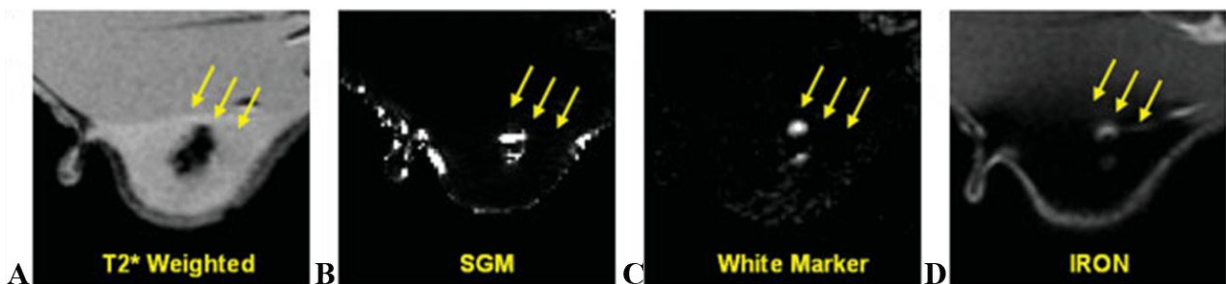

Figure II.4. Axial image series acquired with a standard T2*-w sequence (A), the susceptibility gradient mapping (SGM) (B), the white marker (C) and the IRON (D) techniques on a rat model with a SPIO-labeled tumour (10 mm in diameter) representing relatively diluted SPIO nanoparticles (yellow arrows) (59)

The other strategy is to use *quantitative MRI techniques* to measure relaxation times. The use of these methods is equally interesting for obtaining pre-contrast tissue parameters. Recently, a report on non-contrast enhanced MR T2* mapping in patients showed the possibility of distinguishing between plaques that produce symptoms from asymptomatic ones using the susceptibility of local iron found under different aggregation forms (68). Several *in vitro* quantification essays (69, 70) have shown a linear relationship between iron concentration and measured relaxation times. The challenge is to adapt these methods to *in vivo* conditions. As stated above in the contrast agent theory paragraph, this linear relationship no longer holds in these conditions. The number of reports of the application of quantification MRI to animal models as well as to human studies is very low. Plaque T2* values are only starting to be investigated. A study performed recently by Klug et al. reports *ex vivo* T2* mapping performed on samples taken from ApoE-/- mice at different intervals post-USPIO administration (71). One recent report performed on patients sought to define the optimum post-imaging time after USPIO (Sinerem®, Guerbet, France) administration using T1 and T2* weighted imaging and T2* measurements; maximum changes were found in the 36 – 48h period (72). In both studies only normalized T2* values are reported.

The application of the pixel by pixel T2* mapping on a mouse model of atherosclerosis has been investigated in two studies one performed at 4.7T and the other at 7T and the results are presented in manuscripts four and five of the thesis.

Gathering more knowledge on the effects of (U)SPIO on the MR signal will lead to the improvement of dedicated imaging techniques.

Glossary of terms

Magnetic Susceptibility	A property of materials that describes their response to an applied magnetic field
Diamagnetism	The property of a material which causes the creation of a very weak magnetic field in opposition with the applied external magnetic field
Paramagnetism	It produces a magnetization proportional to and in the same direction as the applied external field. It is stronger than diamagnetism
Ferromagnetism	It creates very high magnetization in the presence of an external magnetic field, that could be a few orders of magnitude larger than the applied field
Superparamagnetism	It appears in very small ferromagnetic materials (when regions containing unpaired spins are sufficiently large that they can be considered single-domain particles named magnetic domains). The magnetic moments of magnetic domains reflect the interaction between individual unpaired electrons and the resultant moment is larger than that of a paramagnetic substance
Magnetic domain	Describes the region in which the magnetic fields of atoms are grouped together and aligned (uniform magnetization)
Magnetic Relaxation Process	The return back to equilibrium of nuclear spins over a period of time after the perturbation of the system. It is due to interactions between spins.
Inner-sphere relaxation	Concerns the direct exchange of energy between protons and electrons located in the first hydratation sphere of the paramagnetic ion. This direct exchange is dominated by dipolar and scalar coupling of the spins. The dipolar coupling is described by correlation times (longitudinal and transverse) as follows: $1/\tau_{Ci} = 1/\tau_R + 1/\tau_M + 1/\tau_{si}$ *(i = 1,2)*, where τ_R represents the time of the rotation of the paramagnetic centre, τ_M is the residence time of water molecules in the first hydratation sphere, and finally τ_{S1} and τ_{S2} are the electron relaxation times (longitudinal and transverse) of the electronic spin associated with the paramagnetic ion. In the case of superparamagnetic particles τ_{Si} is the Néel relaxation time.
Outer-sphere relaxation	This relaxation is produced by the movement of the water protons near the local magnetic field gradients generated by the paramagnetic ion. The interaction between proton spins and the magnetic moment is also a dipolar interaction. The mechanism is characterized by the translational correlation time

	(τ_D) that takes into account the relative diffusion (D) of the paramagnetic centre and the solvent molecule, as well as their distance of closest approach (d): $\tau_D = d^2 / D$
Néel relaxation	Represents the reorientation of the magnetic moment within the superparamagnetic particles
Curie relaxation	Represents the relaxation due to the local field induced by paramagnetic and superparamagnetic particles in their environment in the presence of an external field.
Correlation time	Represents the time between fluctuations in the local magnetic field experienced by a spin due to molecular motions
Spin-lattice relaxation (T1 - longitudinal)	Magnetic relaxation in which the excess potential energy (absorbed from the RF radiation) of protons in a magnetic field is transferred to the surrounding tissue (lattice)
Spin-spin relaxation (T2 – transverse)	Magnetic relaxation in which the excess potential energy (absorbed from the RF radiation) of protons in a magnetic field is redistributed among the spins

References

1. Rohrer M, Bauer H, Mintorovitch J, et al. Comparison of magnetic properties of MRI contrast media solutions at different magnetic field strengths. Invest Radiol 2005; 40:715-724.

2. Ferrucci JT, Stark DD. Iron oxide-enhanced MR imaging of the liver and spleen: review of the first 5 years. AJR Am J Roentgenol 1990; 155:943-950.

3. Wang YX, Hussain SM, Krestin GP. Superparamagnetic iron oxide contrast agents: physicochemical characteristics and applications in MR imaging. Eur Radiol 2001; 11:2319-2331.

4. Bjornerud A, Johansson L. The utility of superparamagnetic contrast agents in MRI: theoretical consideration and applications in the cardiovascular system. NMR Biomed 2004; 17:465-477.

5. Corot C, Petry KG, Trivedi R, et al. Macrophage imaging in central nervous system and in carotid atherosclerotic plaque using ultrasmall superparamagnetic iron oxide in magnetic resonance imaging. Invest Radiol 2004; 39:619-625.

6. Pankhurst QA, Connolly J, Jones SK, et al. Applications of magnetic nanoparticles in biomedicine. J. Phys. D: Appl. Phys. 2003; 36:R167–R181.

7. Mornet S, Vasseur S, Grasset F, et al. Magnetic nanoparticle design for medical diagnosis and therapy. Journal of Material Chemistry 2004; 14:2161-2175.

8. Ito A, Shinkai M, Honda H, et al. Medical application of functionalized magnetic nanoparticles. J Biosci Bioeng 2005; 100:1-11.

9. Bonnemain B. Superparamagnetic agents in magnetic resonance imaging: physicochemical characteristics and clinical applications. A review. J Drug Target 1998; 6:167-174.

10. Laurent S, Forge D, Port M, et al. Magnetic Iron Oxide Nanoparticles: Synthesis, Stabilization, Vectorization, Physicochemical Characterizations, and Biological Applications. Chem Rev 2009.

11. Modo MM, Bulte JWM. Molecular and Cellular MR Imaging: Taylor & Francis Group, LLC, 2007.

12. Gupta AK, Naregalkar RR, Vaidya VD, et al. Recent advances on surface engineering of magnetic iron oxide nanoparticles and their biomedical applications. Nanomed 2007; 2:23-39.

13. Corot C, Robert P, Idee JM, et al. Recent advances in iron oxide nanocrystal technology for medical imaging. Adv Drug Deliv Rev 2006; 58:1471-1504.

14. Zhang C, Jugold M, Woenne EC, et al. Specific targeting of tumor angiogenesis by RGD-conjugated ultrasmall superparamagnetic iron oxide particles using a clinical 1.5-T magnetic resonance scanner. Cancer Res 2007; 67:1555-1562.

15. Reynolds PR, Larkman DJ, Haskard DO, et al. Detection of vascular expression of E-selectin in vivo with MR imaging. Radiology 2006; 241:469-476.

16. Radermacher KA, Beghein N, Boutry S, et al. In vivo detection of inflammation using pegylated iron oxide particles targeted at E-selectin: a multimodal approach using MR imaging and EPR spectroscopy. Invest Radiol 2009; 44:398-404.

17. Thrall JH. Nanotechnology and medicine. Radiology 2004; 230:315-318.

18. Kang HW, Josephson L, Petrovsky A, et al. Magnetic resonance imaging of inducible E-selectin expression in human endothelial cell culture. Bioconjug Chem 2002; 13:122-127.

19. Schellenberger EA, Bogdanov A, Jr., Hogemann D, et al. Annexin V-CLIO: a nanoparticle for detecting apoptosis by MRI. Mol Imaging 2002; 1:102-107.

20. Weissleder R, Kelly K, Sun EY, et al. Cell-specific targeting of nanoparticles by multivalent attachment of small molecules. Nat Biotechnol 2005; 23:1418-1423.

21. Hamoudeh M, Al Faraj A, Canet-Soulas E, et al. Elaboration of PLLA-based superparamagnetic nanoparticles: characterization, magnetic behaviour study and in vitro relaxivity evaluation. Int J Pharm 2007; 338:248-257.

22. Hamoudeh M, Fessi H, Mehier H, et al. Dirhenium decacarbonyl-loaded PLLA nanoparticles: influence of neutron irradiation and preliminary in vivo administration by the TMT technique. Int J Pharm 2008; 348:125-136.

23. Shen T, Weissleder R, Papisov M, et al. Monocrystalline iron oxide nanocompounds (MION): physicochemical properties. Magn Reson Med 1993; 29:599-604.

24. Bulte JW, Brooks RA, Moskowitz BM, et al. Relaxometry and magnetometry of the MR contrast agent MION-46L. Magn Reson Med 1999; 42:379-384.

25. Shapiro EM, Skrtic S, Sharer K, et al. MRI detection of single particles for cellular imaging. Proc Natl Acad Sci U S A 2004; 101:10901-10906.

26. Shapiro EM, Skrtic S, Koretsky AP. Sizing it up: cellular MRI using micron-sized iron oxide particles. Magn Reson Med 2005; 53:329-338.

27. Shapiro EM, Sharer K, Skrtic S, et al. In vivo detection of single cells by MRI. Magn Reson Med 2006; 55:242-249.

28. Weissleder R, Elizondo G, Wittenberg J, et al. Ultrasmall superparamagnetic iron oxide: an intravenous contrast agent for assessing lymph nodes with MR imaging. Radiology 1990; 175:494-498.

29. Taupitz M, Schnorr J, Abramjuk C, et al. New generation of monomer-stabilized very small superparamagnetic iron oxide particles (VSOP) as contrast medium for MR angiography: preclinical results in rats and rabbits. J Magn Reson Imaging 2000; 12:905-911.

30. Corot C, Violas X, Robert P, et al. Comparison of different types of blood pool agents (P792, MS325, USPIO) in a rabbit MR angiography-like protocol. Invest Radiol 2003; 38:311-319.

31. Berry CC, Curtis AS. Functionalisation of magnetic nanoparticles for applications in biomedicine. Journal of Physics D: Applied Physics 2003; 36:R198-R206.

32. Karlsson HL, Gustafsson J, Cronholm P, et al. Size-dependent toxicity of metal oxide particles--a comparison between nano- and micrometer size. Toxicol Lett 2009; 188:112-118.

33. Raynal I, Prigent P, Peyramaure S, et al. Macrophage endocytosis of superparamagnetic iron oxide nanoparticles: mechanisms and comparison of ferumoxides and ferumoxtran-10. Invest Radiol 2004; 39:56-63.

34. Sun R, Dittrich J, Le-Huu M, et al. Physical and biological characterization of superparamagnetic iron oxide- and ultrasmall superparamagnetic iron oxide-labeled cells: a comparison. Invest Radiol 2005; 40:504-513.

35. Oude Engberink RD, van der Pol SM, Dopp EA, et al. Comparison of SPIO and USPIO for in vitro labeling of human monocytes: MR detection and cell function. Radiology 2007; 243:467-474.

36. Berry CC, Wells S, Charles S, et al. Cell response to dextran-derivatised iron oxide nanoparticles post internalisation. Biomaterials 2004; 25:5405-5413.

37. Bean CP. Hysteresis loops of mixtures of ferromagnetic micropowders. Journal of Applied Physics 1955; 26:1381-1383.

38. Bulte JW, Kraitchman DL. Iron oxide MR contrast agents for molecular and cellular imaging. NMR Biomed 2004; 17:484-499.

39. Lauffer RB. Paramagnetic metal complexes as water proton relaxation agents for NMR imaging: theory and design. Chem Rev 1987; 87:901-927.

40. Roch A, Muller RN, Gillis P. Theory of proton relaxation induced by superparamagnetic particles. J. Chem. Phys. 1999; 110:5403–5411.

41. Clarke SE, Weinmann HJ, Dai E, et al. Comparison of two blood pool contrast agents for 0.5-T MR angiography: experimental study in rabbits. Radiology 2000; 214:787-794.

42. Loubeyre P, Zhao S, Canet E, et al. Ultrasmall superparamagnetic iron oxide particles (AMI 227) as a blood pool contrast agent for MR angiography: experimental study in rabbits. J Magn Reson Imaging 1997; 7:958-962.

43. Nolte-Ernsting C, Adam G, Bucker A, et al. Abdominal MR angiography performed using blood pool contrast agents: comparison of a new superparamagnetic iron oxide nanoparticle and a linear gadolinium polymer. AJR Am J Roentgenol 1998; 171:107-113.

44. Tanimoto A, Yuasa Y, Hiramatsu K. Application of superparamagnetic iron oxide (AMI-227) for 3D phase-contrast MR angiography. Acad Radiol 1998; 5 Suppl 1:S113-115.

45. Tanimoto A, Yuasa Y, Hiramatsu K. Enhancement of phase-contrast MR angiography with superparamagnetic iron oxide. J Magn Reson Imaging 1998; 8:446-450.

46. Schmitz SA, Albrecht T, Jensen K, et al. [Superparamagnetic iron oxide enhanced MR angiography of the portal vein system]. Rofo 2000; 172:51-54.

47. Hoffmann U, Loewe C, Bernhard C, et al. MRA of the lower extremities in patients with pulmonary embolism using a blood pool contrast agent: initial experience. J Magn Reson Imaging 2002; 15:429-437.

48. Larsson EM, Sunden P, Olsson CG, et al. MR venography using an intravascular contrast agent: results from a multicenter phase 2 study of dosage. AJR Am J Roentgenol 2003; 180:227-232.

49. Thomas Allkemper MCB, MD Lars Matuszewski, MD Wolfgang Ebert, PhD Peter Reimer, MD. Contrast-enhanced Blood-Pool MR Angiography with Optimized Iron Oxides: Effect of Size and Dose on Vascular Contrast Enhancement in Rabbits. Radiology 2002; 223:432-438.

50. Panting JR, Taylor AM, Gatehouse PD, et al. First-pass myocardial perfusion imaging and equilibrium signal changes using the intravascular contrast agent NC100150 injection. J Magn Reson Imaging 1999; 10:404-410.

51. Weissleder R, Lee AS, Khaw BA, et al. Antimyosin-labeled monocrystalline iron oxide allows detection of myocardial infarct: MR antibody imaging. Radiology 1992; 182:381-385.

52. Schmitz SA, Coupland SE, Gust R, et al. Superparamagnetic iron oxide-enhanced MRI of atherosclerotic plaques in Watanabe hereditable hyperlipidemic rabbits. Invest Radiol 2000; 35:460-471.

53. Ruehm SG, Corot C, Vogt P, et al. Magnetic resonance imaging of atherosclerotic plaque with ultrasmall superparamagnetic particles of iron oxide in hyperlipidemic rabbits. Circulation 2001; 103:415-422.

54. Schmitz SA, Taupitz M, Wagner S, et al. Magnetic resonance imaging of atherosclerotic plaques using superparamagnetic iron oxide particles. J Magn Reson Imaging 2001; 14:355-361.

55. Schmitz SA, Winterhalter S, Schiffler S, et al. USPIO-enhanced direct MR imaging of thrombus: preclinical evaluation in rabbits. Radiology 2001; 221:237-243.

56. Priest AN, Ittrich H, Jahntz CL, et al. Investigation of atherosclerotic plaques with MRI at 3 T using ultrasmall superparamagnetic particles of iron oxide. Magn Reson Imaging 2006; 24:1287-1293.

57. Kooi ME, Cappendijk VC, Cleutjens KB, et al. Accumulation of ultrasmall superparamagnetic particles of iron oxide in human atherosclerotic plaques can be detected by in vivo magnetic resonance imaging. Circulation 2003; 107:2453-2458.

58. Sigovan M, Boussel L, Sulaiman A, et al. Rapid-clearance iron nanoparticles for inflammation imaging of atherosclerotic plaque: initial experience in animal model. Radiology 2009; 252:401-409.

59. Liu W, Dahnke H, Jordan EK, et al. In vivo MRI using positive-contrast techniques in detection of cells labeled with superparamagnetic iron oxide nanoparticles. NMR Biomed 2008; 21:242-250.

60. Seppenwoolde JH, Viergever MA, Bakker CJ. Passive tracking exploiting local signal conservation: the white marker phenomenon. Magn Reson Med 2003; 50:784-790.

61. Mani V, Briley-Saebo KC, Hyafil F, et al. Feasibility of in vivo identification of endogenous ferritin with positive contrast MRI in rabbit carotid crush injury using GRASP. Magn Reson Med 2006; 56:1096-1106.

62. Mani V, Briley-Saebo KC, Itskovich VV, et al. Gradient echo acquisition for superparamagnetic particles with positive contrast (GRASP): sequence characterization in membrane and glass superparamagnetic iron oxide phantoms at 1.5T and 3T. Magn Reson Med 2006; 55:126-135.

63. Briley-Saebo KC, Mani V, Hyafil F, et al. Fractionated Feridex and positive contrast: in vivo MR imaging of atherosclerosis. Magn Reson Med 2008; 59:721-730.

64.   Cunningham CH, Arai T, Yang PC, et al. Positive contrast magnetic resonance imaging of cells labeled with magnetic nanoparticles. Magn Reson Med 2005; 53:999-1005.

65.   Balchandani P, Yamada M, Pauly J, et al. Self-refocused spatial-spectral pulse for positive contrast imaging of cells labeled with SPIO nanoparticles. Magn Reson Med 2009; 62:183-192.

66.   Stuber M, Gilson WD, Schar M, et al. Positive contrast visualization of iron oxide-labeled stem cells using inversion-recovery with ON-resonant water suppression (IRON). Magn Reson Med 2007; 58:1072-1077.

67.   Dahnke H, Liu W, Herzka D, et al. Susceptibility gradient mapping (SGM): a new postprocessing method for positive contrast generation applied to superparamagnetic iron oxide particle (SPIO)-labeled cells. Magn Reson Med 2008; 60:595-603.

68.   Raman SV, Winner MW, 3rd, Tran T, et al. In vivo atherosclerotic plaque characterization using magnetic susceptibility distinguishes symptom-producing plaques. JACC Cardiovasc Imaging 2008; 1:49-57.

69.   Kuhlpeter R, Dahnke H, Matuszewski L, et al. R2 and R2* mapping for sensing cell-bound superparamagnetic nanoparticles: in vitro and murine in vivo testing. Radiology 2007; 245:449-457.

70.   Brisset JC, Desestret V, Marcellino S, et al. Quantitative effects of cell internalization of two types of ultrasmall superparamagnetic iron oxide nanoparticles at 4.7 T and 7 T. Eur Radiol 2009.

71.   Klug K, Gert G, Thomas K, et al. Murine atherosclerotic plaque imaging with the USPIO Ferumoxtran-10. Front Biosci 2009; 14:2546-2552.

72.   Tang TY, Patterson AJ, Miller SR, et al. Temporal dependence of in vivo USPIO-enhanced MRI signal changes in human carotid atheromatous plaques. Neuroradiology 2009; 51:457-465.

Chapter II

Positive contrast with therapeutic iron nanoparticles at 4.7T

Positive Contrast with Therapeutic Iron Nanoparticles at 4.7T

M. Sigovan[1], M. Hamoudeh[2], A. Al Faraj[1], H. Fessi[2], E. Canet-Soulas[1]

1. Université Lyon-1, CREATIS-LRMN, UMR CNRS 5220, U630 INSERM, Lyon, France.

2. Université Lyon-1, Pharmaceutics and Pharmaceutical Technology Department, LAGEP, Laboratoire d'Automatique et de Génie de Procédés, UMR CNRS 5007, CPE-Lyon, Faculté de Pharmacie Lyon1, France

ABSTRACT:

The biocompatible and biodegradable properties of magnetic nanoparticles (SPIO) are expected to enable inclusion of specific molecules for drug delivery purposes, thus combining a therapeutic action with the diagnostic approach. Positive contrast techniques can potentially improve the sensitivity of iron detection compared to standard T2* methods. The gradient compensation technique was tested at a magnetic field of 4.7 T in a preliminary *in-vitro* and an *in-vivo* study to evaluate the contrast induced by therapeutic iron nanoparticles. The method was shown to be effective at this intermediate field strength. The combined negative and positive contrast protocol allowed good quality images to be obtained, enabling good characterization for *in-vivo* SPIO location and microenvironmental follow-up.

Key words: Superparamagnetic iron oxide, positive contrast, gradient compensation

INTRODUCTION

Superparamagnetic iron oxide particles (SPIOs) are extremely strong contrast enhancers for proton MR imaging (1). They have shown various *in-vivo* biodistribution and contrast effects depending on their size and coating. Furthermore, biocompatible and biodegradable properties are expected to enable specific molecules to be included in nanospheres, for drug delivery purposes with numerous clinical applications. In oncology, a brachytherapy type approach can be considered by incorporating specific neutron-activatable complexes that will allow local radiation treatment. With the addition of iron particles to such nanosystems, the magnetic properties will ensure a MRI delivery follow up (2).

The preferred method for iron oxide particle detection is gradient echo (GE) imaging. Inherent sensitivity to static field inhomogeneities, however, causes image distortion and signal loss due to dephasing between intravoxel spins (3). For voxels in magnetically uniform regions, signal intensity is maximal at the center of the k-space; for voxels under the influence of local magnetic gradients, however, the signal peak shifts. Thus, a conventional GE T_2^*-weighted image centered in k-space will show signal loss regions (4). Numerous recently developed methods allow selective signal loss recovery in these regions (5-9). The importance of these positive contrast techniques is their potential for improving iron detection sensitivity compared to standard T_2^* methods.

The "white marker" technique exploits the ability to compensate local field inhomogeneities, using a rephasing slice gradient to obtain a bright signal in regions of SPIO accumulation. The effect of this imaging gradient is to center the k-space on the echo produced by the spins under the influence of a local field inhomogeneity. This technique was originally employed by Seppenwoodle et al. (10) to achieve positive contrast from a paramagnetic material used in the passive tracking method of endovascular MRI. Furthermore, it was successfully applied at a field strength of 1.5 T both *in-vitro* and *in-vivo* in ferritin-containing blood-clot imaging. At 3 T, on the other hand, the authors concluded that the signal intensity obtainable with this method decreased as static magnetic field strength increased, as increased dephasing across the voxel was more difficult to compensate (8,11).

We hypothesized that, at an even higher field, on a small animal magnet equipped with stronger gradient coils, a significant positive signal could be obtained with the gradient compensation technique. Using a method similar to that of Mani et al. (8,11), we here report

in-vitro and *in-vivo* results at a 4.7 T magnetic field, with a novel superparamagnetic nanosystem designed for local radiation therapy.

MATERIALS AND METHODS

Contrast agent

The contrast agent used in the study was a polymer-based nanoparticulate system, produced by LAGEP Laboratory, France. It consisted of magnetite crystals, with a 12 nm size conferring superparamagnetic behavior, incorporated as a complex with oleic acid in a PLLA (poly L-lactic acid) polymer matrix containing non-radioactive [185-187]dirhenium decacarbonyl [$Re_2(CO)_{10}$]. The nanoparticles were prepared by emulsion evaporation so as to obtain biocompatible magnetic nanoparticles with sizes varying between 320 and 1500 nm. The relaxivity values, measured *in-vivo* on aqueous solutions at a 4.7 T magnetic field, were: *r1* = 1.7 ± 0.1 mM^{-1}s^{-1} and *r2* 228.3 ± 13.1 mM^{-1}s^{-1}. The entire preparation and characterization of the magnetic nanoparticulate system is described elsewhere (12).

Phantom preparation

The contrast agent suspension was mixed with liquid agarose to obtain a 1% w/w gel containing the nanoparticles in concentrations of 0.005, 0.05, 0.25, 0.5, 0.75 and 1 mmolFe/L. Phantoms were prepared in three plastic NMR tubes (3 cm in diameter) containing 2% agarose gel, by pouring the mixtures in two holes filled respectively with one low and one high concentration (cylindrical insertion of 1 mm diameter).

In-vivo study

Ten female OF1 mice obtained from Charles River, France, were used for the *in-vivo* study, which was carried out in accordance with current French guidelines for the care of laboratory animals and was approved by the animal ethics committee of Lyon1 University. After anesthesia by intra-peritoneal injection of 100 mg/kg Ketamine and 5 mg/kg Xylazine, all animals underwent a high pressure (400 bar) injection of contrast agent suspension at a concentration of 0.25 mmolFe/L in the left calf muscle, using the Targeted Multi Therapy (TMT) apparatus described elsewhere (2). For the MRI study, the animals were anaesthetized with 1.5 − 2% isoflurane gas under free breathing. At end of MRI follow-up, they were sacrificed by intraperitoneal pentobarbital injection and each calf muscle was removed for iron assay (ICP-AES after tissue digestion in HNO_3-HCl).

MRI protocol

Imaging was performed on a 4.7 T Bruker magnet (Bruker BioSpin GmbH, Germany; maximum gradient amplitude, 270 mT/m) with a Bruker transmission and receiver volume coil. The animal's legs were positioned along the longitudinal axis of the magnetic field. The same positioning was applied for the agarose phantoms.

The *in-vitro* study included a T2*-weighted gradient echo sequence with the following parameters: TE/TR, 10/300 ms; flip angle, 25°; number of averages, 4; matrix, 256 x 256; 2 non-contiguous 1.11 mm slices; spatial resolution, 156x156 µm. For positive contrast imaging, the rephasing gradient was varied between -100% and 0%. The standard value ($G_{standard}$) for negative contrast imaging was kept at -50%, to avoid increased noise.

In-vivo images were acquired in coronal sections with a T2*-weighted gradient echo sequence: TE/TR, 10/300 ms; flip angle, 25°; matrix, 256 x 256; slice thickness, 1.11 mm; spatial resolution, 234×234 µm; number of averages, 1. The MRI protocol was performed immediately after the injection and repeated 24 and 72 hours after the procedure.

Image analysis

Image analysis was performed using the ImageJ software (NIH). Regions of interest (ROI) were defined around the bright signal areas on the positive contrast images and around signal loss areas on the standard T2* images to measure the signal induced by particle accumulation ($S_{particles}$). The reference signals ($S_{reference}$) were taken in the no iron-containing agarose gel on the *in-vitro* images and in the calf muscle of the non-injected leg on the *in-vivo* images. The induced contrast enhancement (ENH%) was calculated as:

$$ENH\% = \left({S_{particles}} / {S_{reference}} - 1 \right) * 100,$$

Statistical analysis

Data are presented as mean ± standard deviations (SD). A one-way ANOVA was performed on the ENH% values obtained *in-vivo* from all follow-up time-points for each method. A $p<0.05$ was considered significant.

RESULTS

The pilot study performed on the range of concentrations indicated a -70% gradient value for the *in-vivo* studies (Figure 1). This decrease of 20% in rephasing gradient offered a good compromise for the iron dose-dependent signal intensity response, with a maximum

ENH% of 42.89±6.32% for the positive and a minimum of -70.03±7.1% for the negative contrast method, at highest concentration (1mmolFe/L).

One of the animals died after the first MRI, and for three others a full set of images was not available for all of the follow-up days. Thus the quantitative analysis was performed for a total of six animals; the number of analyzed slices was 12.
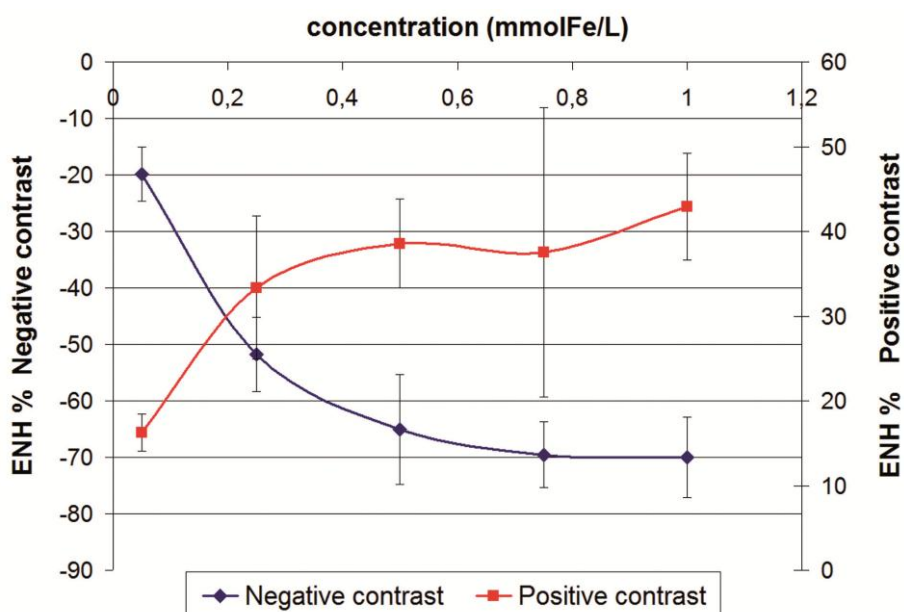

Figure 1. *Graph showing the in-vitro concentration effect on the ENH% for the positive and negative contrast imaging techniques. Data are represented with individual scales for each method.*

The *in-vivo* gradient-echo negative contrast images clearly showed signal loss at the injection site, thanks to the strong r2* relaxivity of the contrast agent (Figure 2). Also, they showed a perfect correlation between the bright regions obtained from gradient compensation and the injection site, as observed in the superposed images of Figure 2.

Iron assay in the calf muscle samples showed a mean concentration of 0.012±0.0017 mmolFe/L three days after local delivery of 0.25 mmolFe/L. The dose-related changes were more pronounced *in-vivo* than *in-vitro* for the gradient compensation technique, as opposed to standard negative contrast (data not shown).
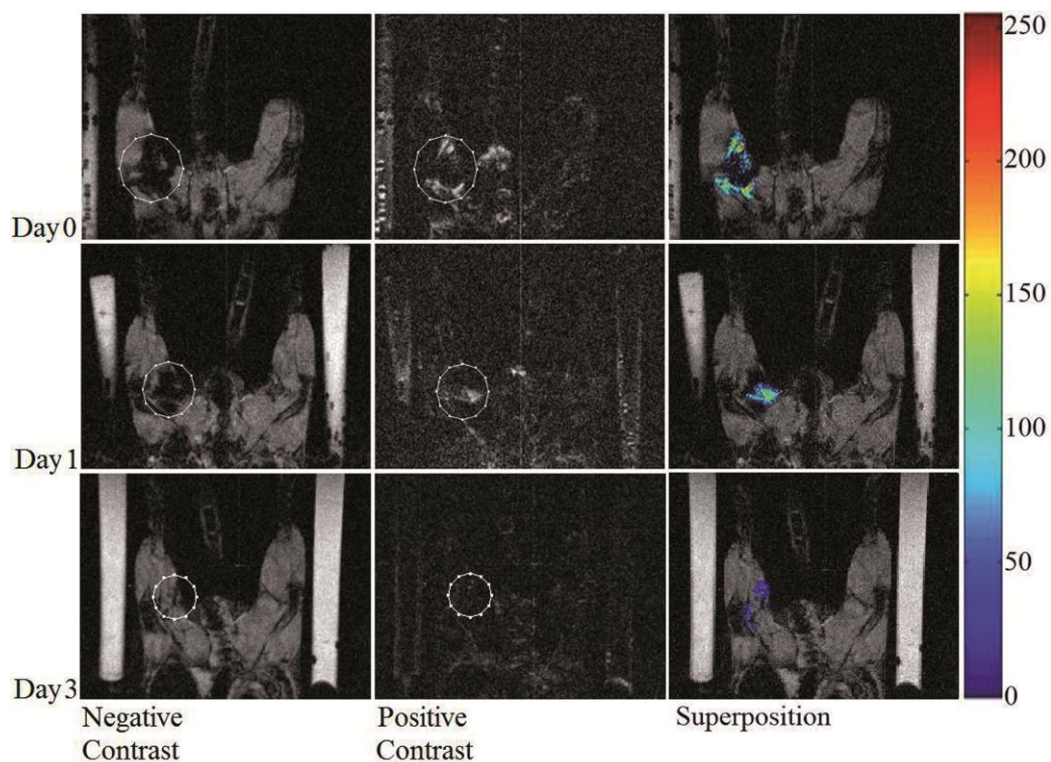
Figure 2. *T2*-weighted gradient echo images obtained from one animal during the longitudinal study, showing signal evolution over time, from immediately after nanoparticle administration (Day 0 to Day 3), respectively with the standard negative contrast (left column) and the positive contrast (middle column) of the same image slice. Gradient compensation leads to the appearance of bright spots at the injection site (circle). The images on the right show the superimposition of the injection site and the bright signal regions.*
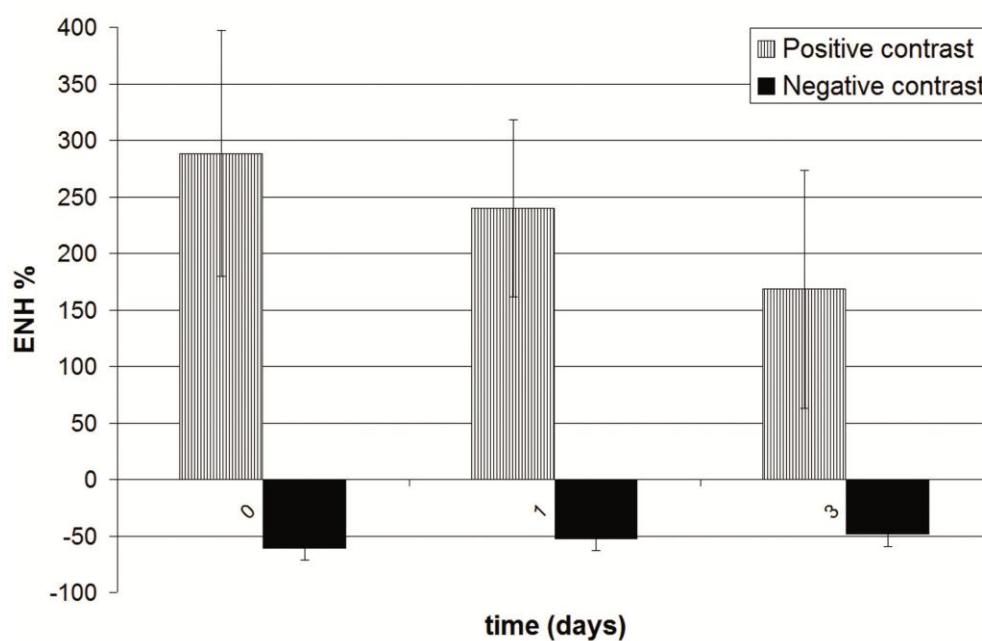

Figure 3. *Graph of ENH% values in both sets of images, showing significant decrease over time (p<0.05), which was more pronounced with positive contrast.*

DISCUSSION AND CONCLUSION

One of the most promising MRI techniques is image-guided drug delivery for clinical oncology (2). Using a novel SPIO with interesting properties for intra-tumoral radiotherapy, we have shown that the gradient compensation method can be effective at a relatively high field strength (8,11). Furthermore, it allowed a good characterization for SPIO location and *in-vivo* follow-up of contrast enhancement variation.

It is possible to achieve positive contrast with SPIO by employing T1 weighting. However, with the product tested in the present study, such a technique would be inefficient because of the high r2/r1 ratio (= 134.3), the large particle size (between 320 and 1500 nm, with a magnetite crystal size of around 12 nm), and relatively high concentration needed at the delivery site (2). Thus, positive contrast sequences based on susceptibility effects are appropriate techniques for the visualization of this kind of magnetic nanoparticulate system.

It was shown that, compared to other positive contrast techniques, the gradient compensation method is the most flexible and yields large bright regions with a very robust contrast *in-vivo* (13). For example, the IRON (inversion recovery on-resonance water suppression) method, which employs a spectrally selective RF pulse to presaturate on-resonance water, leaving the off-resonant protons in close vicinity to the SPIO nanoparticles unaffected, gives excellent results for phantom imaging, generating an extensive hyperintense area; but *in-vivo* the technique proved less sensitive than the gradient compensation method to low concentrations (14). It is also limited by severe artifacts due to the presence of lipids, although this can be corrected by using a fat-suppression pulse (14). Stuber et al. have successfully applied the IRON method *in-vitro* and *in-vivo* at two field strengths, 1.5 and 3T, and demonstrated direct proportionality between the number of labeled cells and the positive signal volume (15). It was also demonstrated that this positive technique can be applied to inflammation imaging with iron particles in an atherosclerotic animal model (16).

An alternative is a spin-echo type sequence, which exploits the frequency shifts induced by magnetic inhomogeneities, using two spectrally selective radio frequency (RF) pulses to excite and refocus a precise volume of spins off-resonance with the suppression of on-resonance signal (5). However, this technique is difficult to set up, as pulse modeling is necessary.

In the present study, contrast enhancement values plotted as a function of gradient amplitude showed a symmetrical distribution around the standard negative-contrast value (data not shown). This symmetry indicates that the two parts of the dipole field, the positive

polar and negative equatorial regions, were rephased separately, since the negative part of the dipolar field induced a negative local gradient superimposed on the static field. Such separate imaging of the two parts of the dipole field was also obtained by Cunningham et al. for the spectrally selective RF method (5).

A limitation of the present study is that only one value of the rephasing gradient was used for imaging, thus obtaining a bright region corresponding to half of the dipole field. This led to an underestimation of the real extent of the inhomogeneity region. However, in this study we only took into account the yielded signal intensities and not the spatial extent of susceptibility induced effects. Furthermore, it has recently been shown that the two images, obtained with $+$ and $-$ ΔGz, allow partial volume (PV) correction, by exploiting the asymmetry of the signal under dephasing conditions for magnetic susceptibility effects, whereas PV effects are found to be symmetric (17). For further studies, both symmetrically dephased images should be taken into consideration.

Given that the obtainable signal intensity is strongly dependent on diffusion, it can be hypothesized that the marked decrease in positive contrast (Figure 3) indicates a change in the physico-chemical state of the nanospheres; more specifically, permeability may be enhanced by microenvironmental change. This specificity compared to the standard technique should be studied in detail, as it could provide further insight into SPIO effects and transformation after accumulation in the tissue environment or inside labeled cells, which was not previously considered.

The technique does not provide anatomical information and thus should be used in complement to standard T2*-weighted imaging, in order to obtain a multicontrast type approach for *in-vivo* iron characterization.

In conclusion, we have shown that the gradient compensation technique can be effectively used at intermediate field strength at could provide better specificity for iron detection.

References

1. Wang YX, Hussain SM, Krestin GP. Superparamagnetic iron oxide contrast agents: physicochemical characteristics and applications in MR imaging. Eur Radiol 2001;11(11):2319-2331.

2. Hamoudeh M, Fessi H, Mehier H, Al Faraj A, Canet-Soulas E. Dirhenium decacarbonyl-loaded PLLA nanoparticles: Influence of neutron irradiation and preliminary in vivo administration by the TMT technique. Int J Pharm 2007.

3. Reichenbach JR, Venkatesan R, Yablonskiy DA, Thompson MR, Lai S, Haacke EM. Theory and application of static field inhomogeneity effects in gradient-echo imaging. J Magn Reson Imaging 1997;7(2):266-279.

4. Yang QX, Williams GD, Demeure RJ, Mosher TJ, Smith MB. Removal of local field gradient artifacts in T2*-weighted images at high fields by gradient-echo slice excitation profile imaging. Magn Reson Med 1998;39(3):402-409.

5. Cunningham CH, Arai T, Yang PC, McConnell MV, Pauly JM, Conolly SM. Positive contrast magnetic resonance imaging of cells labeled with magnetic nanoparticles. Magn Reson Med 2005;53(5):999-1005.

6. Dharmakumar R, Koktzoglou I, Li D. Generating positive contrast from off-resonant spins with steady-state free precession magnetic resonance imaging: theory and proof-of-principle experiments. Phys Med Biol 2006;51(17):4201-4215.

7. Faber C, Heil C, Zahneisen B, Balla DZ, Bowtell R. Sensitivity to local dipole fields in the CRAZED experiment: an approach to bright spot MRI. J Magn Reson 2006;182(2):315-324.

8. Mani V, Briley-Saebo KC, Hyafil F, Fayad ZA. Feasibility of in vivo identification of endogenous ferritin with positive contrast MRI in rabbit carotid crush injury using GRASP. Magn Reson Med 2006;56(5):1096-1106.

9. Zurkiya O, Hu X. Off-resonance saturation as a means of generating contrast with superparamagnetic nanoparticles. Magn Reson Med 2006;56(4):726-732.

10. Seppenwoolde JH, Viergever MA, Bakker CJ. Passive tracking exploiting local signal conservation: the white marker phenomenon. Magn Reson Med 2003;50(4):784-790.

11. Mani V, Briley-Saebo KC, Itskovich VV, Samber DD, Fayad ZA. Gradient echo acquisition for superparamagnetic particles with positive contrast (GRASP): sequence characterization in membrane and glass superparamagnetic iron oxide phantoms at 1.5T and 3T. Magn Reson Med 2006;55(1):126-135.

12. Hamoudeh M, Al Faraj A, Canet-Soulas E, Bessueille F, Leonard D, Fessi H. Elaboration of PLLA-based superparamagnetic nanoparticles: Characterization, magnetic behaviour study and in vitro relaxivity evaluation. Int J Pharm 2007;338(1-2):248-257.

13. Seppenwoolde JH, R. Oude Engberink, A. van der Toorn, E. L. Blezer, C.J. Bakker. Selective MRI of magnetically labeled cells – a comparative evaluation of positive contrast techniques. 2006.

14. Liu W, Dahnke H, Jordan EK, Schaeffter T, Frank JA. In vivo MRI using positive-contrast techniques in detection of cells labeled with superparamagnetic iron oxide nanoparticles. NMR Biomed 2007.

15. Stuber M, Gilson WD, Schar M, Kedziorek DA, Hofmann LV, Shah S, Vonken EJ, Bulte JW, Kraitchman DL. Positive contrast visualization of iron oxide-labeled stem cells using inversion-recovery with ON-resonant water suppression (IRON). Magn Reson Med 2007;58(5):1072-1077.

16. Korosoglou G, Weiss RG, Kedziorek DA, Walczak P, Gilson WD, Schar M, Sosnovik DE, Kraitchman DL, Boston RC, Bulte JW, Weissleder R, Stuber M. Noninvasive detection of macrophage-rich atherosclerotic plaque in hyperlipidemic rabbits using "positive contrast" magnetic resonance imaging. J Am Coll Cardiol 2008;52(6):483-491.

17. Seppenwoolde JH, Vincken KL, Bakker CJ. White-marker imaging--separating magnetic susceptibility effects from partial volume effects. Magn Reson Med 2007;58(3):605-609.

Chapter III

T2* mapping of a USPIO contrast agent by MRI at three different field strengths

T2* mapping of a USPIO contrast agent by MRI at three different field strengths

Monica Sigovan [1], Elena Kaye [2], Hisanori Kosuge[2], Florence Lagarde[3], Marcus Alley [2],

Kim Butts Pauly [2], Emmanuelle Canet-Soulas [1]

[1]. Lyon 1 University, CREATIS-LRMN Laboratory

[2]. Stanford University, Radiology Department

[3]. Lyon 1 University, Laboratoire de Sciences Analytiques

ABSTRACT

Objectives: We investigated the use of a very short TE gradient echo sequence for the T2* mapping of a wide range of free ultra-small superparamagnetic iron oxide (USPIO) concentrations and magnetically labeled cells at three magnetic fields in order to obtain calibration curves and determine the detection limit of the sequence.

Materials and Methods: MR imaging was performed on 1.5, 3 and 7 T General Electric scanners (GE Medical Systems, Milwaukee, WI) using 8-channel head coil. Investigations were performed on two phantoms, one containing increasing concentrations of free USPIO particles (P904, Guerbet, Paris, France) in agar (0.05 to 8.55 mM Fe); and the second containing suspensions of P904 labeled cells. A single-echo fast spoiled gradient echo (SPGR) sequence with fractional echo was used for relaxivity measurements. The minimum echo time (TE: 1004 μs at 1.5 T, 848 μs at 3T; and 972 μs at 7T) was stepped at increasing intervals to a final value of 50 ms. T2* maps were calculated by fitting mono-exponentially the signal decay with TE on a pixel by pixel basis. Iron concentrations of labeled cells were measured by inductively coupled plasma atomic emission spectrometry (ICP-AES).

Results: A linear relationship between R2* and concentration ($R^2 > 0.95$) was obtained for every measurement performed on free particles containing tubes at the investigated fields. The slope of the linear regression (r2*) did not show a field dependence. For similar iron concentration intervals, T2* values were several times shorter for magnetically labeled cells compared to free particles.

Conclusion: The fractional echo sequence is adapted for the detection of high iron concentrations. The curves of T2* variation with iron concentration should prove helpful in optimizing sequence parameters for *in vivo* applications.

Key words: USPIO, T2* mapping, fractional echo

INTRODUCTION

Superparamagnetic iron oxide ((U)SPIO) nanoparticles are an important class of MR contrast agents that originally were used for liver examinations (1, 2), but quickly proved efficient in other applications. One of the applications that greatly benefited from the development of this class of contrast agents is cellular imaging, which relies on non-invasive tracking of magnetically labeled cells with MRI. Labeling can be done either directly, *in vitro* on cell cultures (3) or indirectly by injecting free SPIO particles in the blood stream where they are taken up by immune cells. SPIO are the preferred labeling agent because they provide a high contrast change, in particular on T2* weighted images (4-7).

One of the most sought-after goals in nowadays research is improving (U)SPIO diagnosis value by applying adapted quantification methods. Intensive research in the field of iron overload pathologies lead to good quantitative MR techniques that have been successfully applied for nearly 20 years in iron estimation in the liver and more recently the heart (8-12).

(U)SPIO are known to have stronger MR relaxation properties compared to the endogenous iron, thus shorter echo times are needed for a reliable detection of high concentrations. In this work we investigated the use of a rapid, very short TE, gradient echo sequence for the T2* mapping of a wide range of free USPIO concentrations and magnetically labeled cells at three magnetic fields. The goal was to obtain calibration curves for the chosen USPIO and to determine the detection limit of the investigated sequence.

MATERIALS AND METHODS

Contrast agent

An ultra-small superparamagnetic iron oxide (USPIO) contrast agent, the P904, recently approved for clinical research (Guerbet Laboratories, Paris, France), was used in the study.

The P904 nanoparticles are composed of a maghemite crystalline core, coated with a low molecular weight amino-alcohol derivative of glucose with an average hydrated particle diameter of 21 nm. The longitudinal (r1) and transverse (r2) relaxivities measured at three magnetic fields are gathered in Table 1.

Table 1*. Longitudinal (r1) and transverse (r2) relaxivities measured at three magnetic fields (unpublished Guerbet data)*

Magnetic field strength	r1 ($s^{-1}\cdot mM^{-1}$)	r2 ($s^{-1}\cdot mM^{-1}$)
1.5 T	14±1	90±5
3 T	7±1	90±5
7 T	1.6±0.2	94±5

Cell labeling

Cell labeling was performed in RAW cells (mouse macrophages cell lines). Briefly, RAW cells suspensions were cultured in Dulbecco's Modified Eagle Medium (DMEM) supplemented with 10% fetal calf serum (FCS) and incubated in a humidified atmosphere containing 5% $CO2$ at 37°C for one week. Magnetic labeling of the cells was performed by adding a sterilized suspension of P904 in DMEM 10% FCS to adherent cells. Macrophages were incubated at 37°C overnight with three iron concentrations: 50, 75 and 100 µg Fe/ml, they were then rinsed (3 times) and resuspended in phosphate buffer saline (PBS), counted and placed in plastic tubes.

MRI protocol

Two phantoms were used for the study. One phantom was made up of 9 plastic tubes, containing homogeneous suspensions of free USPIO in 3% agar gel with increasing concentrations of iron from 0.05 to 8.55 mM Fe. The second phantom was made up of three tubes containing suspensions of labeled cells in PBS. MR imaging was performed on 1.5, 3 and 7 T General Electric scanners (GE Medical Systems, Milwaukee, WI) using 8-channel head coil. A single-echo fast spoiled gradient echo (SPGR) sequence using a minimum phase, 600 ms long RF pulse with fractional echo was used for relaxivity measurements. The minimum echo time (TE) used was: 1004 µs at 1.5 T, 848 µs at 3T; and 972 µs at 7T and it was stepped at increasing intervals to a final value of 50 ms. For every field intensity the other acquisition parameters were as follows: TR = 65 ms, band width (BW) = 976.5 kHz, matrix = 256×256, pixel size 0.86×0.86 mm, slice thickness = 2 mm. For labeled cells experiments a higher spatial resolution was used (pixel size = 0.6×0.6 mm) thus the first available echo time was longer, as follows: 1.2 ms at 1.5T and 1.3 ms at 3T and 7T.

For free particles, at each field strength the profiles of the investigated volume were obtained by measuring the mean signal intensity in a circular ROI (10 pixels in diameter) placed in the centre of each tube on images obtained with the shortest echo time. The border pixels (N=2) were excluded from the measurement to avoid susceptibility effects from the tube gel interface. Only the 2 adjacent slices with the highest signal intensities over the 10 slices acquired were used for relaxation measurements. T2* maps were calculated on the two adjacent slices by fitting mono-exponentially the signal decay with TE on a pixel by pixel basis using the 'fminsearch' function of Matlab (The MathWorks Inc, Natick, MA, USA). The function assumed to describe de decay was: $S = S_0 \cdot \exp(-TE/T2^*) + C$; where S0 is the signal intensity at TE = 0 and C is a constant that compensates for the presence of noise. The goodness of the fit was also calculated and the pixels that gave a regression r < 0.8 were removed. Mean T2* values were measured for each concentration in the same manner as the intensity profiles for free particles and in a square ROI (5 pixels in length) for labeled cells.

Iron quantification by ICP-AES

Iron concentration in each tube containing labeled cells was measured by inductively coupled plasma atomic emission spectrometry (ICP-AES), using an axial Jobin-Yvon 138 Ultrace prototype spectrometer operating at 1,075 W and equipped with a Meinhard-type nebulizer and Scott spray chamber. The samples were digested in a closed Ethos Touch Control microwave device from Milestone. Before use, the vessel was cleaned by addition of 5 mL 65% HNO3 (Fluka) and 3 mL ultrapure water and heated to 180°C for 15 min. Each sample was placed in a 50-mL Teflon digester. Then 5 mL 65% HNO3, 2 mL 30% H2O2 (Trace Select, from Fluka) and 1 mL ultrapure water were added. The digester was closed, progressively heated to 180°C in the microwave (15 min) and then maintained at 180°C for 30 min. Blanks were performed to check the absence of reagent pollution. After cooling, mineralized samples were diluted to 18 ml. Flow rates were plasma gas=12 l·min^{-1}, nebulizer gas= 0.7 l·min^{-1} and auxiliary gas=0.15 l·min^{-1}. Integration time was set at 2 s and wavelength at 238.2 nm.

Statistical analysis

Statistical analysis was performed for free particles. Reproducibility was assed by repeating three times the imaging sessions. Slice to slice variability was examined in two

adjacent slices. Linear regression analyses was performed to characterize the relation between 1/T2* (R2* relaxation rate) and concentration.

RESULTS

In all experiments, stronger signal loss in tubes with higher iron concentration of free particles was clearly visible on the magnitude MR images. The obtained T2* maps are presented in figure 1. Note the decrease of T2* values with increasing external field.
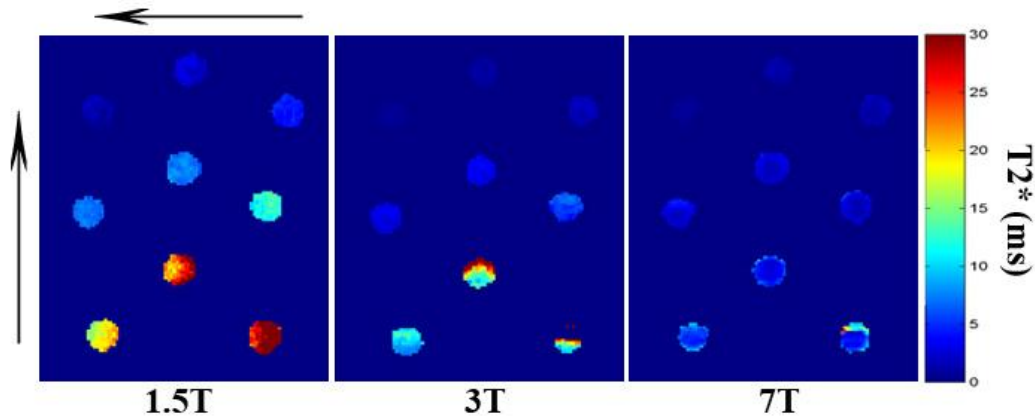

Figure 1. T2* maps calculated from 12 echo images acquired at 1.5T, 3T and 7T. Arrows point the increasing concentrations. Note the decrease in relaxation times (T2*) as external field strength increases. Colorbar represents the T2* values in ms.

T2* measurements varied between imaging slices (mean coefficient of variation (CV) for 1.5T was 0.06 and 0.2 for 3T and 7T) and between imaging sessions (mean CV of 0.5 for 1.5T, 0.1 for 3T and 0.3 for 7T). The mean T2* values over all measurements for the highest (8.55 mM Fe) and the lowest concentration (0.05 mM Fe) are gathered in Table 1. T2* variation as a function of concentration is presented in Figure 2A.

Table 1. *Mean T2* values over 6 measurements for the highest and the lowest concentrations of free particles*

Field Strength	Highest Concentration (mM Fe)	T2* (ms)	Lowest Concentration (mM Fe)	T2* (ms)
1.5 T		0.8±0.4		18.2±3
3 T	8.55	0.57±0.03	0.05	14.6±7
7 T		0.6±0.03		5.5±3

Concerning the magnetic labeling, an average number of 6.3 million cells were obtained per tube; they were suspended in PBS and allowed to sediment. The volume occupied by the cells was estimated from the MR images at around 30 mm^3. T2* values measured in each tube are presented as a function of the iron concentration obtained by ICP-AES (Figure 2B). Note that T2* values are several times shorter (~ 4) for similar intervals of iron concentration, for magnetically labeled cells compared to free particles.
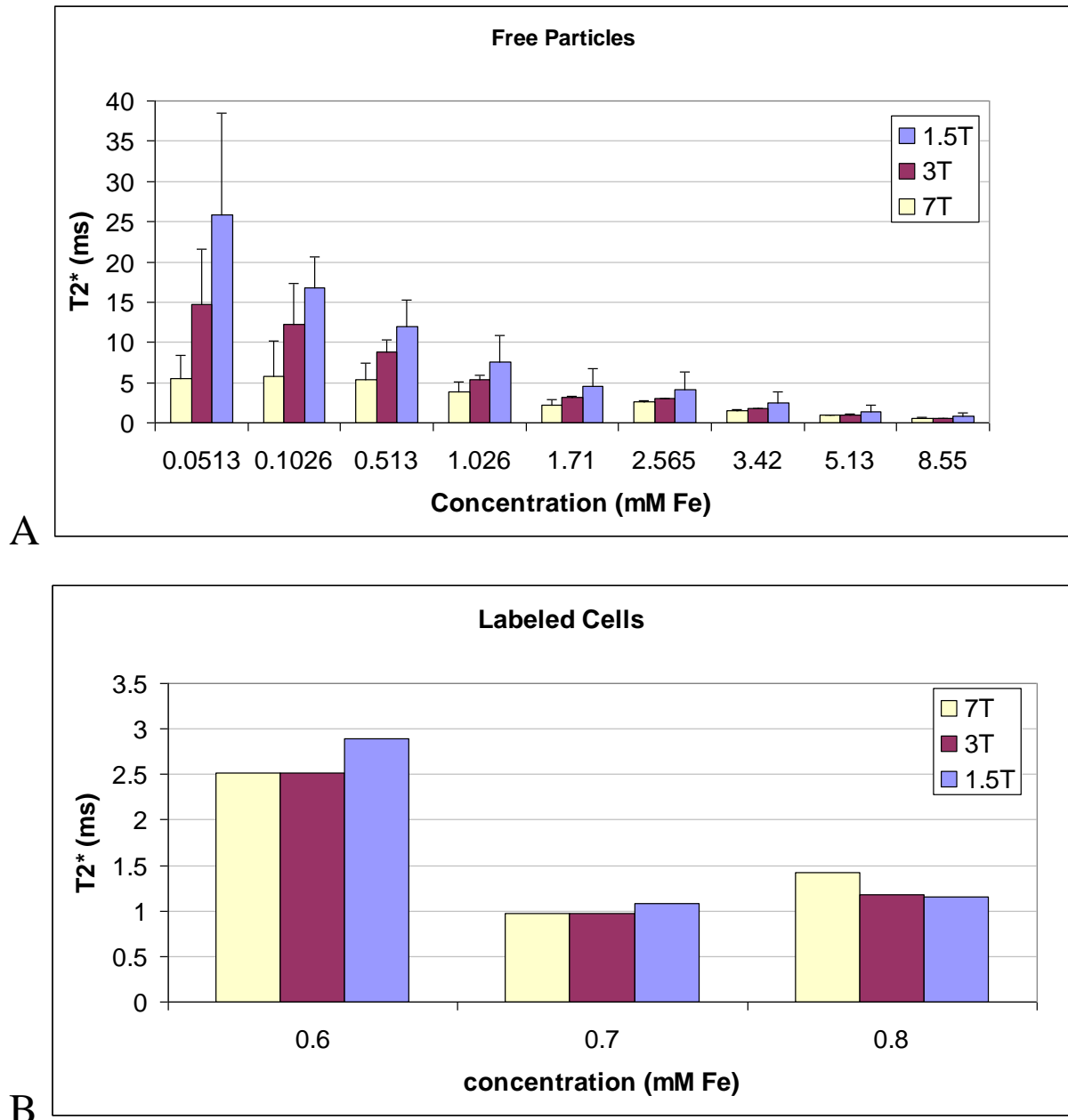

A

B

Figure 2. Mean T2* values represented as a function of iron concentration calculated at 1.5, 3 and 7T for free particles (A) and labeled cells (B).

A linear relationship between R2* and concentration ($R^2 > 0.95$) was obtained for every measurement performed on free particles containing tubes at the investigated fields (Figure 3). The slope of the linear regression (r2*) did not show a field dependence. No significant difference was found between r2* values obtained at 1.5T, 3T and 7T.
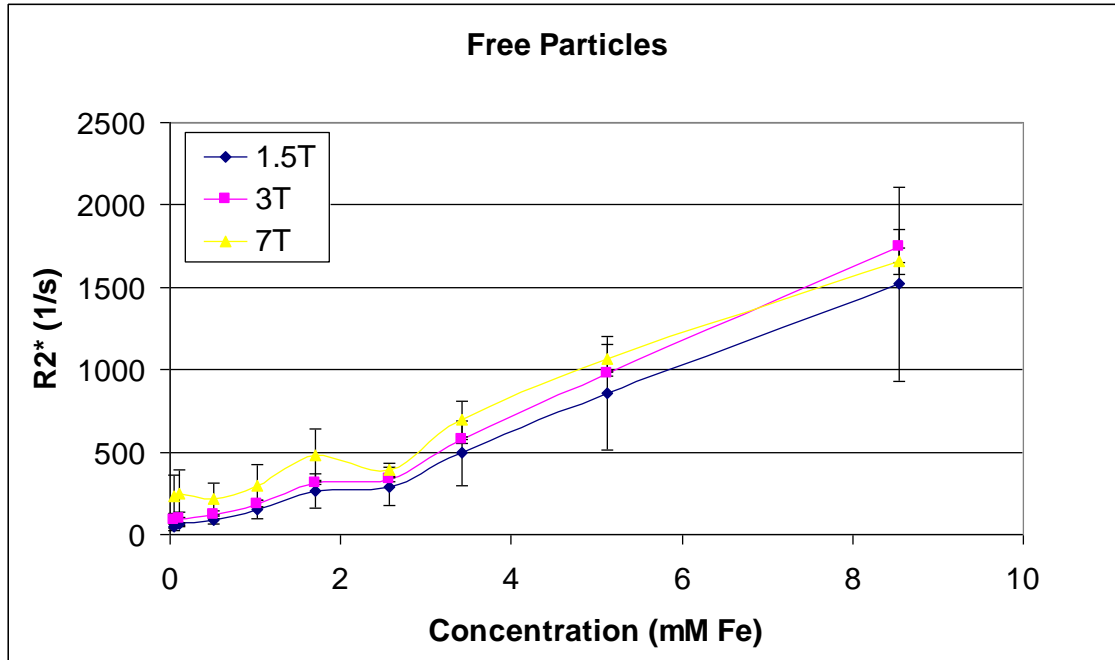

Figure 3. *Graphical representation of the R2* dependency on the USPIO concentration calculated at 1.5T, 3T and 7T for free particles. The slope of R2* increase with concentration is field independent. Data are presented as means ± SD.*

DISCUSSION

Intensive research in the field of iron overload pathologies lead to good quantitative MR techniques that have been successfully applied for nearly 20 years in iron estimation in the liver and more recently the heart (8, 9, 11, 13). The important number of studies has produced calibration curves for iron concentrations that are currently used for the clinical diagnosis of these pathologies. Obtaining calibration curves for (U)SPIO agents is highly desirable in order to improve their diagnosis value.

In the present study we performed T2* measurements on a wide range of USPIO concentrations that can be expected for *in-vivo* applications. Several problems can be identified with T2 and T2* mapping techniques like the need for a test that can asses a full range of iron concentrations with one set of parameters. The factors limiting the accuracy of these measurements are related to the number of echoes and the minimum echo spacing that can be used. The present study addressed these problems.

The 3D fractional echo gradient echo sequence tested in this study allowed the use of echo times of less than one millisecond. The choice of using increasing ΔTEs between acquisitions is justified by the need of adapting the sampling of signal decrease to the relaxation rate that is related to it. Small intervals are needed for a correct sampling of high relaxation rates expected for high iron concentrations. We performed investigations on concentrations up to ten times higher than those previously reported and found that iron quantity is directly proportional to the inverse of the relaxation T2* in agreement with literature data (14, 15).

The effect of the external magnetic field was also investigated. Shorter T2* values obtained with increasing field are a direct consequence of the fact that the local dipolar field induced by the particles is directly proportional with the external magnetic field as described by Cunningham et al. (16). The apparent transverse relaxation (1/T2*) increases with the increase of the external field, however, the relaxivity (r_2^*) given by the slope of R2* variation with concentration is not field dependant. Concerning the highest investigated concentration (8.55 mMFe) of free particles, we found that the mean T2* value increased at 7T. This was also observed for the highest concentration of magnetically labeled cells. It can thus be assumed that the high relaxation rate was underestimated by the calculations. We can conclude that the limit of detection for free particles is around 5mM Fe and for magnetically labeled cells around 0.7 mM Fe with the set of parameters proposed here.

The difficulties of applying this quantification MRI to *in vivo* USPIO evaluation arise on one hand from the bio-distribution of the particles that leads to having two states free particles and aggregated inside cells. This limitation could potentially be overcome with the use of bi-exponential calculation methods. This could prove effective, once a sufficient quantity of information is gathered for the different states. Another difficulty arises from acquisition duration constraints that will limit the attainable spatial resolution.

In conclusion, we showed that the fractional echo sequence is adapted for the detection of high iron concentrations. The goal of this quantification essay was to offer an optimized set of parameters that enable quantification of a large interval of USPIO concentrations. The curves showing T2* variation with iron concentration should prove helpful in optimizing sequence parameters for *in vivo* applications.

References

1.   Ferrucci JT, Stark DD. Iron oxide-enhanced MR imaging of the liver and spleen: review of the first 5 years. AJR Am J Roentgenol 1990; 155:943-950.

2.   Bellin MF, Zaim S, Auberton E, et al. Liver metastases: safety and efficacy of detection with superparamagnetic iron oxide in MR imaging. Radiology 1994; 193:657-663.

3.   Daldrup-Link HE, Rudelius M, Piontek G, et al. Migration of iron oxide-labeled human hematopoietic progenitor cells in a mouse model: in vivo monitoring with 1.5-T MR imaging equipment. Radiology 2005; 234:197-205.

4.   Weissleder R, Cheng HC, Bogdanova A, et al. Magnetically labeled cells can be detected by MR imaging. J Magn Reson Imaging 1997; 7:258-263.

5.   Bulte JW, Zhang SC, van Gelderen P, et al. Magnetically labeled glial cells as cellular MR contrast agents. Acad Radiol 2002; 9 Suppl 1:S148-150.

6.   Bos C, Delmas Y, Desmouliere A, et al. In vivo MR imaging of intravascularly injected magnetically labeled mesenchymal stem cells in rat kidney and liver. Radiology 2004; 233:781-789.

7.   Bulte JW, Kraitchman DL. Monitoring cell therapy using iron oxide MR contrast agents. Curr Pharm Biotechnol 2004; 5:567-584.

8.   Clark PR, St Pierre TG. Quantitative mapping of transverse relaxivity (1/T(2)) in hepatic iron overload: a single spin-echo imaging methodology. Magn Reson Imaging 2000; 18:431-438.

9.   Clark PR, Chua-Anusorn W, St Pierre TG. Proton transverse relaxation rate (R2) images of liver tissue; mapping local tissue iron concentrations with MRI [corrected]. Magn Reson Med 2003; 49:572-575.

10.   Wood JC, Enriquez C, Ghugre N, et al. MRI R2 and R2* mapping accurately estimates hepatic iron concentration in transfusion-dependent thalassemia and sickle cell disease patients. Blood 2005; 106:1460-1465.

11.   Positano V, Pepe A, Santarelli MF, et al. Standardized T2* map of normal human heart in vivo to correct T2* segmental artefacts. NMR Biomed 2007; 20:578-590.

12.   Ramazzotti A, Pepe A, Positano V, et al. Multicenter validation of the magnetic resonance T2* technique for segmental and global quantification of myocardial iron. J Magn Reson Imaging 2009; 30:62-68.

13. St Pierre TG, Clark PR, Chua-Anusorn W. Measurement and mapping of liver iron concentrations using magnetic resonance imaging. Ann N Y Acad Sci 2005; 1054:379-385.

14. Kuhlpeter R, Dahnke H, Matuszewski L, et al. R2 and R2* mapping for sensing cell-bound superparamagnetic nanoparticles: in vitro and murine in vivo testing. Radiology 2007; 245:449-457.

15. Brisset JC, Desestret V, Marcellino S, et al. Quantitative effects of cell internalization of two types of ultrasmall superparamagnetic iron oxide nanoparticles at 4.7 T and 7 T. Eur Radiol 2009.

16. Cunningham CH, Arai T, Yang PC, et al. Positive contrast magnetic resonance imaging of cells labeled with magnetic nanoparticles. Magn Reson Med 2005; 53:999-1005.

Chapter IV

Rapid-Clearance Iron Nanoparticles for Inflammation Imaging in Atherosclerotic Plaque: Initial Experience in Animal Model

Rapid-Clearance Iron Nanoparticles for Inflammation Imaging in Atherosclerotic Plaque: Initial Experience in Animal Model

Monica Sigovan[1] MS, Loic Boussel[1] MD, PhD, Abdulrazzaq Sulaiman[1] MD, Dominique Sappey-Marinier[1,2] PhD, Hasan Alsaid[1] PhD, Catherine Desbleds-Mansard[1], Danielle Ibarrola[2] PhD, Delphine Gamondes[1] MD, Claire Corot[3] PhD, Eric Lancelot[3] PhD, Jean-Sebastian Raynaud[3] PhD, Veronique Vives[3] MS, Christine Laclédère[3] MS, Xavier Violas3 MS, Philippe Douek[1] MD, PhD and Emmanuelle Canet-Soulas[1] DVM, PhD

1. Université Lyon 1, CREATIS-LRMN, UMR CNRS 5220, U630 INSERM, Lyon, France.
2. CERMEP, Lyon, France.
3. GUERBET Group, Aulnay-sous-Bois, France.

Advance(s) in Knowledge:

- P904's fast blood clearance allows detection of aortic wall inflammation at 24 to 48 hours after administration of a dose of 1000 µmolFe/kg in a rabbit model of induced atherosclerotic plaques.

- A long exposure time is not the predominant factor for high up-take in atherosclerotic plaque. In addition, size and coating properties of iron oxide-based nanoparticles are both important factors.

Implication(s) for Patient Care:

- The proposed protocol can potentially be adapted to human studies of the carotid arteries, allowing early post-contrast imaging.

ABSTRACT

Purpose: To evaluate the use of new fast-clearance ultrasmall superparamagnetic particles of iron oxide (USPIO) for detection of vascular inflammation in atherosclerotic plaque.

Materials and Methods: The protocol was approved by the animal experimentation ethics committee of our institution. P904 (Guerbet Laboratories, France) and a reference USPIO (Ferumoxtran-10) were tested in a rabbit model of induced aortic inflammation (hyperlipidemic New Zealand white rabbits, N=26). *In vivo* MR angiography and T2*-weighted plaque imaging were performed at baseline and after administration of a total dose of 1000 µmolFe/kg. Vessel wall area variation over time was evaluated using a nonparametric test. *Ex vivo* MRI was compared to iron content by linear regression.

Results: With *in vivo* MRI, plaque analysis was possible as early as 24 hours after P904 injection in rabbits. A 27.75% increase in vessel wall area due to susceptibility artifacts was obtained with P904 at day 2 (p=0.04) and a 38.81% increase at day 3 (p=0.04), compared to +44.5% at day 7 (p=0.04) and +34.8% at day 10 (p=0.22) with Ferumoxtran-10. These susceptibility artifacts were correlated with intraplaque iron uptake in corresponding histological slices. The number of pixels with signal loss on *ex-vivo* MR images was linearly correlated to the logarithm of the iron concentration (p=0.0001; R-squared=0.93).

Conclusions: Plaque inflammation can be detected in rabbits using P904 earlier than with Ferumoxtran-10, thanks to a faster blood pharmacokinetics and an early uptake in the reticulo-endothelial system.

Key Words: atherosclerosis; USPIO; rapid pharmacokinetics; animal model.

INTRODUCTION

Previous pre-clinical and clinical studies have demonstrated the ability of iron oxide particles to characterize inflammation in atherosclerotic plaques both in animal models and in patients (1-5). A potential clinical application of USPIO is to better differentiate *in vivo* between low- and high-risk plaques as USPIOs accumulate predominantly in ruptured and rupture-prone lesions for risk stratification (3). Pre-clinical studies of atherosclerosis imaging using USPIO were originally based on 3D angiography (MRA) techniques, where the blood T1 effect of a low dose shows a bright signal in the lumen and the T2* effect of intraplaque accumulated iron oxide particles results in a signal void at the lumen boundaries (2, 6, 7). Compared to gadolinium based agents for MR angiography, using first-pass imaging sequences, the longer circulation time of USPIO's allows a wider imaging window enabling the use of high spatial resolution sequences (8). Schmitz et al. focused, in a rabbit model for evaluating the thoracic aorta, on the vessel wall rather than the lumen signal using a high resolution T2*-weighted gradient echo (GE) sequence. Focal signal loss within the wall was correlated with the histological pattern of iron accumulation (9). Among the limitations entailed by presently available iron oxide particles, the long delay between USPIO injection and the imaging window is an important drawback for widespread clinical application. Indeed, the presently recommended interval before atherosclerotic plaque imaging in animal models (iron doses for rabbits are between 250 and 1,000 µmol Fe/kg) is 5 to 7 days after USPIO injection (1, 2, 6, 7, 10-12). Moreover, the diagnostic efficacy for the detection of plaque inflammation may be quite different from one iron oxide particle to another, both in animal models of atherosclerosis (6, 11) and in symptomatic patients scheduled for carotid endarterectomy (13). The type of coating and the size of the particles are actually very critical for optimal targeting of plaque macrophages.

The aim of our study was to evaluate the use of a new USPIO (P904, Guerbet Laboratories, Paris, France) for MRI detection of vascular inflammation in atherosclerotic plaque. A high spatial resolution MRI protocol was adapted to delineate iron uptake in a rabbit model of atherosclerotic plaques. A dose range study was also performed to establish the lowest detectable dose in atherosclerotic lesions.

MATERIALS AND METHODS

The work presented here is a research project that was partially financed by a grant from Guerbet, which also provided the already-patented contrast agent, P904.

Animal model

The protocol was approved by the animal experimentation ethics committee of our institution. A total number of 26 New Zealand white rabbits (mean weight, 3.7 kg, age 16 weeks, Harlan, France) were used in the study. Animals were included on the basis of a minimum weight of 3 kg. An exclusion criterion was overall bad health due to the high fat diet, but no animal had to be excluded for this reason. The induced focal aortic inflammation model has been chosen as it is well described in literature and commonly used for USPIO studies (2, 11). Briefly, a group of N = 24, after 15 days on a high-cholesterol diet (0.3% cholesterol) underwent two vascular interventions: a de-endothelialization of the infrarenal aorta followed by an angioplasty at a fifteen-day interval (2). From a histological view point, the aortic lesions are reproducible from one animal to another. Half of these animals (N = 12) were subject to *in vivo* MRI and the other half were used for the dose range study. The two remaining animals (of the total of 26 animals) that did not undergo vascular interventions were used as the control group for the *in vivo* MRI study to validate specific uptake in inflammatory lesions.

In vivo MRI was performed after a total of 75 days on the diet. Twelve atherosclerotic animals were randomly divided in two groups, one subgroup received P904 and the second subgroup received Ferumoxtran-10 as reference standard, with a total dose of 1000 µmolFe/kg for each product. The same dose of the new USPIO was administered to the healthy group. One rabbit from the subgroup that received Ferumoxtran-10 at the high dose did not recover from anesthesia after the first MRI. Animals were anesthetized by intramuscular injection of a Ketamine/Xylazine mixture (50 mg/kg and 5 mg/kg, respectively) for MRI and were then sacrificed by exsanguination.

The other half of the atherosclerotic rabbits were divided in three groups (N = 4 each), receiving three different P904 doses: 150, 350 and 1000 µmolFe/kg. All animals were sacrificed 24 hours post-injection and *ex-vivo* imaging was performed for the semi-quantitative analysis of iron accumulation into aortic samples.

Contrast agents

The P904 USPIO (Guerbet Laboratories, Paris, France) and a reference product, currently being evaluated for approval by the regulatory authorities, the Ferumoxtran-10 (AMI227, Sinerem[R], Guerbet Laboratories, Paris, France; Combidex[R], Advanced Magnetics, Cambridge, Massachusetts, USA), were used in this study. They are made of a maghemite core coated with a low molecular weight amino-alcohol derivative of glucose and a dextran polymer, respectively. For P904, this type of coating represents approximately 2000 hydroxyl groups per nanoparticle. Its plasma half-life in hyperlipidemic rabbits is 3.5 hours for a dose of 1000 µmolFe/kg (Supplemental Data), compared to several days for the corresponding dose of Ferumoxtran-10.

The relaxivities measured in water at 1.42 T and 37°C were $r_1 = 9.9$ mM^{-1}s^{-1} and $r_2 = 65$ mM^{-1}s^{-1} for Ferumoxtran-10, with an average hydrated particle diameter of 35 nm, and $r_1 = 14$ mM^{-1}s^{-1} and $r_2 = 87$ mM^{-1}s^{-1} for P904, with a particle diameter of 21 nm.

The administration technique was the same for both contrast agents, as follows: a bolus injection through a catheter placed in the ear vein, was performed only for the angiographic dose (50 µmolFe/kg); the high dose was administered by a slow injection with a rate of approximately 1 ml/minute.

Efficacy of plaque imaging

In vivo MRI protocol

Imaging was performed on a clinical 1.5 T system (Sonata, Siemens, Erlangen, Germany) using two carotid surface coils (Magnex Scientific, UK). Coils were positioned on the back of the animal in decubitus position. External fiducial landmarks (sternum, ribs) were used to center the examination on the origin of the left renal artery. Two reference tubes doped with Gadolinium DOTA (DOTAREM®, Guerbet 0.3µmol/ml) were positioned on the animal's side for signal intensity calibration.

The imaging protocol (sequence parameters in Table 1), was performed at baseline, i.e., six weeks after the vascular intervention, and repeated on days 1, 2 and 3 after P904 injection and on days 7 and 10 after Ferumoxtran-10 injection (1, 2, 6, 12). In short, three axial slices were acquired using 2 gradient-echo (GE) sequences for two different T2* weightings. Positioning of the slices was as follows: two in a surgically prepared aortic area (1 and 2 cm above the left renal artery origin) and one slice in a "healthy" aortic area (between the two renal arteries). A 3D T1-weighted GE was performed before and after the

injection of an angiographic dose of the contrast agents. The total duration of imaging and positioning for each animal was one hour.

Contrast agents were administered at baseline as follows: a low dose of 50 µmolFe/kg for MR angiography (MRA) and a re-injection at the end of the MR examination, for a total dose of 1,000 µmol Fe/kg (representing 2.54 ml/kg for the P904 group and 2.8 ml/kg for the Ferumoxtran-10 group). At follow-up, an additional dose (50 µmolFe/kg) was injected when the blood T1 effect was not sufficient to ensure high quality MRA.

Table 1. *In vivo MR imaging protocol*

Sequence Type	Sequence Parameters	Acquisition Time
Proton Density localizer	TR/TE = 1540/20 ms, FOV = 60 mm, FA = 150°, BW = 85 Hz/pixel, NA= 5, turbo factor = 11, voxel size = 0.2/0.2/3.0 mm, 6 axial slices	4 min 56 sec
High Resolution Long TE	TR/TE = 800/20 ms, FOV = 60 mm, FA = 25°, BW =127 Hz/pixel, NA = 8, voxel = 0.2/0.2/3.0 mm	4 min 17 sec
High Resolution Short TE	TR/TE = 500/3.65 ms, FOV = 80 mm, NA = 2, FA = 30°, BW = 300 Hz/pixel, voxel = 0.3/0.3/3.0 mm	3 min 14 sec
MRA	TR/TE = 8.62/2.97 ms, FOV = 100 mm, NA = 4, FA = 30°, BW = 130 Hz/pixel, voxel = 0.4/0.3/0.3 mm	6 min 46 sec

Abbreviations*: TR – repetition time, TE – echo time, FOV – field of view, FA – flip angle, BW – bandwidth, NA – number of accumulations.*

Image analysis

Image analysis was performed using a dedicated software (Creatools) (14)

The blood T1 effect was assessed on 3D MRA images reconstructed in the transverse plane. A circular region of interest (ROI) was positioned in the lumen center of the abdominal aorta and the mean signal intensity, normalized to the signal of the reference tube, was recorded at baseline and for each follow-up day (MS, 3 years experience).

A quantitative analysis of the area of signal loss in the vessel wall was performed on the *in vivo* GE images. On each slice, inner and outer contours of the aortic wall were delineated manually and separately by two observers (E.C. 10 years experience, L.B. 8 years). Vessel

wall area was determined by subtracting the inner from the outer area measurement. The variation in area between pre-contrast and post-contrast images was evaluated using the following expression (1) :

$$\delta A = \left(\frac{A_{post} - A_{pre}}{A_{pre}} \right) \cdot 100 \qquad (1)$$

where A_{pre} and A_{post} define the areas measured at baseline and after USPIO injection. Signal to noise ratio (SNR) variations were calculated similarly.

Histology

After sacrifice of the animals, aortic specimens were fixed in formalin and embedded in paraffin for histology with hematoxilin-eosin stain (HES); Perl's staining was used to determine the presence of iron particles, and RAM-11 monoclonal antibody (Dako, France) was used to label the macrophages. Two slices per animal were analyzed for the control rabbits.

Dose range study

After sacrifice of the 12 atherosclerotic animals, 24 hours post contrast administration of the three different doses, the infrarenal aorta was cut into 24 three-millimeter thick slices. After weighing, each slice was placed in an agar gel well and *ex vivo* MRI was performed at 2.35 T (Bruker, Germany) with a 3D GE sequence (TR/TE = 15/4.2 msec, flip angle = 75°, FOV = 80x60x17 mm, number of accumulations = 32, band width = 217 Hz/pixel, voxel size = 0.3/0.5/1.0 mm, aquisition time = 16 min 22 sec). Quantitative analysis of signal loss was then performed by counting the number of dark pixels per aortic slice.

In each slice, iron was then quantified by Inductively-Coupled Plasma Mass Spectrometry (ICP-MS, Perkin-Elmer, France) for the group injected with 150 µmol Fe/kg, and by ICP-AES for the other two doses. In each rabbit, 3 to 4 slices were not included in iron quantification as they were close to the iliac bifurcation and did not present any aortic lesion.

Statistical Analysis

Data are expressed as mean ± standard deviation (SD). Inter-observer reproducibility of the measurement of the vessel wall area was calculated as the SD of the differences in measurements between the two observers relative to the global mean value of the measurements (15).

For each contrast agent, changes in the wall area were compared between baseline and each following time points using a Wilcoxon signed rank test. Cross comparison between Ferumoxtran-10 and P904 at the different time points after injection (days 2 and 3 for P904 and days 7 and 10 for Ferumoxtran-10) were performed using a Mann-Whitney U test.

A value of $P<0.05$ was considered significant. Statistical analysis was performed using Intercooled Stata 10.0 (StataCorp LP, College Station, Texas, USA).

For the dose range study, a linear regression analysis was performed between the number of dark pixels and the iron dose values after their logarithm transform.

RESULTS

Efficacy of plaque imaging

In vivo MRI

Regarding the lumen signal, the low-dose injection at baseline produced an angiographic T1 effect for both products, showing aortic stenosis in the infrarenal aorta in all atherosclerotic rabbits (Figure 1, MRA). The high-dose (1,000 μmolFe/kg) injection of each contrast agent resulted in T2* effects leading to a total initial signal loss in the lumen followed by a progressive recovery related to the T1 effect as USPIO blood concentration decreased.

This secondary T1 effect occurred during the first 24 hours for P904 and was still visible 7 days post-injection for Ferumoxtran-10 (Figure 2). However, luminal signal recovery was not always persistent and a low-dose re-injection was necessary, to visualize the lumen accurately for 1 rabbit on day 1 and all 6 rabbits on days 2 and 3 with P904, and for 4 rabbits on day 10 with Ferumoxtran-10.

All images obtained with a short TE were deemed of good enough quality to be contoured, whereas most of the images with a long TE were not analyzable, because they presented strong susceptibility artifacts coming from the wall and the surrounding structures: e.g., USPIO trapped in the bone marrow of the vertebrae (Figure 1, T2*MRI).
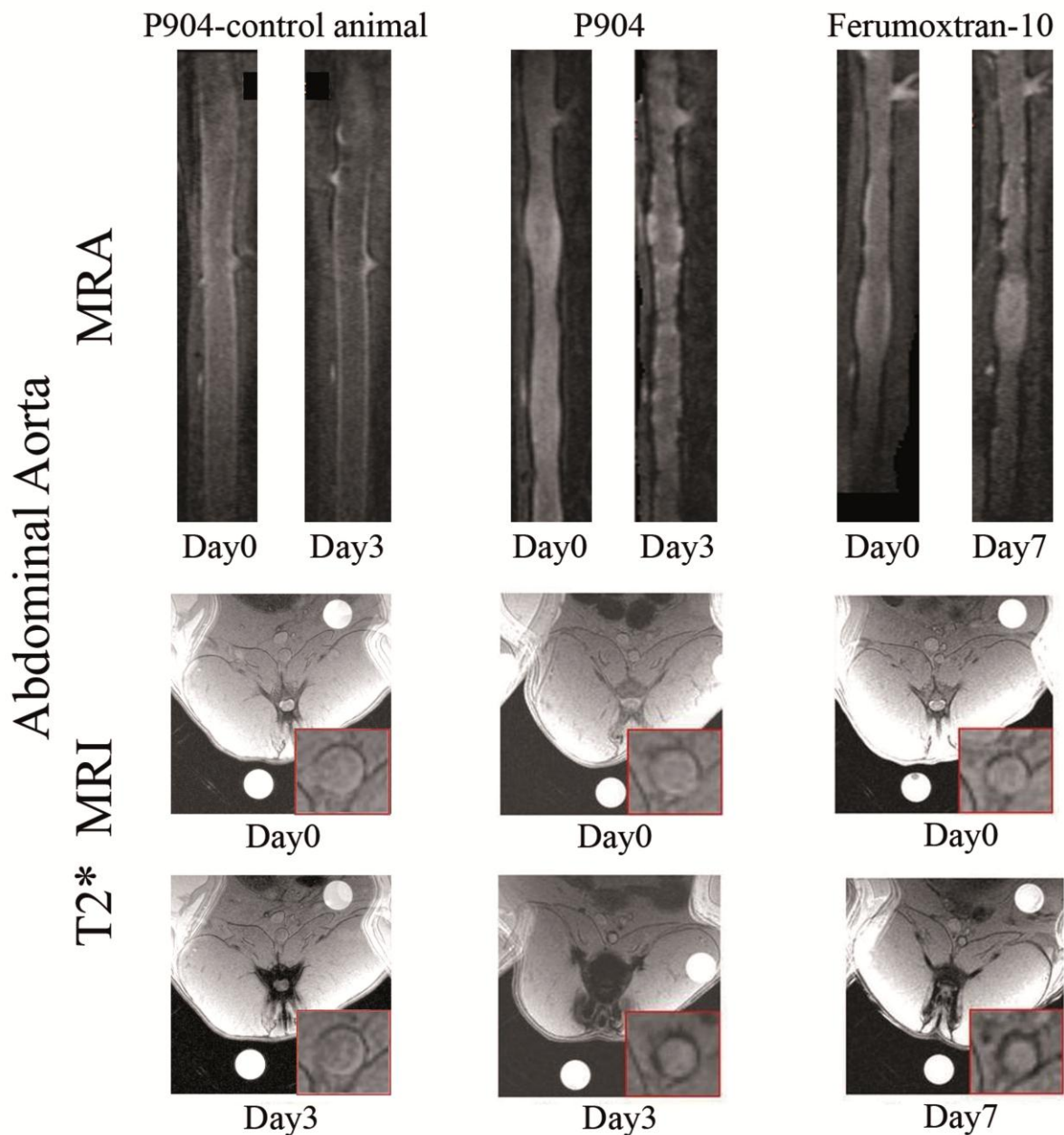
Figure 1. *MRA (coronal plane) and T2* weighted GE images (TE = 3.65 ms, axial plane) of the abdominal aorta with P904 on days 0 and 3 (control and atherosclerotic rabbits) and with Ferumoxtran-10 on days 0 and 7. Susceptibility artifacts in the vessel wall, due to the intra-plaque iron accumulation, are clearly visible on the post contrast images of atherosclerotic animals and absent for the control rabbit (insets - zoom of the aorta on T2*-w images).*
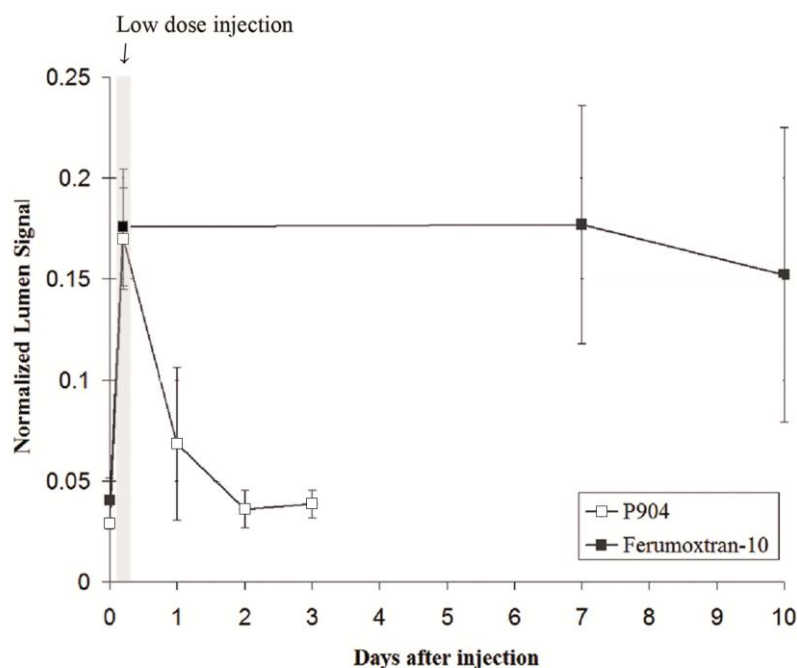
Figure 2. Normalized lumen signal intensity showing a similar angiographic T1 effect on day 0 immediately after the small dose (50 μmolFe/kg) injection for both products (highlighted region); all the other points of the follow up show the T1 effect of the high dose (1000 μmolFe/kg) injected at the end of the baseline MRI. This effect decreased rapidly for P904 and was almost undetectable as early as day 1.

The evolution of the signal in the vessel wall was the same with the two contrast agents but with an offset in time. With Ferumoxtran-10, mean vessel wall area at baseline, day 7 and day 10 was respectively 13.65±1.34, 19.6±6.44 and 18.18±6.4, corresponding to an increase of +44.5% (day 7; p=0.04) and of +34.8% (day 10; p=0.22) from baseline. Similarly with P904, the mean area was 16.35±3, 20.78±5.15 and 22.36±5.33 at baseline, day 2 and day 3, corresponding to an increase of 27.75% at day 2 (p=0.04) and of 38.81% at day 3 (p=0.04) (Figure 3). At day 1, the inner contour of the vessel was not assessable for 4 out of 6 rabbits (P904 group), because of susceptibility artifacts in the lumen.
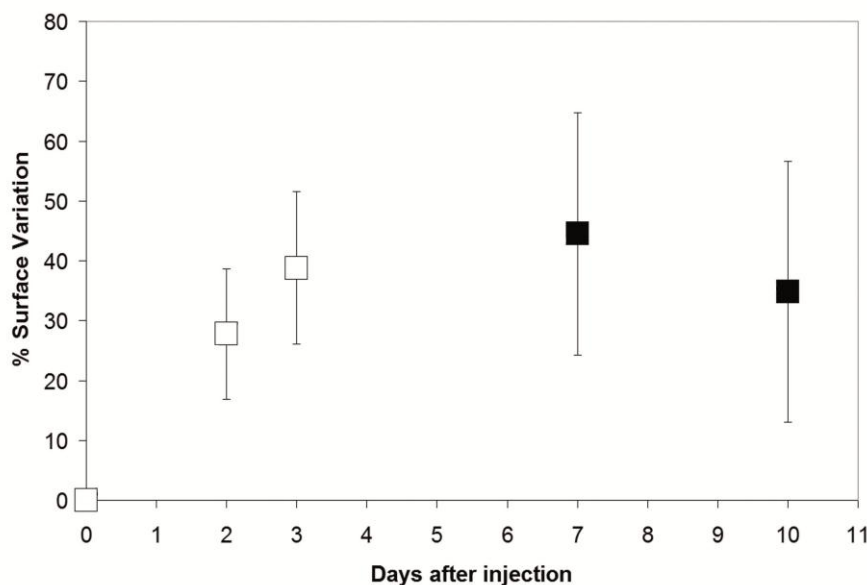
Figure 3. *Time course of the number of darkening pixels in the vessel wall for Ferumoxtran-10 (filled square) and P904 (open square). P904 induced effects were of approximately the same intensity as those induced by Ferumoxtran-10 but on a significantly shorter time scale. Data are shown as percentage (%) variation compared to baseline values before contrast agent infusion with the standard error of the mean (SEM).*

No significant difference in wall area was found between the two contrast agents in the cross-comparison statistical analysis: day 2/day 7 (p=0.52), day2/day10 (p=0.36), day3/day7 (p=0.27) and day3/day10 (p=0.14).

The inter-observer reproducibility was 71% (p<0.001) for vessel wall area measurement.

Histology

Control rabbits displayed neither plaque nor iron uptake on Perl's staining of the aorta (2 slices per animal). In all the other animals, the histological analysis showed mostly circumferential lesions (57% from 67 histological sections, corresponding to 6±2 slices per animal, N=11) with localized regions of particle accumulation deep in the plaques and also in the sub-endothelial area. Large foam cells were detected in abundance in the lesions. Perl's staining revealed presence of particles in plaques showing a certain degree of inflammation, with iron preferentially accumulating in regions containing eosinophile-type extracellular matrix, and not in highly fibrous regions (Figure 4). Immunohistochemistry with RAM11 monoclonal antibody revealed that the iron particles did not accumulate exclusively in the macrophage-rich regions, though numerous regions of co-localization were found in the plaque shoulder. There was no difference in this regard between the two products.
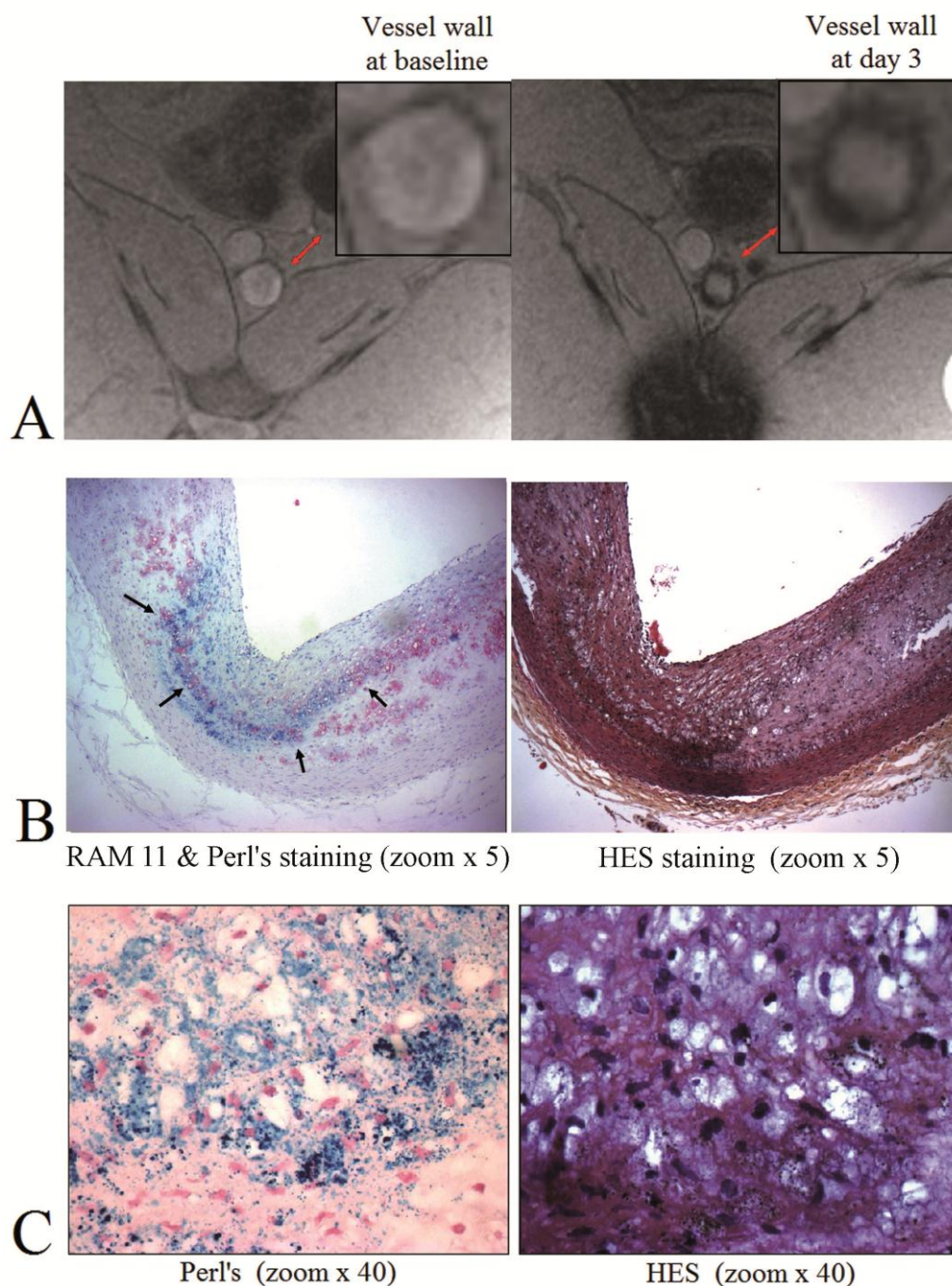
Figure 4. *(A) In vivo T2* GE images of the rabbit abdominal aorta at baseline (left) and 3 days after P904 injection. The insets represent magnified MR images of the aorta. (B) Corresponding immunohistological slice showing macrophages (in red with RAM11 immunostaining) and iron particles (in blue with Perl's) co-localization (left). HES staining shows that iron is preferentially accumulating in regions containing eosinophile-type extracellular matrix (right). The fleches indicate regions of free particles and macrophage colocalisation. (C) Higher magnification (x 40) histological images with Perl's (left) and HES (right) staining showing P904 particles accumulated inside large foam cells.*

Dose range study

The iron concentration measured by ICP in aortic slices increased significantly with dose: 0.81 ± 0.04 (n = 80), 1.32 ± 0.08 (n = 84) and 5.66 ± 0.47 (n = 83) µmol Fe/g of tissue, at 150, 350 and 1,000 µmolFe/kg respectively ($p<0.0001$ between each value interval). The serial *ex vivo* MR images showed that the number of pixels with signal loss was linearly correlated to the logarithm of their iron concentration ($p=0.0001$; R-square=0.93) (Figure 5).
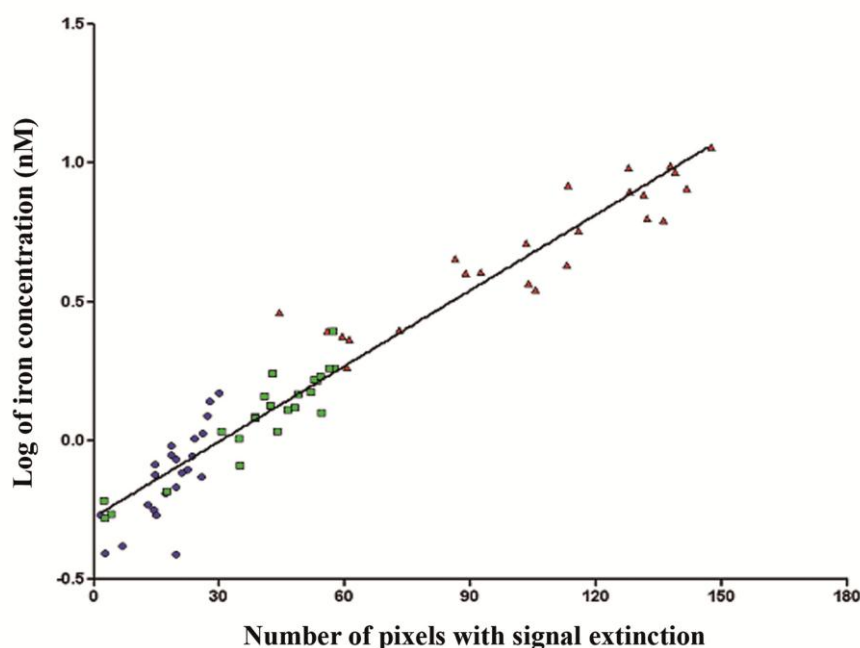

Figure 5. *Linear correlation between the number of pixels with ex vivo MRI signal loss and the logarithm of iron concentration in aortic slices following injection of P904. Circles, squares and triangles respectively represent the 150, 350 and 1000 doses. A linear regression line closely fits the data with an adjusted R-square of 0.93.*

DISCUSSION

We present here the first description of P904 for atherosclerotic plaque imaging.

Preliminary studies, performed on hyperlipidemic Watanabe rabbits, showed that Ferumoxtran-10 is accumulated early in atherosclerotic plaques. For a high dose, as used in the present study (1000 µmolFe/kg), intraplaque iron uptake was observed on Perl's staining as of 30 minutes post-injection (supplemental material, Guerbet Laboratories). Indeed, the major problem for post-iron-administration MRI is the strong T2* effect induced by the high concentration of circulating iron nanoparticles, which prevents visualization of the vessel wall. Our *in vivo* MRA and pharmacokinetic studies demonstrated that P904 was cleared from circulation much faster than Ferumoxtran-10, leading to earlier blood-signal recovery, enabling vessel wall analysis. A difference in the liver and spleen uptakes has been observed

between the two USPIOs (supplemental material, Guerbet Laboratories), which could potentially explain P904 faster clearance. As a result, a different imaging window, allowing vessel-wall visualization as of 24h post-injection was observed in this animal model, unlike with Ferumoxtran-10 (1, 2, 6).

However, it is conceivable that this faster blood clearance would impair contrast uptake in the atherosclerotic plaque (11, 16). Indeed, Yancy et al. (11), in an animal study comparing Ferumoxtran-10 and a product with faster clearance (Ferumoxytol: carboxy-methyl-dextran coated USPIO), observed reduced accumulation of the second product in the plaque. It was suggested that the period of plaque exposure to blood-circulating USPIO was the main factor for final intra-plaque USPIO accumulation. While this is probably true, the early accumulation observed in the present study demonstrated that other mechanisms are also playing important roles. First, particle size and coating are important (16). The smaller size and hydrophilic coating of P904 particles allowed effective accumulation at the lesion site by passive diffusion, as shown with Perl's staining on histology. Second, the intensity of macrophage uptake is an important point and may vary from one product to another. It has been previously shown that *in vitro* iron accumulation in human promonocytic cell line THP-1 is higher for P904 (1.8-2.3 pg Fe/cell) than for the above-mentioned Ferumoxytol (1.0-1.5 pg Fe/cell) (17).

The mechanisms leading to plaque contrast uptake remain unclear. It is still unknown whether iron particles are taken up in the blood by circulating monocytes or in the plaque by activated macrophages after passive diffusion. Furthermore, in the histological part of our study, almost all histological sections showed areas of co-localization of macrophages and iron particles. This supports the hypothesis that, while passive diffusion plays a role in USPIO accumulation in inflammatory plaque, active macrophage uptake is also an important mechanism for this phenomenon.

For *in vivo* imaging, a clinical multi-contrast protocol including MRA was favored to obtain a general view on the spatial extent of lesions, high-resolution proton density and T2* transversal scans for characterization of vessel wall signal intensity after iron uptake. The proposed protocol is easily transposable to human studies of the carotid arteries. Indeed, the study was performed on a clinical scanner and the duration of the acquisition did not exceed one hour, making this investigation compatible for human application. Furthermore, this particular animal model was chosen because the diameter of the abdominal aorta is close to that of human carotid arteries, making the spatial resolution of the imaging sequences well adapted to clinical investigation.

On MRA, the signal intensity in the lumen was similar, corresponding to the T1 effect, for the two agents immediately after the low-dose injection (50 μmolFe/kg). With the high dose (1000 μmolFe/kg), the peak T1 effect occurred during the first 24 hours post-injection for P904, compared day 7 for Ferumoxtran-10. This imaging window and the T1 effect have also been used for fresh thrombus detection using a carboxydextran coated USPIO (18). The present findings indicate an early imaging window for post-contrast vessel wall characterization with P904, compared to that found with Ferumoxtran-10 at 5 to 7 days post-injection, as shown in the present study and previous reports (6, 11).

The present study also emphasizes the importance of adapting the echo time to the intra-plaque iron concentration in order to obtain good quality images. We used a TE scout approach to cope with the problem of plaque variation, which leads to very different iron concentrations at the inflammation site, as demonstrated on histology and ICP analysis. In the case of high iron uptake, a long TE leads to overestimation of the susceptibility effect; thus a shorter TE proved to be better adapted.

Direct *in vivo* iron concentration quantification was not possible in our study, as combined effects produced by both extra- and intra-cellular iron particle populations caused T2 shortening and susceptibility responses of various intensities. However, the susceptibility-sensitive GE sequence of the *ex vivo* MRI enabled semi-quantitative assessment of local particle concentration. At 2.35 T, the detection of susceptibility artifacts induced by lower doses was possible. The relationship between the number of pixels with signal loss measured from T2*-w GE images and iron concentration was confirmed.

A limitation of the present study is the different imaging delay used for the two agents in the *in vivo* MRI study. However, previous studies performed on animal models showed that the optimal imaging window was 5 to 7 days post-injection for Ferumoxtran-10 (2, 6, 11). On earlier images, vessel wall visualization and analysis are prevented by high plasma concentrations. Another limitation is the fact that the clinical dose (45μmolFe/kg) was not tested as, for this animal model, the efficient dose with Ferumoxtran-10 ranges from 250 to 1000 μmolFe/kg. These higher doses are mandatory to increase the blood concentration of USPIOs in animals and compensate the inter-species differences in particle uptake efficiency of the reticulo-endothelial system.

In conclusion, **P904 allowed inflammation detection, in a rabbit model of atherosclerosis, as early as 24 hours post-administration, compared to the imaging window of 7 days previously shown with Ferumoxtran-10**. The faster blood pharmacokinetics did not prevent

particle accumulation at inflammation sites. Our study confirms that plaque inflammation detection is linked to both Ferumoxtran-10's and P904's ability to concentrate in atherosclerotic plaques. P904 allows an earlier visualization of contrast uptake in MRI, as its blood concentration decreases more rapidly. This significant reduction in the interval between USPIO injection and MR imaging could be the key factor for clinical use of iron oxide particles for this indication. We further propose a high-resolution multi-contrast MRI protocol adapted to the imaging of USPIO uptake in atherosclerotic plaques in animals, potentially easily transferable to human clinical studies of the carotid artery.

Practical Application

Although our research is pre-clinical, the proposed protocol can potentially be easily transposed to human studies of the carotid arteries and the spatial resolution of the imaging sequences is well suited to clinical investigations.

The present data indicates an early imaging window for post-contrast vessel wall characterization with P904 as compared to a later one (of 5 to 7 days post-injection) shown by the present data and literature with Ferumoxtran-10. It can be assumed that in patients, P904 may enable post-contrast imaging on the same day, compared to the 24-36 hours imaging delay with Ferumoxtran-10 (19).

Supplemental Material

P904 Pharmacokinetic Study

To determine the plasma pharmacokinetic parameters of P904 at different doses (150, 350 and 1000 µmol of iron per kilogram of body weight) (Table E1), blood samples from six hyperlipidemic New Zealand white rabbits that had been on a 0.3% cholesterol diet were taken at different times after the injection of P904. Plasma iron concentrations were measured at baseline (0 hour), at 0.5 hour, at 1 hour, and at 2, 6, 10, 13, 24, and 32 (highest single dose) hours after the injection by means of inductively coupled plasma atomic emission spectrometry (ICP-AES; Perkin-Elmer, France). With use of computer software (Kinetica; Innaphase, Philadelphia, Pa), plasma concentration curves were analyzed to determine the half-life, extrapolated area under the curve (expressed as a percentage), distribution volume (in milliliters per kilogram), and clearance (in milliliters per minute per kilogram) of P904; these measurements were compared with those for ferumoxtran-10 (Table 2).

At doses between 150 and 1000 µmol Fe/kg, the pharmacokinetic profile of P904 in the blood compartment, as compared with that of ferumoxtran-10, was associated with an increase in plasma clearance, whereas the distribution volume remained stable. This effect was dose dependent: The higher the dose, the longer the plasma half-life (Table 1).

Table 1. *Pharmacokinetic Parameters of Various Doses of P904 Injected in Hyperlipidemic Rabbits*

Parameter	Injected Dose		
	150 µmol Fe/kg	350 µmol Fe/kg	1000 µmol Fe/kg
Half-life (min)	136 ± 20	164 ± 9	220 ± 4
Distribution volume (mL/kg)	22 ± 2	22 ± 2	22 ± 0
Clearance (mL/min/kg)	0.06 ± 0.01	0.05 ± 0	0.04 ± 0

Table 2. *Pharmacokinetic Properties and Biodistributions of P904 and Ferumoxtran-10 in Healthy Rats*

USPIO	Plasma Half-life (min)	Plasma Clearance (mL/min/kg)	Postinjection Distribution in Liver (μmol Fe/g)*	Postinjection Distribution in Spleen (μmol Fe/g)*	Postinjection Distribution in Mesenteric Lymph Node (μmol Fe/g)*
P904	145 ± 28	0.2 ± 0.04	4.5 ± 0.2	9.5 ± 1.4	1.6 ± 1.2
Ferumoxtran-10	297 ± 31	0.09 ± 0.01	1.8 ± 0.0	4.5 ± 1.1	0.5

Note.---Data are pharmacokinetic properties and biodistributions of P904 and ferumoxtran-10 in healthy Sprague-Dawley rats injected with 200 μmol Fe /kg. Data are mean values ± standard deviations.
*Distributions of P904 and ferumoxtran-10 in liver, spleen, and mesenteric lymph node 120 minutes after injection.
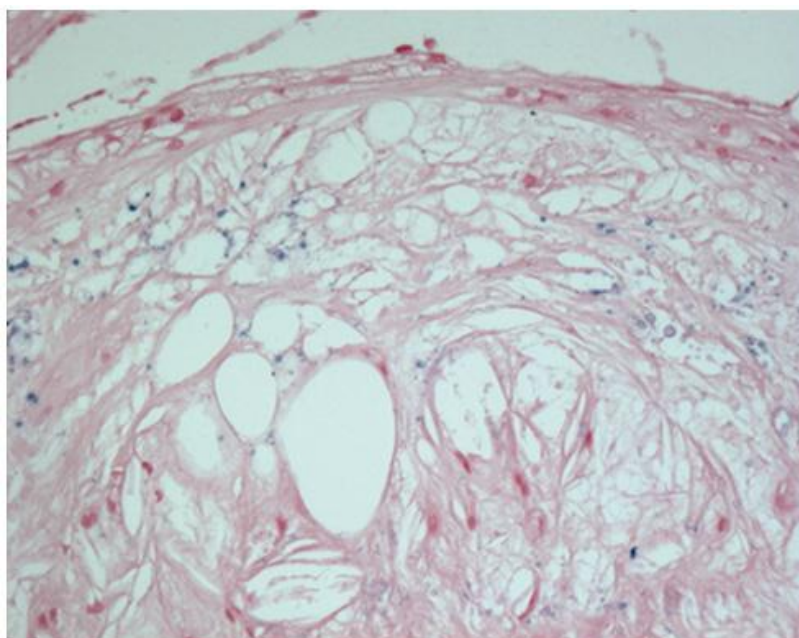

Figure 1*: Perl's-stained histologic aortic specimen from a Watanabe rabbit showing an early diffusion of ferumoxtran-10 particles into atherosclerotic plaques. Numerous particles are already present in all compartments of the lesion as early as 30 minutes after the injection. (Original magnification, ×20.)*
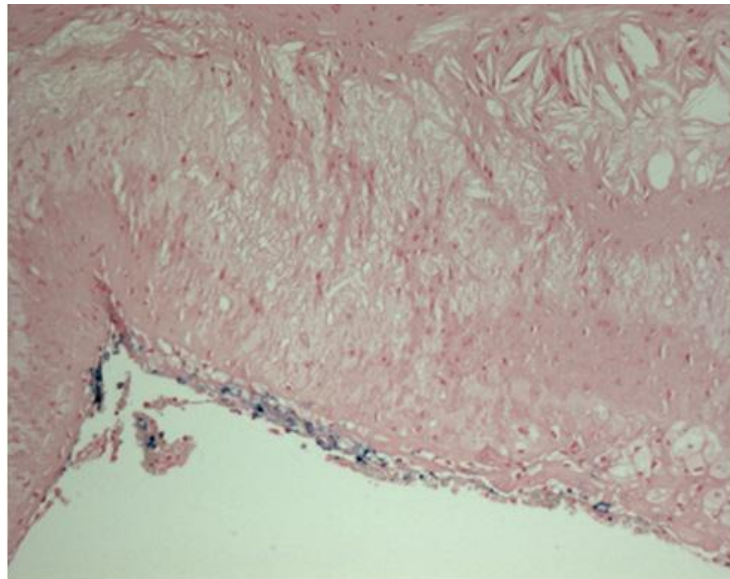
Figure 2*: Perl's-stained histologic aortic section from another Watanabe rabbit showing ferumoxtran-10 particles concentrated in the subendothelial region of the atherosclerotic plaque 4 hours after the injection. (Original magnification, ×10.)*

References:

1. Ruehm SG, Corot C, Vogt P, et al. Magnetic resonance imaging of atherosclerotic plaque with ultrasmall superparamagnetic particles of iron oxide in hyperlipidemic rabbits. Circulation 2001; 103:415-422.

2. Hyafil F, Laissy JP, Mazighi M, et al. Ferumoxtran-10-enhanced MRI of the hypercholesterolemic rabbit aorta: relationship between signal loss and macrophage infiltration. Arterioscler Thromb Vasc Biol 2006; 26:176-181.

3. Kooi ME, Cappendijk VC, Cleutjens KB, et al. Accumulation of ultrasmall superparamagnetic particles of iron oxide in human atherosclerotic plaques can be detected by in vivo magnetic resonance imaging. Circulation 2003; 107:2453-2458.

4. Trivedi RA, JM UK-I, Graves MJ, et al. In vivo detection of macrophages in human carotid atheroma: temporal dependence of ultrasmall superparamagnetic particles of iron oxide-enhanced MRI. Stroke 2004; 35:1631-1635.

5. Trivedi RA, Mallawarachi C, JM UK-I, et al. Identifying inflamed carotid plaques using in vivo USPIO-enhanced MR imaging to label plaque macrophages. Arterioscler Thromb Vasc Biol 2006; 26:1601-1606.

6. Herborn CU, Vogt FM, Lauenstein TC, et al. Magnetic resonance imaging of experimental atherosclerotic plaque: comparison of two ultrasmall superparamagnetic particles of iron oxide. J Magn Reson Imaging 2006; 24:388-393.

7. Korosoglou G, Weiss RG, Kedziorek DA, et al. Noninvasive detection of macrophage-rich atherosclerotic plaque in hyperlipidemic rabbits using "positive contrast" magnetic resonance imaging. J Am Coll Cardiol 2008; 52:483-491.

8. Claire Corot XV, Philippe Robert, Georgia Gagneur, Marc Port. Comparison of Different Types of Blood Pool Agents (P792, MS325, USPIO) in a Rabbit MR Angiography-like Protocol. Investigative Radiology 2003:311-319.

9. Schmitz SA, Coupland SE, Gust R, et al. Superparamagnetic iron oxide-enhanced MRI of atherosclerotic plaques in Watanabe hereditable hyperlipidemic rabbits. Invest Radiol 2000; 35:460-471.

10. Ruehm SG, Corot C, Vogt P, et al. Ultrasmall superparamagnetic iron oxide-enhanced MR imaging of atherosclerotic plaque in hyperlipidemic rabbits. Acad Radiol 2002; 9 Suppl 1:S143-144.

11. Yancy AD, Olzinski AR, Hu TC, et al. Differential uptake of ferumoxtran-10 and ferumoxytol, ultrasmall superparamagnetic iron oxide contrast agents in rabbit: critical

determinants of atherosclerotic plaque labeling. J Magn Reson Imaging 2005; 21:432-442.

12.   Durand E, Raynaud JS, Bruneval P, et al. Magnetic resonance imaging of ruptured plaques in the rabbit with ultrasmall superparamagnetic particles of iron oxide. J Vasc Res 2007; 44:119-128.

13.   Kawahara I, Nakamoto M, Kitagawa N, et al. Potential of magnetic resonance plaque imaging using superparamagnetic particles of iron oxide for the detection of carotid plaque. Neurol Med Chir (Tokyo) 2008; 48:157-161; discussion 161-152.

14.   Mansard CD, Canet Soulas EP, Anwander A, et al. Quantification of multicontrast vascular MR images with NLSnake, an active contour model: in vitro validation and in vivo evaluation. Magn Reson Med 2004; 51:370-379.

15.   Bland J, Altman D. Statistical methods for assessing agreement between two methods of clinical measurement. Lancet 1986; 1:307-310.

16.   Briley-Saebo KC, Mani V, Hyafil F, et al. Fractionated Feridex and positive contrast: in vivo MR imaging of atherosclerosis. Magn Reson Med 2008; 59:721-730.

17.   Corot C, Port M, Guilbert I, et al. Superparamagnetic Contrast Agents. In: Modo MMJ, Bulte JWM, eds. Molecular and Cellular MR Imaging: CRC Press Taylor & Francis Group, 2007; 60-78.

18.   Schmitz SA, Winterhalter S, Schiffler S, et al. USPIO-enhanced direct MR imaging of thrombus: preclinical evaluation in rabbits. Radiology 2001; 221:237-243.

19.   Trivedi RA, JM UK-I, Graves MJ, et al. Noninvasive imaging of carotid plaque inflammation. Neurology 2004; 63:187-188.

Chapter V

Assessment of age modulated vascular inflammation in ApoE-/-mice by USPIO-enhanced MRI

Assessment of age modulated vascular inflammation in ApoE-/- mice by USPIO-enhanced MRI

Monica Sigovan[1], Amine Bessaad[1], Hasan Alsaid[1], Eric Lancelot[2], Claire Corot[2], Bruno Neyran[1], Nicolas Provost[3], Zouher Majd[3], Magali Breisse[3], Emmanuelle Canet-Soulas[1]

[1]. Université Lyon 1, CREATIS-LRMN, UMR CNRS 5220, U630 INSERM, Lyon, France

[2]. GUERBET Group, Aulnay-sous-Bois, France

[3]. GENFIT, Lille, France

ABSTRACT

Objective: Inflammation within atherosclerotic lesions increases the risk for plaque rupture and thrombosis. A functional approach to plaque analysis is the intravenous administration of ultrasmall superparamagnetic particles of iron oxide (USPIO) that enables visualization of macrophages residing in the plaques. In this study we sought to characterize the age related inflammatory status associated with atherosclerosis lesion progression in ApoE$^{-/-}$ mice by USPIO-enhanced MRI.

Materials and Methods: 24 ApoE$^{-/-}$ mice were divided in four groups (N=6) and fed a high cholesterol diet from 6 weeks of age to the end of the protocol. One group per MR time point was investigated at **10, 16, 24 and 34 weeks of age**. Each MR examination was performed on a 4.7T scanner and consisted of baseline and 48h post-USPIO administration imaging sessions. P904, a USPIO contrast agent (Guerbet, Paris, France) with a potential for plaque macrophage targeting, was used.

Vessel wall area measurements were performed on high resolution spin echo images. Multi echo gradient echo images acquired with the same geometry were used to calculate T2* maps of the vessel wall using a pixel by pixel mono-exponential fit. A one-way ANOVA was performed to characterize the temporal variation of vessel wall area, susceptibility artifact area, baseline and post-USPIO T2* values. MR measurements were correlated with the histological findings.

Results: A significant increase was found in the aortic wall area from 1.4±0.2 at 10 weeks to 2±0.3 mm^2 at 34 weeks of age (P<0.05). Concerning the post-USPIO MRI, signal loss regions, with patterns spanning from focal to the complete disappearance of the vessel wall, were observed on all post-contrast images. A significant increase in the size of the

susceptibility artifact was observed from 0.5 ± 0.2 to 2.4 ± 1.0 at 24 weeks (P<0.05) and to 2.0 ± 0.9 mm^2 at 34 weeks (P<0.05).

The T2* values calculated on the 48h post-USPIO images were shorter compared to baseline. The decrease was 34 ± 16 % at 10 weeks, 57 ± 11 % at 16 weeks, 57 ± 16 % at 24 weeks and 48 ± 13 % at 34 weeks.

The Pearson's correlation test between measurement of aortic wall area performed on both MR images and histological analysis showed a statistically significant correlation (r = 0.695 and p < 0.05). A correlation was also obtained between the signal loss area and the macrophages covered area (r = 0.68 and p < 0.05).

Conclusions: This study demonstrated the feasibility of USPIO-enhanced MRI in assessing the inflammatory status related to the temporal progression of the atherosclerosis plaque in ApoE$^{-/-}$ transgenic mice model of atherosclerosis. In our experimental conditions, the vascular inflammation peak, for the ApoE -/- mice feeding high-fat/high-cholesterol diet is measured between 16 to 24 weeks of age.

Key Words: atherosclerosis; USPIO; rapid pharmacokinetics; ApoE$^{-/-}$ mouse.

INTRODUCTION

Inflammation within atherosclerotic lesions increases the risk of plaque rupture and thrombosis (1). A functional approach to plaque analysis is the intravenous administration of ultrasmall superparamagnetic particles of iron oxide (USPIO) that enables visualization of macrophages residing in the plaques. USPIO have been shown to accumulate in atherosclerotic plaques in carotid arteries of patients with clinically documented cardiovascular risk factors (2, 3).

The ApoE$^{-/-}$ mouse model develops atherosclerotic lesions similar to those found in human and has been extensively used to study factors affecting the size and composition of plaques (4). Age related lesion progression in the ApoE$^{-/-}$ mouse has been well documented by histological studies (5-7).

In addition, high-field MRI allows the non-invasive detection and characterization of lesions and their age related progression (8-11). Although the number of (U)SPIO-enhanced MRI studies performed in ApoE$^{-/-}$ mice is limited, growing evidence shows that this family of contrast agents can be used as a marker to detect inflammation at the atherosclerotic lesion (12, 13). However, assessing the inflammatory status of atherosclerotic lesions non-invasively *in vivo* represents a challenge to date. USPIO-enhanced MRI studies generally focused on the qualitative evaluation of the induced signal loss. Correlation between signal loss on MR images and iron positive staining on histological slides or local iron concentrations provides the validation for inflammation targeting (2, 3). A more quantitative MR method for assessing inflammation would be needed.

The characteristics of USPIO agents are best exploited with T2* weighted gradient echo sequences. Furthermore, T2* mapping techniques offer quantitative information on local iron concentrations (14). Currently there are no reports of T2* mapping applied *in vivo* for mouse models of atherosclerosis. Also, to our knowledge, a noninvasive follow up of the inflammatory status at the arterial wall has not yet been reported. The aim of the study was to characterize the age related inflammatory status related to atherosclerosis lesion progression in ApoE$^{-/-}$ mice by USPIO-enhanced MRI.

MATERIALS AND METHODS

Animal model

The protocol was approved by the animal experimentation Ethic Committee of Lyon1 University. A total number of 24 ApoE-/- mice (C57BL/6 background, Charles-River, France)

were used in the study. Animals were fed with a high-fat/high cholesterol diet (Western Diet, 0.5% cholic acid and 1.25% cholesterol, SSNIFF) at 6 weeks of age (mean body weight of 18 g at protocol initiation). The exclusion criterion was overall bad health of the animal due to the high-fat/high-cholesterol diet, however none had to be excluded.

MR investigations were performed at 4 time points on different groups of animals (N=6 per group). At each investigation point a baseline MRI session was followed by the administration of a USPIO agent (dose of 1mmolFe/kg) and a second imaging session was performed 48h post contrast. Mice were anesthetized by isoflurane 2 % for the induction and 1 % to maintain anaesthesia (TEM SEGA, Lormont, France) and kept under continuous monitoring of cardiac and respiratory rates during the entire imaging session. Body temperature was maintained using a circulating heated water blanket (Fischer Bioblock Scientific, Ilkirch, France). at the end of the post contrast MRI, while still under anaesthesia, mice were sacrificed by cervical dislocation and the aorta was removed for histological analysis.

Contrast agent

The P904, a USPIO contrast agent provided by Guerbet (Paris, France) was used in this study. The nanoparticles are composed of a maghemite crystalline core, coated with a low molecular weight amino-alcohol derivative of glucose. This type of coating represents approximately 2000 hydroxyl groups per nanoparticle. The relaxivities measured in water at 1.42 T and 37°C were $r_1 = 14$ mM^{-1}s^{-1} and $r_2 = 87$ mM^{-1}s^{-1} with a mean hydrated particle diameter of 21 nm. The agent is supplied in suspension at a concentration of 11.9 mg of iron per milliliter. Its plasma half-life in hyperlipidemic rabbits is 3.5 hours for a dose of 1000 μmolFe/kg (15).

MRI Protocol

The MR imaging system was a 4.7 Tesla Bruker magnet (Bruker Biospin GmbH, Rheinstetten, Germany) equipped with a 10 cm bore actively-shielded and 270 mT/m gradient set. An 'Alderman and Grant' home built emission-reception volume radio frequency (RF) coil (length=30 mm, inner diameter=26 mm) was used for good RF homogeneity over the volume of interest.

Double cardiac and respiratory gated acquisitions were obtained with a home built gating system developed in Matlab (The Mathworks Inc., Natick, MA, USA). Three patch electrodes placed on the animal's paws were used to collect the ECG signal and a pressure

sensor was used for the respiratory signal. Two reference tubes doped with Gadolinium DOTA (DOTAREM®, Guerbet 0.3µmol/ml) were positioned on the animal's side for signal intensity calibration.

A bright-blood cine-mode FLASH sequence was used for aortic arch localisation, performed on 7 transverse joined slices centred on the base of the heart. These reference slices were acquired with a gradient echo (GE) sequence (TR/TE = 1R-R interval / 6.7 ms, field of view (FOV) = 3.8×3.8 cm, matrix = 256×256, bandwidth (BW) = 25 kHz, slice thickness = 1.11 mm, number of averages (NA) =1). The same FLASH sequence was then used in an oblique plane to obtain a slice right above the aortic sinus perpendicular to the vessel wall. The parameters for the FLASH sequence were as follows: TR/TE = 10/ 2.7 ms, FOV = 3×3 cm, matrix = 128×128, BW = 25 kHz, slice thickness = 1 mm, NA = 4.

Morphologic information on the vessel wall was then gathered with two spin echo (SE) sequences with different T2 weightings. MRI parameters were: 0.8 mm slice thickness (transverse slice on the ascending aorta), with the high in-plane resolution of 98µm, with TR ~ 2500 ms, TEs = 12.4 and 24 ms, FOV = 2.5×2.5 cm, matrix = 256×256, BW = 100 kHz, NA = 2. Luminal signal suppression was performed with a trigger delay of 30 ms that enabled a synchronisation during systole. A saturation pulse was used to eliminate signal from fat and reduce chemical shift artefacts.

Using the same geometry a multi-echo GE sequence was used to assess USPIO accumulation. A double inversion recovery pulse was used to achieve black-blood contrast. The sequence was performed twice, to obtain 8 echo images, using the following parameters: TR ~ 1800 ms, TE1 = 5 and TE2 = 8 ms, ΔTE = 6.5 ms, inversion time (TI) for black-blood module = 700 ms, BW = 50.5 kHz, NA = 2.

The total duration of the MRI protocol was 2 hours.

Image analysis

Image analysis was performed using a dedicated software (Creatools) (16). Inner and outer vessel wall contours were delineated manually by one observer (M.S., 3 years experience) on the morphologic pre-contrast SE images (TE = 12.4 ms). The obtained ROIs (regions of interest) were then used for the analysis of the pre and post-contrast GE images. An adjustment by translation and rotation of the ROIs was performed when necessary. The induced susceptibility artifacts were assessed on the post-contrast GE images (acquired with the shortest TE) using a second manually drawn outer contour. Areas for the vessel wall and

the induced susceptibility artifact were measured in a ROI obtained by subtracting the inner from the outer contours.

The GE images were interlaced from the two acquisitions to have a better sampling of the signal decrease with TE. T2* maps were then calculated in Matlab (The MathWorks Inc, Natick, MA, USA) using a pixel by pixel mono-exponential fit. The goodness of the fit was also calculated and the pixels that gave a regression r < 0.7 were considered as having a T2* value lower than the detection limit and were set to 0 ms. The previously obtained ROIs for MR image analysis were used in Matlab on the calculated maps to get the T2* distribution and the mean T2* value in the plaque. The distributions were calculated as a percentage of the entire surface of the ROI taking into account values between 1 and 50 ms.

Histology

For analysis of atherosclerotic lesions in the ascending aorta, samples were harvested and fixed in Antigenfix (MicromMicrotech, France). The ascending aorta was then isolated, embedded in tissue medium (OCT Compound, Leica, Nanterre, France) and frozen on dry ice.

The samples were serially cut into 10μm sections, stained with Oil Red O (Merck, France) and then counterstained with hematoxylin (Labonord, Templemars, France) to identify the presence of atherosclerotic lesions. For immunohistochemical analysis, macrophages were detected with rat anti-mouse CD68 antibody (AbD Serotec, Düsseldorf, Germany). The sections were incubated 2 hours at room temperature with CD68 antibody (1:100) and, after incubation at room temperature for one hour, revealed by a Cy3-labeled secondary antibody (1:200, Jackson IR, Suffolk, UK).

Images were acquired using an Olympus IX81 microscope coupled to a ColorviewII digital camera and analyzed with a Cell^F associated software (Olympus, France). The aortic wall areas were measured and expressed in mm². Macrophage content in aortic wall was determined after the analysis of the CD68 signal area (expressed in mm²).

Statistical Analysis

A second observer (EC, 10 years of experience) drew internal and external vessel wall contours for 10 randomly chosen animals. The variability for vessel wall area measurement was calculated with a paired two-tailed student's t test and reproducibility between observers was estimated by correlation coefficient and coefficient of variation. The relationship between MR measurements and aortic wall area was evaluated by regression analysis, as well as the

relative area of signal loss and measured macrophage area. One image per animal was analyzed for both MRI and histopathology.

For each time point, the independence between baseline and post-USPIO histograms was compared using a Pearson's chi-square test. The temporal variation of the vessel wall areas, signal loss areas and mean T2* values of plaques for both baseline and post-USPIO was analyzed with an ANOVA test. Differences were considered significant when $P<0.05$. Data are expressed as mean ± standard deviation (SD).

RESULTS

The authors had full control of all data and information submitted for publication.

At the first imaging point 4 out of 6 animals underwent MRI; one mouse died after USPIO administration at the second time point. The actual number of animals analysed in the study is presented in Table 1.

Table 1. Study design showing the actual number and age of animals that underwent MR imaging sessions

Time Point	I	II	III	IV
No. of Animals	4	5	6	6
Diet Duration	4 weeks	10 weeks	18 weeks	28 weeks
Age	10 weeks	16 weeks	24 weeks	34 weeks

Plaque development evaluation

All obtained images were analyzed, owing to a good performance of the double cardiac and respiratory gating system. Figure 1 (left) shows representative MR morphological T2-w images acquired over the duration of the study on different animals for each time point. Baseline images showed a progressive increase of the vessel wall thickness and heterogeneity of signal with occurrence of hypo-intense regions indicating calcifications at 34 weeks of age. Histology slides showed a thickening of the aortic wall with formation of complex lesions, with large lipid deposits, possible calcifications and accumulation of macrophages (Figure 1, right).
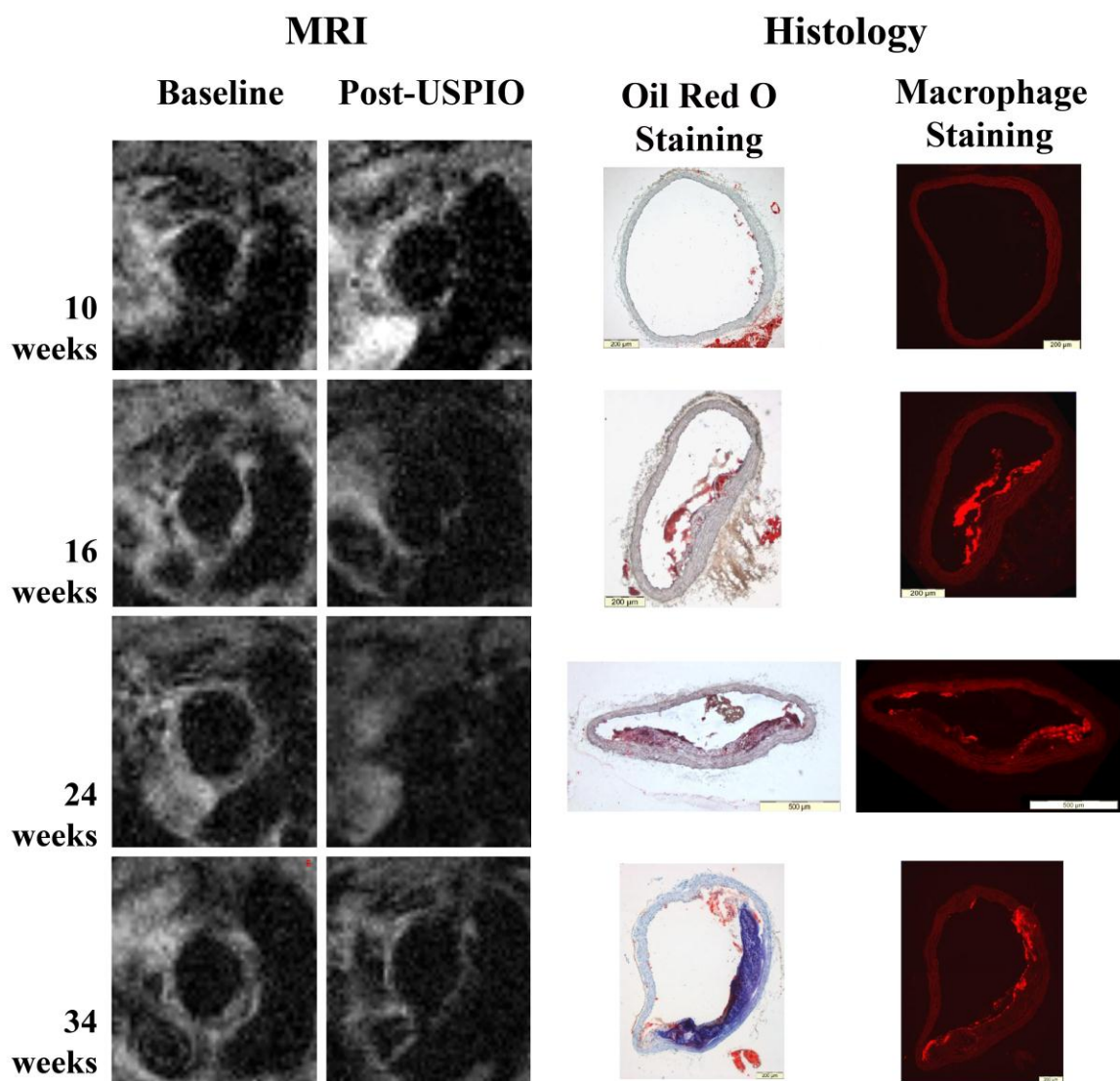
Figure 1. *MR and histological images from the ascending aorta from animals representing the different stages of plaque development. Baseline morphologic black-blood spin-echo images (left row) show an increasingly thicker aortic wall. Histological slides stained with Oil Red O reinforced with hematoxylin show lipid rich lesions starting with 16 weeks. All post USPIO images obtained 48h after administration show signal loss regions inside the vessel wall. Immunohistochemical staining of CD68 reveals the presence of macrophages in the aortic lesions. The macrophage staining corresponds to the signal loss area on MR images*

A significant increase was measured in the aortic wall area from 1.4±0.2 at 10 weeks to 2±0.3 mm^2 at 34 weeks of age (p<0.05). The Pearson's correlation test between measurements performed on MR images and histology slides showed a good and statistically significant correlation for vessel wall surface (r = 0.695 and p < 0.05, Figure 4 A).
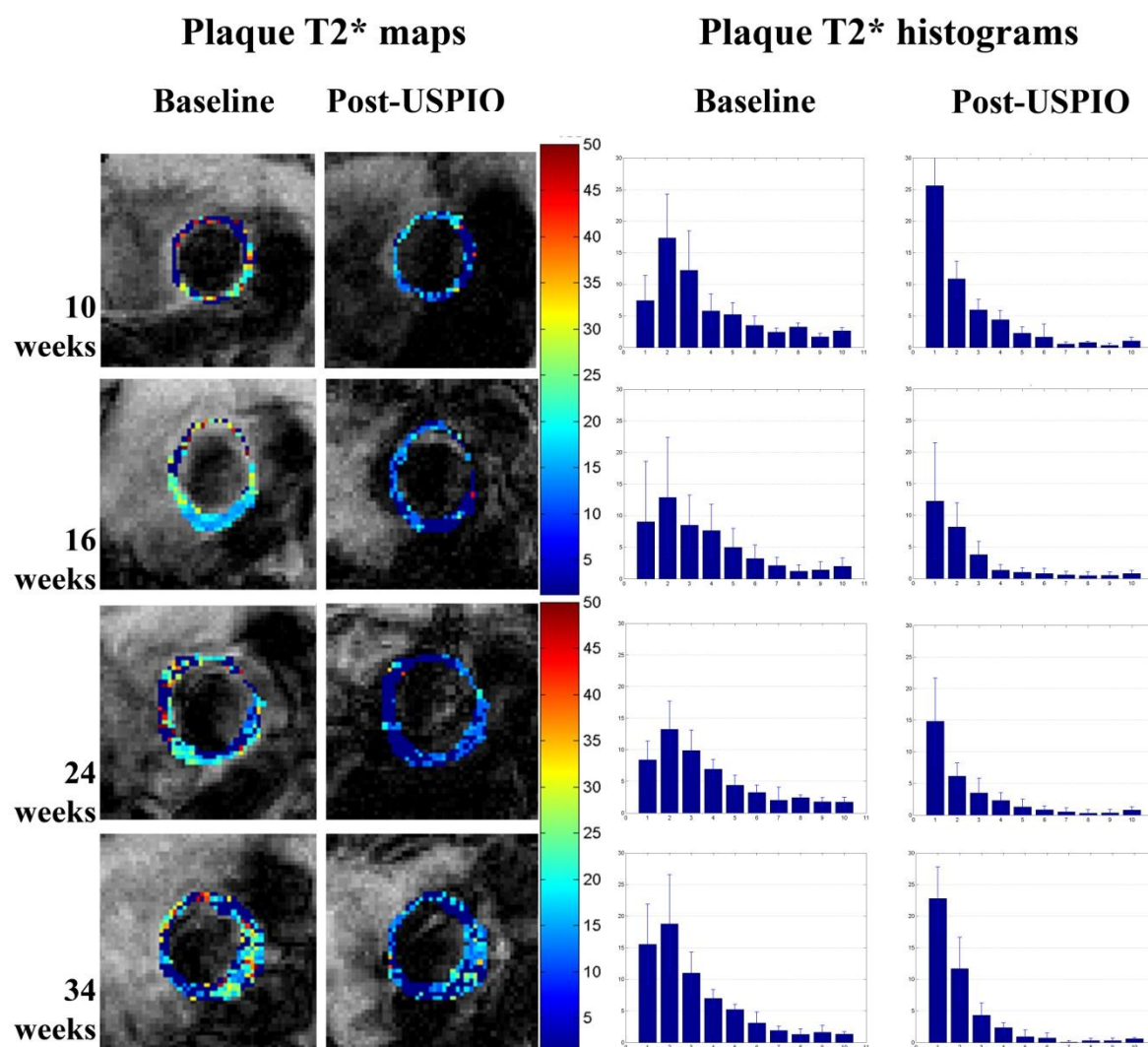
Inflammation evaluation

Figure 2. Left: Overlay of T2* maps of the vessel wall on anatomic GE images. Maps were calculated from baseline and 48h post-USPIO images. The colorbar represents T2* values in ms and the value 0 was given to the pixels that could not be fitted (r<0.7). Right: Mean histograms over all investigated animals at each time point showing the distribution of T2* values (between 1 and 50 ms, intervals of 5 ms) as a percentage of the entire vessel wall area (scale from 0 to 30%). Data is represented as mean ± SD.

Concerning the post-USPIO MRI performed 48h after contrast administration, signal loss regions, with patterns spanning from focal to the complete disappearance of the vessel wall, were observed on all post-contrast images (Figure 1, post-USPIO). A significant increase in the size of the susceptibility artifact was observed from 0.5±0.2 to 2.4±1.0 at the third time point ($p<0.05$) and to 2.0±0.9 mm^2 at the last ($p<0.05$). The size of the susceptibility artifact was greater than the size of the vessel wall for a number of animals (5 out of 5 mice at the third time point, 4 out of 6 mice at the fourth and 2 out of 6 mice at the

last). Furthermore, a statistically significant correlation was obtained between the signal loss area and the macrophage covered area both measured in mm^2 (r = 0.68 and $p < 0.05$, Figure 4 B).
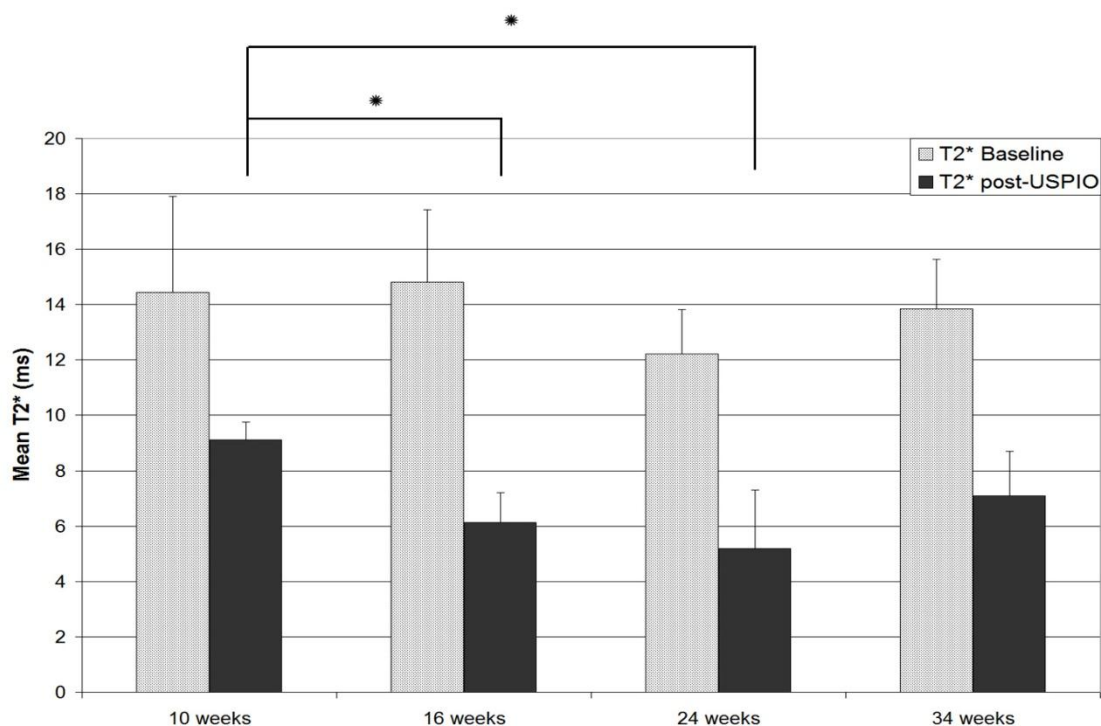

Figure 3. *Temporal variation of the mean T2* values of the vessel wall calculated on baseline and 48h post-USPIO images. Data is presented as mean ± SD. (* - p<0.05)*

An overlay of plaque T2* values on anatomic GE images is provided in Figure 2. Baseline T2* maps provided a view of the temporal modification of vessel wall components indicating that lesions tend to become more heterogeneous as the aortic wall thickness increases (Figure 2). Mean T2* values calculated at every time point are represented in figure 3. The T2* values calculated on the post-USPIO images were shorter compared to baseline and showed a significant temporal variation. The decrease was 34±16 % at 10 weeks, 57±11 % at 16 weeks, 57±16 % at 24 weeks and 48±13 % at 34 weeks.
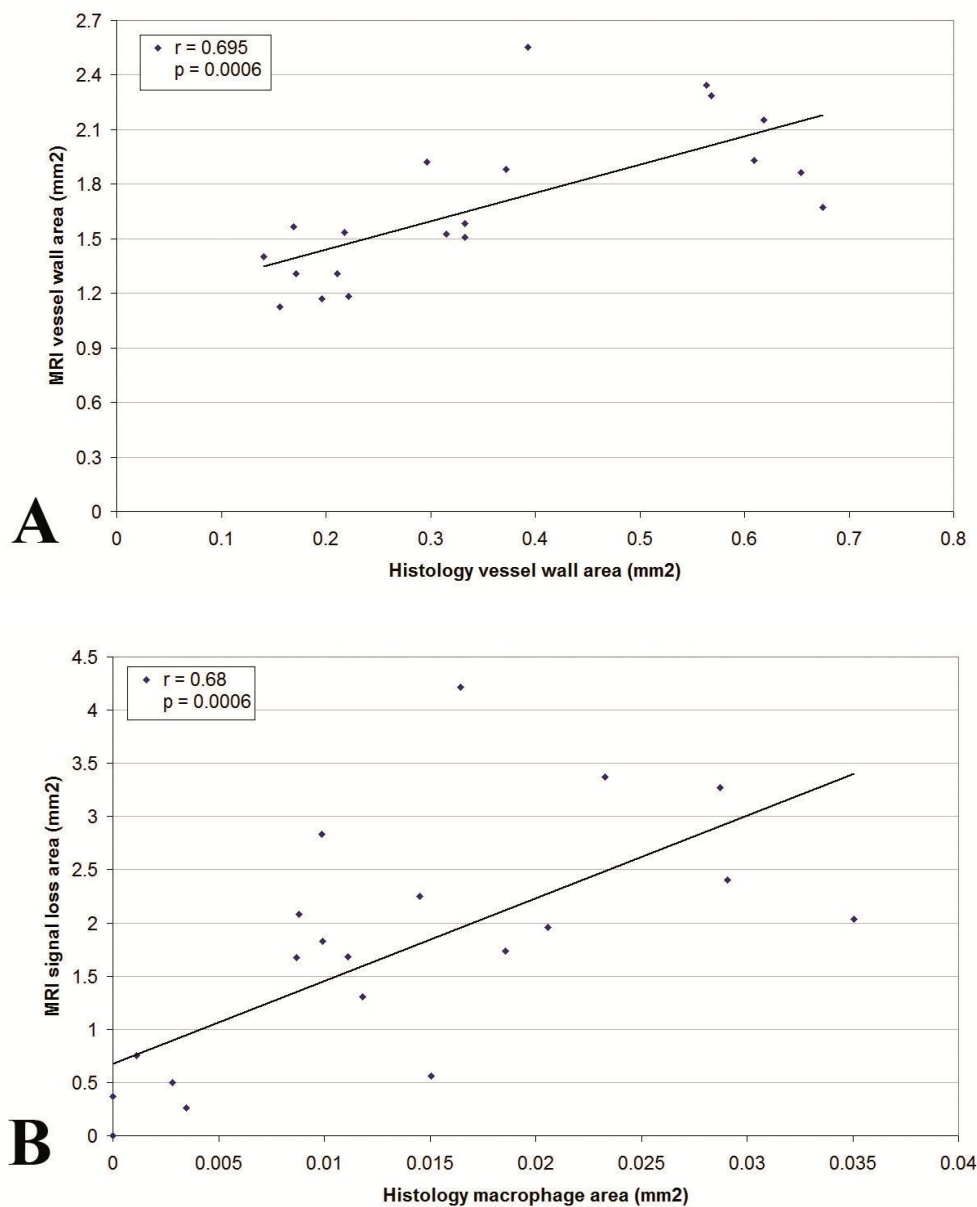
Figure 4. *Linear regression analysis showing a correlation between (A) vessel wall areas measured on SE MR images and aortic wall area determined by histological analysis; (B) signal loss area measured on GE MR images and macrophage positive staining area. All measurements were performed on cross-sectional images of ascending aorta of ApoE$^{-/-}$ mice and values are presented in mm^2.*

There was no inter-observer difference for vessel wall measurements (P = 0.13) on baseline images and post-USPIO contouring (P = 0.56), with good correlation coefficients (r = 0.94 p < 0.001 and CV = 3.99, r = 0.64, p = 0.04 and CV = 2.29 respectively).

DISCUSSION

The present study demonstrates that USPIO-enhanced MRI enables the assessment of macrophage accumulation indicating the inflammatory state related to temporal lesion progression in ApoE-/- mice.

For this animal model, lesion progression has been demonstrated in earlier studies (10). Kober et al. measured the aortic wall thickness in ApoE$^{-/-}$ mice up to 26 weeks of age. Using the same calculation method for wall thickness as described in the previously mentioned study, we found slightly higher values, with differences of about one pixel (data not shown). This is most likely due to partial volume effects induced by our larger slice thickness, adapted for the lower field strength.

In a histological study performed on ApoE-/- female mice, 6 days after intravenous administration the SPIO agent (Feridex, Berlex Laboratories) Litovsky et al. showed predominantly a superficial localization in the sub-endothelium area of plaques. Most of the lesion area was free of iron. In addition, thin areas of iron-laden macrophages were found just above the elastic lamina (12). Morris et al. showed for the first time that MRI can be applied to visualize macrophages non-invasively using a USPIO contrast agent in ApoE$^{-/-}$ mice (13).

We performed post-USPIO imaging at 48h post-administration because P904 is a rapid pharmacokinetics product that has been shown to accumulate as early as 24 to 48h in induced atherosclerotic plaques in rabbits (15). Concerning the post-USPIO images, signal loss regions indicating iron accumulation at the lesion site were observed in all images, spanning from localized regions to "blooming" artifacts larger than the vessel wall. The "blooming" artifacts were seen starting with the third time point, for all mice (5 out of 5), and then in fewer animals for the last two points. These results indicate an age related modulation of atherosclerotic plaque inflammation. The inflammatory status decreases at the final point. This finding is supported by T2* analysis.

To our knowledge, plaque T2* values have not been measured before *in vivo* in mice. In a study performed recently by Gert et al., *ex vivo* T2* mapping was performed on samples taken from ApoE$^{-/-}$ mice at different intervals post-USPIO administration (17). Normalized T2* were calculated, thus there are no actual T2* values available for plaque components. Recently, non-contrast enhanced MR T2* mapping was used in patients to distinguish between plaques that produce symptoms from asymptomatic ones using the susceptibility of endogenous iron. Although the local concentration was similar, it was assumed that changes in the iron form, like the aggregation, were responsible for the different susceptibility effects.

This first report on the susceptibility of human plaques, performed at 1.5T found mean T2* values of around 34 ms for asymptomatic lesions and around 20 ms for the symptomatic ones (18).

In the present study, measuring the percentage of pixels for T2* intervals in relation to the entire plaque area represents a robust method of characterisation, since it filters out the influence of plaque growth. The shift towards lower T2* values observed in the baseline histogram at the last imaging time point (34 weeks) could indicate a change in plaque composition. Shorter T2* components, such as calcifications and cartilage, might become more abundant. Concerning the post-USPIO measurements, higher iron concentrations can be assumed at the second and third time points on account of the significant decrease of the post-USPIO mean plaque T2* values, since T2* values decrease with increasing iron concentrations (14). This indicates that in our experimental conditions the highest macrophage staining representing lesion inflammation is measured between 16 and 24 weeks of age.

In a recent drug evaluation study on atherosclerosis progression Nagy et al. observed peak vascular inflammation at 10 to 14 weeks of age in ApoE$^{-/-}$ male mice. However, the animals were kept under a different diet (21% saturated fats and 0.15% cholesterol) than the one used in our study (0.5% cholic acid and 1.25% cholesterol) (19).

The dose of P904 used in the study, although 20 times higher than the accepted clinical dose for another USPIO (2), is a typical dose used in animal studies, as evidenced by the different pharmacokinetic properties and lack of toxic effects (15).

One limitation of the current study is the minimum TE (5 ms) imposed by the chosen spatial resolution used for the GE acquisitions. This limits the T2* values that can be measured. To compensate for this, a condition was set for the goodness of fit during the T2* calculations and only pixels with a T2* equal or higher than 1 ms were taken into account. An improvement in this technique of T2* mapping for post-USPIO MRI would be the use of very short echo time sequences, such as partial echo acquisition and UTE (ultrashort TE). A recently developed spin echo based technique allows the measurement of very short T2* of species with relatively long T2, adapted for magnetically labeled cell imaging (14). However, the long scan time is not compatible with our *in vivo* application. Another limitation is that only one slice was acquired and analyzed and may not be representative for the T2* distribution of the plaque.

In summary, the present study shows for the first time a follow up evaluation of the inflammatory status associated to atherosclerosis plaque development by non invasive

contrast enhanced MR imaging. The inflammatory status evaluation was performed using an established marker for inflammation represented by the USPIO agent P904. In conclusion, these findings open the way for follow up studies of therapeutic agent evaluation.

References:

1. Fuster V, Moreno PR, Fayad ZA, et al. Atherothrombosis and high-risk plaque: part I: evolving concepts. J Am Coll Cardiol 2005; 46:937-954.

2. Trivedi RA, JM UK-I, Graves MJ, et al. In vivo detection of macrophages in human carotid atheroma: temporal dependence of ultrasmall superparamagnetic particles of iron oxide-enhanced MRI. Stroke 2004; 35:1631-1635.

3. Trivedi RA, Mallawarachi C, JM UK-I, et al. Identifying inflamed carotid plaques using in vivo USPIO-enhanced MR imaging to label plaque macrophages. Arterioscler Thromb Vasc Biol 2006; 26:1601-1606.

4. Meir KS, Leitersdorf E. Atherosclerosis in the apolipoprotein-E-deficient mouse: a decade of progress. Arterioscler Thromb Vasc Biol 2004; 24:1006-1014.

5. Zhang SH, Reddick RL, Piedrahita JA, et al. Spontaneous hypercholesterolemia and arterial lesions in mice lacking apolipoprotein E. Science 1992; 258:468-471.

6. Zhang SH, Reddick RL, Burkey B, et al. Diet-induced atherosclerosis in mice heterozygous and homozygous for apolipoprotein E gene disruption. J Clin Invest 1994; 94:937-945.

7. Reddick RL, Zhang SH, Maeda N. Atherosclerosis in mice lacking apo E. Evaluation of lesional development and progression. Arterioscler Thromb 1994; 14:141-147.

8. Hockings PD, Roberts T, Galloway GJ, et al. Repeated three-dimensional magnetic resonance imaging of atherosclerosis development in innominate arteries of low-density lipoprotein receptor-knockout mice. Circulation 2002; 106:1716-1721.

9. Wiesmann F, Szimtenings M, Frydrychowicz A, et al. High-resolution MRI with cardiac and respiratory gating allows for accurate in vivo atherosclerotic plaque visualization in the murine aortic arch. Magn Reson Med 2003; 50:69-74.

10. Kober F, Canault M, Peiretti F, et al. MRI follow-up of TNF-dependent differential progression of atherosclerotic wall-thickening in mouse aortic arch from early to advanced stages. Atherosclerosis 2007; 195:e93-99.

11. Herold V, Wellen J, Ziener CH, et al. In vivo comparison of atherosclerotic plaque progression with vessel wall strain and blood flow velocity in apoE(-/-) mice with MR microscopy at 17.6 T. Magma 2009; 22:159-166.

12. Litovsky S, Madjid M, Zarrabi A, et al. Superparamagnetic iron oxide-based method for quantifying recruitment of monocytes to mouse atherosclerotic lesions in vivo: enhancement by tissue necrosis factor-alpha, interleukin-1beta, and interferon-gamma. Circulation 2003; 107:1545-1549.

13. Morris JB, Olzinski AR, Bernard RE, et al. p38 MAPK inhibition reduces aortic ultrasmall superparamagnetic iron oxide uptake in a mouse model of atherosclerosis: MRI assessment. Arterioscler Thromb Vasc Biol 2008; 28:265-271.

14. Kuhlpeter R, Dahnke H, Matuszewski L, et al. R2 and R2* mapping for sensing cell-bound superparamagnetic nanoparticles: in vitro and murine in vivo testing. Radiology 2007; 245:449-457.

15. Sigovan M, Boussel L, Sulaiman A, et al. Rapid-clearance iron nanoparticles for inflammation imaging of atherosclerotic plaque: initial experience in animal model. Radiology 2009; 252:401-409.

16. Mansard CD, Canet Soulas EP, Anwander A, et al. Quantification of multicontrast vascular MR images with NLSnake, an active contour model: in vitro validation and in vivo evaluation. Magn Reson Med 2004; 51:370-379.

17. Klug K, Gert G, Thomas K, et al. Murine atherosclerotic plaque imaging with the USPIO Ferumoxtran-10. Front Biosci 2009; 14:2546-2552.

18. Raman SV, Winner MW, 3rd, Tran T, et al. In vivo atherosclerotic plaque characterization using magnetic susceptibility distinguishes symptom-producing plaques. JACC Cardiovasc Imaging 2008; 1:49-57.

19. Nagy N, Melchior-Becker A, Fischer JW. Long-term treatment with the AT1-receptor antagonist telmisartan inhibits biglycan accumulation in murine atherosclerosis. Basic Res Cardiol 2009.

Chapter VI

Anti-angiotensin drug evaluation in ApoE$^{-/-}$ mice by USPIO-enhanced MRI at 7T

Anti-angiotensin drug evaluation in ApoE-/- mice by USPIO-enhanced MRI at 7T

Monica Sigovan[1], Amine Bessaad[1], Elena Kaye[2], Eric Lancelot[3], Claire Corot[3], Nicolas Provost[4], Zouher Majd[4], Magali Breisse[4], Emmanuelle Canet-Soulas[1]

1. Université Lyon 1, CREATIS-LRMN, UMR CNRS 5220, U630 INSERM, Lyon, France
2. Stanford University, Radiology Department, The Richard M. Lucas Center for Imaging
3. GUERBET Group, Aulnay-sous-Bois, France
4. GENFIT, Lille, France

INTRODUCTION

The renin-angiotensin system (RAS) plays an important role in the pathogenesis of atherosclerosis by promoting a series of coordinated cellular and molecular events observed in atherosclerotic lesions (1). Blocking the renin-angiotensin system (RAS) results in a decrease of atherosclerosis lesion formation and periadventitial inflammation in the same model (2).

The apolipoprotein E deficient (ApoE-/-) mouse develop severe hypercholesterolemia and extensive atherosclerotic lesions on chow diet, similar to those found in humans. Lesion formation is accelerated by a high cholesterol high fat diet.

In this study we investigated the effect of an angiotensin inhibitor on the development of atherosclerosis was determined non-invasively in the apolipoprotein (apo) E-deficient mice by high resolution MRI follow up study.

MATERIALS AND METHODS

Animal model

33 ApoE-/- female mice (C57BL/6 background) were included in the study (C57BL/6 background, Charles-River, France). Animals were divided in two groups (N=17 and N=16) and started on a high-fat diet (Western Diet, 0.5% cholic acid and 1.25% cholesterol) at 6 weeks of age (start mean weight of 19 g). An anti-angiotensin drug was added to the diet of one group of animals. Overall bad health was considered as the exclusion criterion; however no animals had to be excluded.

Seven animals from each group (Treated group – TG and Not Treated group - NTG) were investigated during three MR time points, at 10, 24 and 38 weeks of age. At each time point a baseline MRI session was followed by the administration of an USPIO agent and a second imaging session was performed 48h post contrast. A dose of 250 µMFe/kg was administered at the first imaging point and a dose of 1000 µMFe/kg at the second and third imaging points. During the second imaging point, 6 animals (N=3 not treated and N=3 treated) were administered the contrast agent twice, they received a dose of 250 µMFe/kg and underwent 48h post-USPIO MRI and a week later they received a second injection of a dose of 1000 µMFe/kg and underwent a third imaging session 48h after the last administration. For the MR investigations mice were anesthetized by isoflurane 2 % for the induction and 1 % to maintain anaesthesia (TEM SEGA, Lormont, France) and kept under continuous monitoring of cardiac and respiratory rates during the entire imaging session. Body temperature was maintained by heated water circulation (Fischer Bioblock Scientific, Ilkirch, France). At every time point 2 animals from each group that did not undergo imaging were sacrificed and at the end of the MRI follow-up all remaining animals were sacrificed, blood samples were taken for plasma lipid dosing and aorta samples were taken for histology. Study protocol was approved by the animal experimentation Ethic Committee of our Institution.

Contrast agent

The P904, a USPIO contrast agent provided by Guerbet (Paris, France), was used in this study. The nanoparticles are composed of a maghemite crystalline core, coated with a low molecular weight amino-alcohol derivative of glucose. Relaxivities measured in water at 1.42 T and 37°C are $r_1 = 14$ mM^{-1}s^{-1} and $r_2 = 87$ mM^{-1}s^{-1} with a mean hydrated particle diameter of 21 nm.

MRI Protocol

MR imaging was performed on a 7 Tesla Bruker small animal magnet (Bruker Biospin GmbH, Rheinstetten, Germany) equipped with a 12 cm bore actively-shielded and 400 mT/m gradient set. A volume emission-reception radio frequency (RF) coil (length = 150 mm, inner diameter = 33 mm) was used.

The cardiac signal was collected and filtered through a ECG Trigger Unit V2.0 (RapidBiomedical, GmbH, Rimpar, Germany); a pressure sensor was used for the respiratory signal. Double cardiac and respiratory gated acquisitions were obtained with a home built gating system developed in Matlab (The Mathworks, Inc., Natick, MA). One reference tube

doped with Gadolinium DOTA (DOTAREM®, Guerbet 0.3µmol/ml) was positioned over the animal's thoracic cage for signal intensity calibration.

Aortic arch localisation was performed as described previously (Reference Study IV). Morphologic information on the vessel wall was were obtained with a spin echo (SE) sequence with the following parameters: TR ~ 1600 ms, TE = 8.75, 17.5 and 26 ms (3 echo images), 0.8 mm slice thickness (transverse slice on the ascending aorta), pixel size 98 µm, FOV = 2.5×2.5 cm, matrix = 256×256, BW = 79.3 kHz, NA = 2. A saturation pulse was used to eliminate signal from fat and reduce chemical shift artefacts. Blood signal suppression was enabled by the gated acquisition and no supplemental techniques were needed. Using the same geometry a multi-echo GE sequence was used to asses USPIO accumulation. A double inversion recovery pulse was added to achieve black-blood contrast. The sequence was performed twice, to obtain 12 echo images, using the following parameters: TR ~ 742 ms, TE1 = 2.1 and TE2 = 2.5 ms, ΔTE = 5.1 ms, inversion time (TI) for black-blood module = 700 ms, BW = 79.3 kHz, NA = 2.

The total duration of the MRI protocol was one and a half hours.

Image analysis

Image analysis was performed using a dedicated software (Creatools) (2). Inner and outer vessel wall contours were delineated manually by one observer (M.S., 3 years experience) on the gradient echo image obtained with the shortest (TE = 2.1 ms) taking into account all available image series. A vessel wall ROI (regions of interest) was obtained by subtracting the two contours and was then used for surface measurements. An adjustment by translation and rotation of the ROI was performed when necessary.

The GE images were interlaced from the two acquisitions for a better sampling of the signal decrease with TE. $T2^*$ maps were then calculated in Matlab using a pixel by pixel mono-exponential fit. The goodness of the fit was also calculated and the pixels that gave a regression $r < 0.7$ were considered as having a $T2^*$ value lower than the detection limit and were set to 0 ms. The previously obtained ROI was used in Matlab, on the calculated map to get the mean $T2^*$ value in the plaque.

Histology

For analysis of atherosclerotic lesions in the ascending aorta, samples were harvested and fixed in Antigenfix (MicromMicrotech, France). The ascending aorta was then isolated, embedded in tissue medium (OCT Compound, Leica, Nanterre, France) and frozen on dry ice.

The samples were serially cut into 10μm sections, stained with Oil Red O (Merck, France) and then counterstained with hematoxylin (Labonord, Templemars, France) to identify the presence of atherosclerotic lesions. For immunohistochemical analysis, macrophages were detected with rat anti-mouse CD68 antibody (AbD Serotec, Düsseldorf, Germany). The sections were incubated 2 hours at room temperature with CD68 antibody (1:100) and revealed after incubation at room temperature for one hour, by a Cy3-labeled secondary antibody (1:200, Jackson IR, Suffolk, UK).

Images were acquired using an Olympus IX81 microscope coupled to a ColorviewII digital camera and analyzed with a Cell^F associated software (Olympus, France). The aortic wall areas were measured and expressed in mm². Macrophage content in aortic wall was determined after the analysis of the CD68 signal area (expressed in mm²).

Statistical Analysis

A second observer (EC, 10 years of experience) drew internal and external vessel wall contours for 8 randomly chosen animals. The variability for vessel wall area measurement was calculated with a paired two-tailed student's t test and reproducibility between observers was estimated by correlation coefficient and coefficient of variation. Correlation between MR measurements and plaque area quantification from Oil Red O stained histological slides was tested with Pearson's parametric test.

The temporal variation of the vessel wall areas and mean T2* values of plaques for both baseline and post-USPIO was analyzed with an ANOVA test on independent samples. When analyzing data from the same animals (N=10) investigated at each imaging time point an ANOVA on correlated samples was used. Student's t-test was used to assess the statistical significance of the differences between vessel wall areas and mean T2* values of the two groups. Differences were considered significant when $p<0.05$. Data are expressed as mean $\pm$ standard deviation (SD).

RESULTS

The images obtained from one animal (NTG) at the second imaging point and from one animal (TG) at the last point were judged not-analyzable owing to the presence of motion artifacts and were removed from the study.

Vessel wall area measured by MRI increased significantly over time for both the NTG ($p=0.001$) and the TG ($p=0.05$). No statistically significant difference was found between the

two groups. However, linear regression yielded a slope of vessel wall increase with time that was 1.8 times higher for the not treated group compared to the treated group.
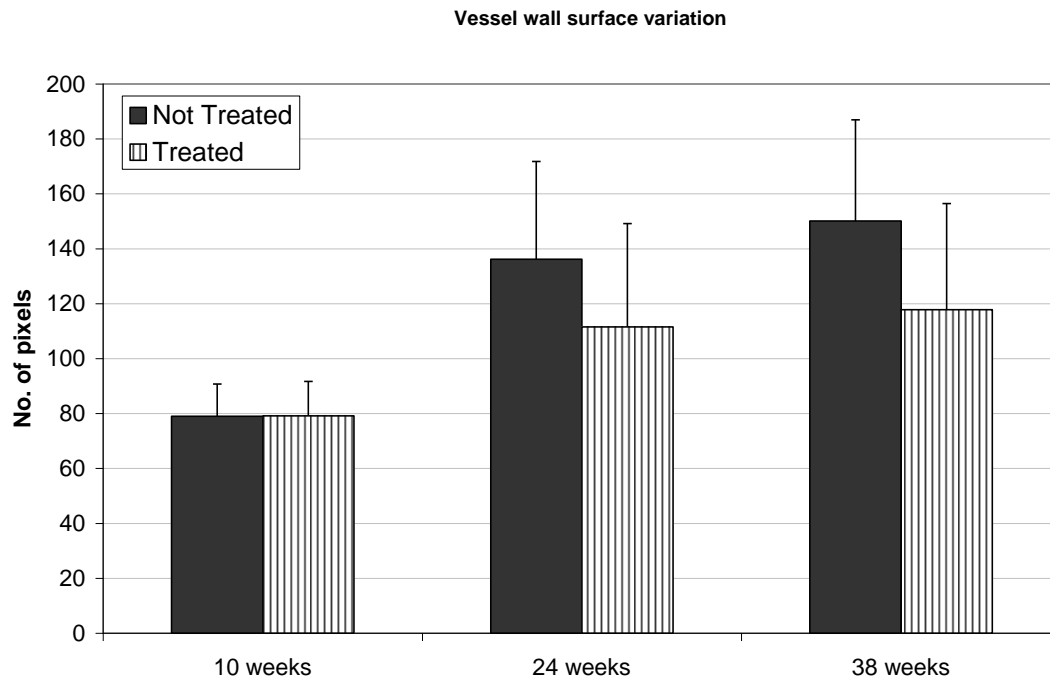
Vessel wall surface variation

Figure 1. *Temporal variation of the vessel wall surface (in number of pixels) for each investigated group. Data is presented as mean ± SD for all the investigated animals.*

A good and statistically significant correlation was found for vessel wall contouring between the two observers (r = 0.78, *p* < 0.001, CV = 2.87).

Figure 2 shows examples of calculated T2* maps overlaid on the MR T2*-w GE images (TE = 2.1 ms) acquired over the duration of the study on a not treated (left) and on a treated animal (right).

Mean T2* values obtained for all investigated animals are presented in Table 1. No statistically significant differences were found between groups at any time point, however significant decrease was obtained when comparing baseline to post-USPIO values for both groups (*p*<0.001).
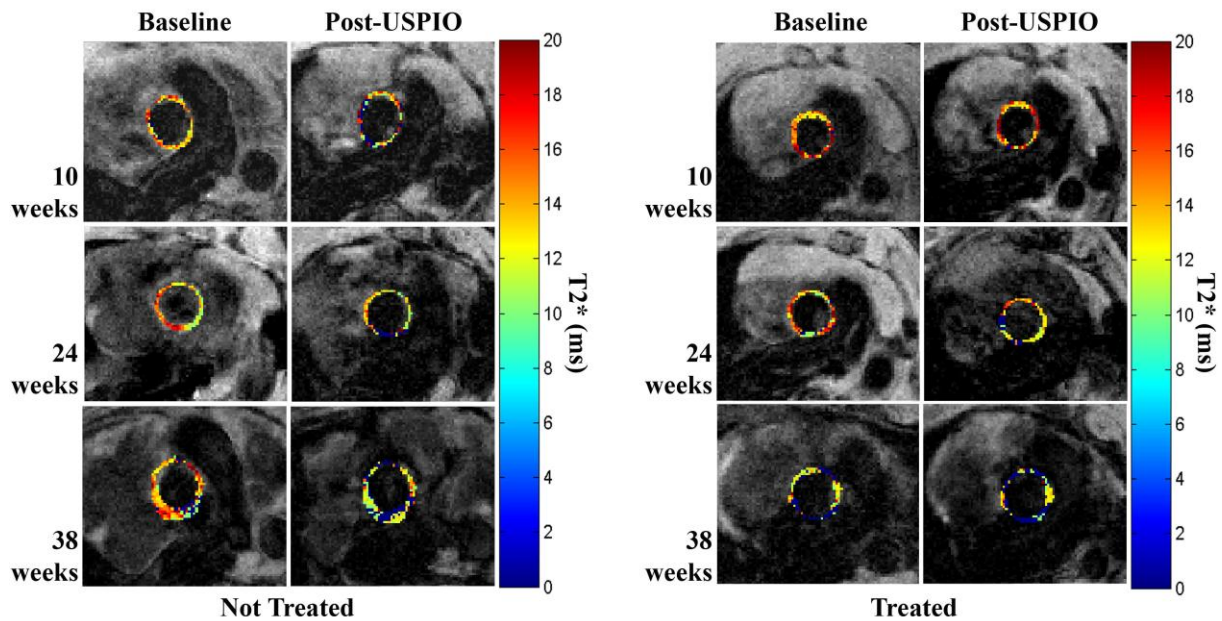
Figure 2. *Overlay of T2* maps of the ascending aorta on anatomic GE images acquired for one animal of the not treated group (NTG) (left) and one animal from the treated group (TG) (right) at every imaging time point. Maps were calculated from baseline and post-USPIO images. The colorbar represents T2* values in ms. T2* value of 0 indicates pixels that were poorly fitted, thus under the detection limit. (zoom x 3 on the MR images).*

Table 1. *Mean T2* values of the vessel wall calculated for each imaging time point*

Imaging time point		Not Treated	Treated
10 weeks	Baseline T2* (ms)	15±1	16±2
24 weeks		14±2	15±1
38 weeks		13±2	11±3
10 weeks	48h post-USPIO T2* (ms)	13±2	11±4
24 weeks		10±2	11±1
38 weeks		9±1	8±2

Drug evaluation performed on the same animals

Out of the 14 animals investigated by MRI at each point, 10 (N=5 treated and N=5 not treated) were the same throughout the study; Δ vessel wall surface between first and last imaging points and ΔT2* between baseline and post-USPIO were calculated for each of these animals. Mean values for the treated and not treated groups are presented in figure 4 A and B. The mean Δ surface in the TG was 44.7% lower than in the NTG, however not statistically

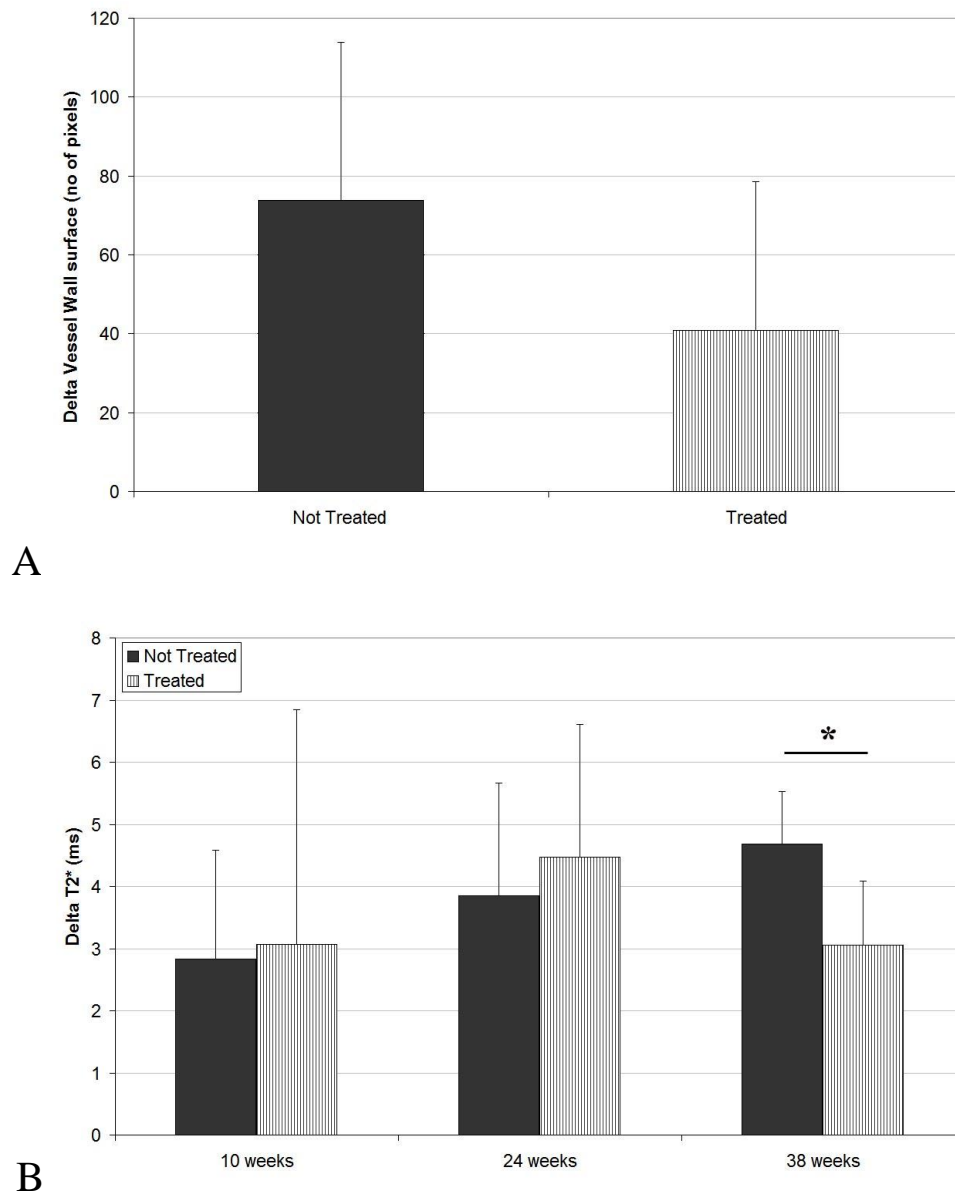significant. Furthermore, the TG showed significantly lower $\Delta T2*$ at the third point compared to the NTG.

A

B

Figure 4. *(A) Δ vessel wall surface (in number of pixels) between the first and the last point of investigation and (B) temporal variation of the $\Delta T2*$ values of the vessel wall between baseline and post-USPIO images. Data is presented as mean $\pm$ SD for the same 10 animals investigated throughout the study. (* - $p<0.05$)*

DISCUSSION

We report here the noninvasive assessment of the effect of an angiotensin inhibitor on the development of atherosclerosis in ApoE -/- mice by high resolution USPIO-enhanced MRI. It is, to our knowledge, the first MRI follow-up study performed on a mouse model of atherosclerosis with the goal of assessing a pharmaceutical effect.

A number of investigations pointed out that hypertension is associated with exaggerated atherosclerosis and that angiotensin (Ang) II infusion increases atherosclerosis and leads to the formation of abdominal aortic aneurysms in ApoE-/- mice (3, 4). Inversely, blocking the renin-angiotensin system (RAS) results in a decrease of atherosclerosis lesion formation and periadventitial inflammation in the same model (5).

The present study was performed on female ApoE -/- mice under a high cholesterol diet to which an angiotensin inhibitor was added or not. A clear tendency of reduced plaque formation was observed for the treated group compared to the not treated one. However a statistical significance was not obtained due to the high inter-individual variability. After 28 weeks of treatment (34 week old animals), the angiotensin inhibitor induced a 45% decrease of the mean vessel wall area compared to the not treated group.

Concerning USPIO-enhanced MRI, the study failed to obtain differences between groups based on the post-contrast plaque $T2^*$ values. A significant difference was found at the last imaging point (34 weeks) for Δ $T2^*$ values between the two groups (same investigated animals, $N = 10$). However, this finding cannot be directly related to a reduction in the number of resident macrophages because multiple injections were performed and permanence of iron particles at the lesion site cannot be excluded. Whether this is related to a lack of sensibility of the MR protocol or to the absence of a drug effect on the number of inflammatory cells remains to be confirmed by the histological analysis.

Literature data concerning RAS blockers seems to indicate that responses depend on age, sex, dose, duration of treatment, and site of lesion investigation (6). Thus a limitation of the current study is the fact that only one image of the ascending aorta just above the sinus was acquired, hence the obtained information may not be representative of the general effect of the drug.

In summary, the present study illustrates for the first time a noninvasive MRI follow-up using USPIO as a contrast agent to assess the effect of a therapeutic agent in a mouse model of atherosclerosis.

References:

1. Fukuda D, Sata M, Ishizaka N, et al. Critical role of bone marrow angiotensin II type 1 receptor in the pathogenesis of atherosclerosis in apolipoprotein E deficient mice. Arterioscler Thromb Vasc Biol 2008; 28:90-96.

2. Fukuda D, Enomoto S, Nagai R, et al. Inhibition of renin-angiotensin system attenuates periadventitial inflammation and reduces atherosclerotic lesion formation. Biomed Pharmacother 2009.

3. Mansard CD, Canet Soulas EP, Anwander A, et al. Quantification of multicontrast vascular MR images with NLSnake, an active contour model: in vitro validation and in vivo evaluation. Magn Reson Med 2004; 51:370-379.

4. Mazzolai L, Duchosal MA, Korber M, et al. Endogenous angiotensin II induces atherosclerotic plaque vulnerability and elicits a Th1 response in ApoE-/- mice. Hypertension 2004; 44:277-282.

5. Weiss D, Kools JJ, Taylor WR. Angiotensin II-induced hypertension accelerates the development of atherosclerosis in apoE-deficient mice. Circulation 2001; 103:448-454.

6. Zhou Y, Chen R, Catanzaro SE, et al. Differential effects of angiotensin II on atherogenesis at the aortic sinus and descending aorta of apolipoprotein-E-deficient mice. Am J Hypertens 2005; 18:486-492.

Annex Studies

Annex Study I

Dynamic M1 macrophages migration inside aortic atherosclerotic plaques: In vivo preclinical MRI study in ApoE2 Knock In mice

A.Bessaad, M. Sigovan, H. Alsaid, G. De Souza, N. Provost, Z. Majd, C.Menager, J .Honnorat, F. Lagarde, N.Nighoghossian, S. Nataf and E.Canet-Soulas

The MRI protocol developed and reported in manuscript four was used in a study of magnetically labelled cell tracking in atherosclerotic lesions. The purpose was to evaluate M1 macrophage recruitment in atherosclerosis after adoptive transfer of iron oxide-labelled macrophages in mice.

Anionic magnetic nanoparticles (AMNP) were chosen as the magnetic label because of their demonstrated good cell labeling properties. The particles had a mean diameter of 7.5 nm and bear negative charges due to carboxylate groups complexed on their surface.

A total of 19 ApoE2 ki (knock in) and 6 C57BL/6J mice were used for the follow-up MRI study. After a baseline imaging session, labelled cell suspensions (4×10^6 cells in 200 µL 0.9% NaCl solution) were injected in the retro-orbital sinus. The MRI protocol was repeated daily from day 1 to day 3 after cell administration. At the end of the MR follow up, animals were sacrificed and the aorta was removed for histology.

The presence of AMNP-labeled macrophages in lesions was determined as focal signal loss on post-injection images, using both GE and SE sequences. All injected mice showed localized signal loss in thickened vessel wall regions of the ascending aorta and the presence of iron- loaded M1 macrophages into aortic plaques was confirmed by Prussian blue staining and MHC-II IHC (Figure 1).
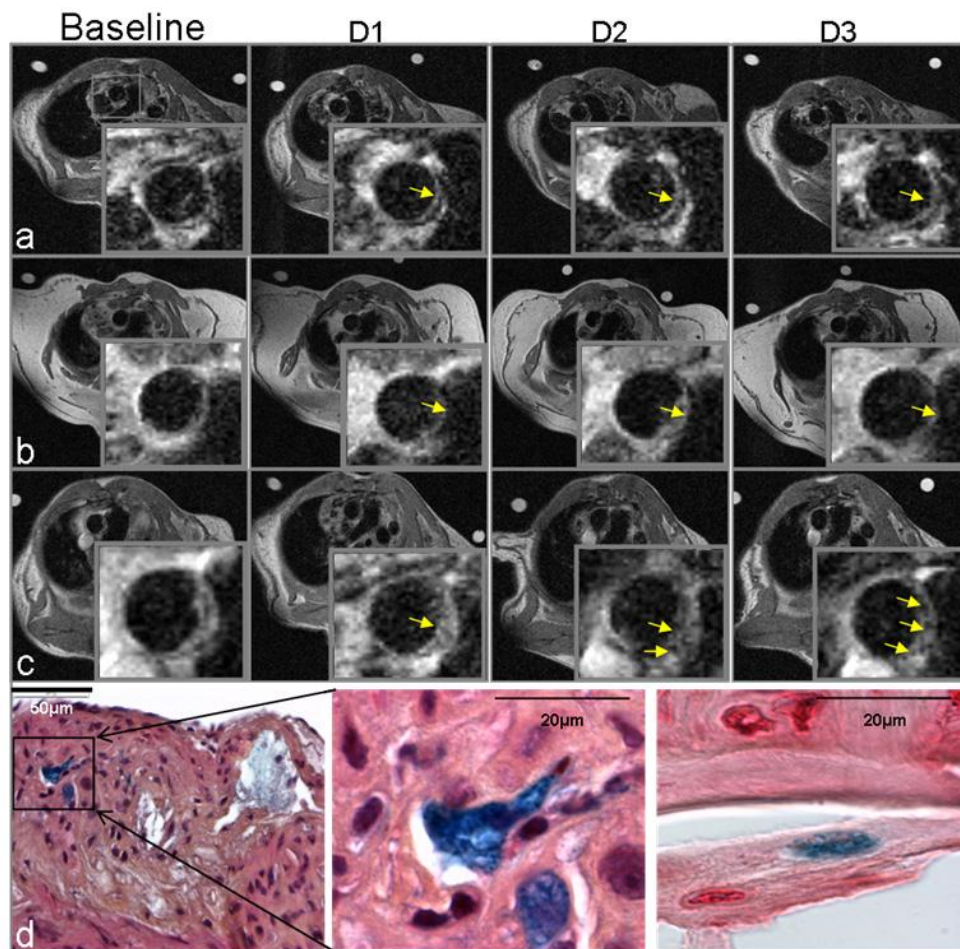
Figure 1*: High resolution proton density MRI in 3 ApoE2 ki mice (a, b, c) and histology (d). MRI follow-up from baseline to Day 3 (D1 to D3) after injection of AMNP-labelled macrophages showed post-injection focal signal loss inside the vessel wall (enlarged view in the insert, arrow head, a-c). Prussian blue alone (d, left) and coupled with MHC-II IHC (d, right) confirmed the presence of iron-positive cells inside the plaque and the co-localization of iron-loaded and MHC-II positive (i.e., M1 activated, d right) macrophages. (Reproduced with permission)*

With this study we have shown that is possible to track non- invasively by MRI the dynamic homing of magnetically labeled macrophages to the aortic atherosclerosis plaque. With the high spatial resolution of the MRI technique, topological evaluation of macrophage migration inside the plaque can be studied over time. This result opens a wide pre-clinical and clinical application field, like treatment monitoring by evaluating of the inflammation evolution in plaques.

Annex Study II

T2 and T2* mapping and clover leaf artifact volume for estimating the number of iron-labeled macrophages: murine in vivo testing

J.C. Brisset, <u>M. Sigovan</u>, A. Riou, F. Chauveau, E. Canet-Soulas, Y. Berthezene, and M. Wiart

The positive contrast sequence presented in the first study did not seem to be adapted for *in vivo* imaging of atherosclerosis in our experimental conditions. It has been however successfully applied for a quantification trial of magnetically labeled cells *in vivo* in the mouse brain.
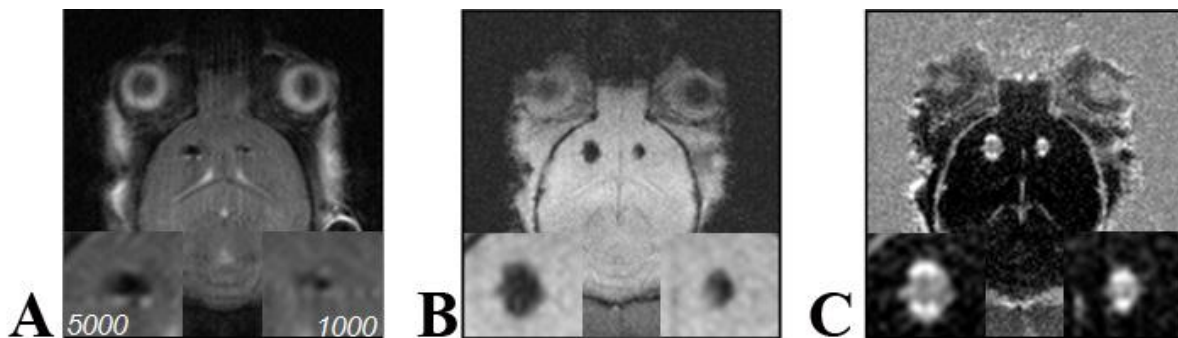

Figure 2. *Size and shape of susceptibility artefacts induced by labelled macrophages administered by local injection in the mouse brain. Images acquired with a spin echo (A) a gradient echo (C) and a positive contrast sequence (C). Insets represent magnified images of the injection regions. Number of injected cells is given on the spin echo image. (Modified with permission)*

It was chosen in this study as it offers a better contrast for labeled cell visualization. As it was concluded at the end of the first study presented in this thesis, the gradient compensation sequence should be used with two symmetric (positive and negative) gradient amplitudes since only one part of the dipolar field is refocused at one time. This was done in the present study and a post-processing method was used for the two positive contrast images that enabled visualization of the entire dipolar field. Furthermore it was observed that the size of the dipolar field was linearly correlated to the number of injected cells.

Annex Study III

Modified Electrocardiograph-Triggered Black-Blood Turbo Spin-Echo Technique to Improve T1-Weighting in Contrast-Enhanced MRI of Atherosclerotic Carotid Arteries

Loic Boussel, MD, Gwenael Herigault, PhD, Monica Sigovan, MSc, Romaric Loffroy, MD, Emmanuelle Canet-Soulas, DVM, PhD, and Philippe Charles Douek, MD, PhD

In collaboration with the Radiology Department of the Cardiology Hospital of Lyon, a patient study was performed on a 1.5T Philips scanner (Intera®; Philips Medical Systems, Best, The Netherlands).

The purpose of the study was to assess the efficacy of a modified electrocardiograph (EKG)-triggered black-blood T1 weighted (T1-w) spin-echo sequence in improving contrast on post-gadolinium high resolution carotid plaque imaging by implementing heart rate–independent contrast preparation.

A standard EKG-triggered double inversion-recovery (DIR) turbo spin-echo (TSE) sequence was modified with the addition of an extra saturation (90°) radio frequency (RF) pulse placed immediately after the DIR module, shortening the repetition time to a fixed value of 400 msec. The extra RF pulse was a 2-msec nonselective 90°, three-lobe, sinc-Gauss shaped pulse, followed by crusher gradients to prevent unwanted stimulated echoes. Postinjection intraplaque contrast measurements with both the standard and the modified sequence were performed on a total of 10 patients with atherosclerotic disease. The intraplaque contrast between low and high intraplaque signal areas was defined as:

$$C = \frac{SI(High) - SI(Low)}{SI(High)} * 100$$

where *SI(High)* and *SI(Low)* are the mean value of the highest and lowest signal areas in the plaque for the two observers, respectively.
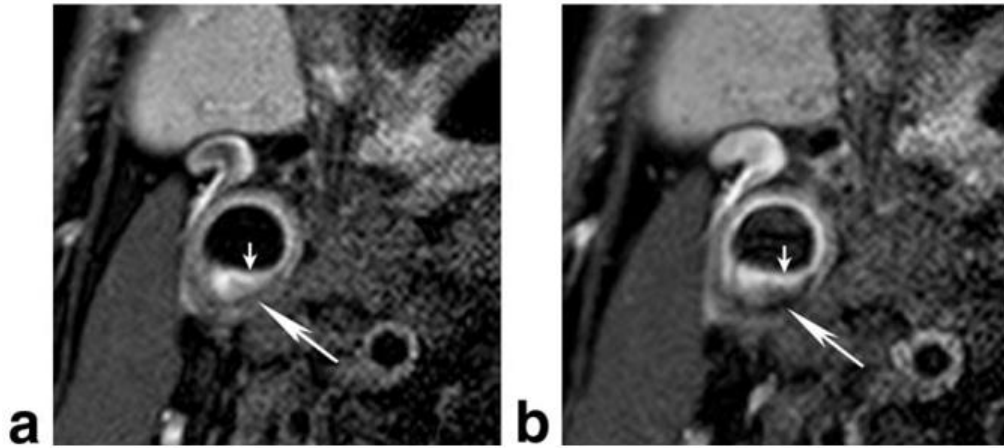
Figure 3. Comparison between the standard black-blood T1W TSE (a) and modified black-blood T1W TSE techniques (b) showing better intraplaque contrast between lipid core (large arrow) and the fibrous cap (small arrow) with the modified sequence. (Reproduced with permission)

Significant contrast enhancement of 13.6% (P < 0.001) was obtained for post-gadolinium-injection intraplaque contrast from $31.7 \pm 12.8\%$ with the standard T1W sequence (nT1-TSE) to $45.3 \pm 17.2\%$ with the modified T1W sequence (mT1-TSE). An exemple of contrast enhancement between plaque components with the modified sequence is presented in figure 3.

The addition of a RF pulse to the standard EKG-triggered T1W TSE sequence increased intra-plaque contrast without increasing sequence acquisition time. Furthermore, it appeared to be a robust technique, easy to implement on clinical scanners. The interest of a heart rate-independent sequence could be imagined in follow-up studies of patients with arrhythmia or for multicenter trials.

Discussion and Conclusions

Cardiovascular diseases represent the main cause of death in industrialized countries. Atherosclerosis is a complex arterial disease that induces changes of the vessel wall; its development involves inflammation as a central parameter. Detecting inflammation *in vivo* becomes thus essential for diagnosis and therapeutic follow up.

Given its characteristics in relations to other imaging techniques, magnetic resonance imaging (MRI) is one of the preferred methods for non invasive cardiovascular investigations. MRI offers a 3-dimensional (3D) anatomic view of the cardiovascular system with a small field of view and an excellent spatial and temporal resolution. This is achieved by technologic advances in imaging and gating systems and the development of fast imaging sequences. In addition, MRI offers a molecular and functional approach to imaging with the use of non-targeted and targeted contrast agents.

Cardiovascular research is oriented toward improving clinical patient care. In this regard, the aim of numerous specific preclinical studies, performed on animal models, is the development and the evaluation of novel contrast and pharmaceutical agents. The work presented here integrates this concept by proposing dedicated imaging methods for contrast enhanced MR.

Contrast media is used in 30% of all MRI procedures with a dominance of gadolinium (Gd) based agents. However, after their development, superparamagnetic iron oxide contrast agents ((U)SPIO) have been the subject of intensive research and opened up a new field in MRI. They have several advantages over Gd-based agents: no long term toxicity for the biodegradable particles, higher relaxivity effects and prolonged circulation time that enables the use of high resolution T1-w sequences.

A functional approach for atherosclerosis plaque characterization is the intravenous administration of (U)SPIO agents. They have been the subject of intensive research during the past decade owing to their intrinsic properties. As they are rapidly taken up by macrophages, in spleen and liver, but also in areas of active inflammation, they are often described as contrast agents for "inflammation imaging". Since the overall objective of this thesis was the *in vivo* evaluation of inflammation in atherosclerosis we reported methodological studies for USPIO detection (positive contrast imaging) and quantification (T2* measurements) followed by their application to animal models.

The coating material plays a major role in the biodistribution of nanoparticles. As was seen in the study presented in chapter IV of this thesis, a rapid-clearance USPIO with specific coating properties is efficiently accumulated in induced inflammatory aortic lesions in a rabbit model of atherosclerosis. One would think that a fast elimination from blood is incompatible

with effective vascular inflammation detection. However, we have demonstrated that P904 is accumulated in high concentrations (mean values around 6 µMFe/g of tissue for an injected dose of 1000µM) and it enables an earlier post-contrast imaging window compared to a standard clinically used USPIO (Ferumoxtran-10, Sinerem®, Guerbet, Paris, France).

Superparamagnetic contrast agents decrease the relaxation time of the surrounding water protons creating strong contrast changes on the MR images, owing to their high magnetic moment that is induced in the presence of an external magnetic field. The method of choice for their detection was gradient echo (GE) imaging given its inherent sensitivity to magnetic field variations induced by relatively high concentrations of particles. Voxels neighbouring superparamagnetic particles appear as signal loss regions on a GE T2*-weighted images. Two strategies based on GE sequences have been explored for iron oxide based contrast agent detection: one is the standard negative contrast of T2*-w images that can be combined with quantitative MR to measure T2* (the apparent transverse relaxation time) and the other is the use of 'positive contrast' techniques, imaging methods that allow the selective recovery of signal loss from the voxels surrounding magnetic particles. The later techniques offer a new type of contrast, based on the susceptibility effects. Their importance is the potential improvement of iron detection sensitivity compared to standard T2* methods of negative contrast.

The implementation of the gradient compensation sequence on small animal scanners and its application for different biological applications were presented in this thesis. Firstly the sequence was used for the detection of non-radioactive superparamagnetic nano-capsules designed for brachy-therapy. This is a novel product, developed at the LAGEP Laboratory (Laboratoire d'Automatique et de Génie des Procédés) of Lyon1 University, that consists of magnetite crystals, with a 12 nm size conferring superparamagnetic behavior, incorporated as a complex with oleic acid in a PLLA (poly L-lactic acid) polymer matrix containing non-radioactive [185-187]dirhenium decacarbonyl [$Re_2(CO)_{10}$]. MRI represents the only imaging technique that can be applied for delivery validation before radio activation in a neutron flux.

In vitro study performed on a series of concentrations showed that contrast enhancement on the negative contrast reached saturation for iron concentrations around 1mM. *In vivo* the positive contrast technique allowed a three day follow up of particles. Furthermore, it showed a different contrast variation with time compared to the standard negative contrast. This indicates a potential higher specificity to particle visualisation as signal loss on negative contrast images may be due to additional sources. We are currently

looking into MR simulation techniques to estimate positive contrast signature of a given iron material, to simulate contrast effects of endogenous iron (i.e. local haemorrhage) versus the injected iron nanocapsules. The goal is to be able to differentiate between different contrast sources.

The gradient compensation technique was then tested for the *in vivo* detection of USPIO accumulation in a mouse model of atherosclerosis (this data was not presented). It proved inefficient in this application due to several reasons related to the anatomical region investigated, the aortic arch. The gradient compensation is based on refocusing spins surrounding the region where magnetic particles are accumulated. Thus the failure of the sequence is most certainly due to the fact that the vessel wall is a moving thin structure (80 µm for normal aorta) surrounded by very heterogeneous regions, with high blood flow. In some cases bright signal regions were obtained, however it was unclear whether they were related to the presence of iron or to blood flow artifacts.

A study performed in our laboratory where the positive contrast sequence was used, showed that it can be efficiently applied for magnetically labeled cell detection in the mouse brain. Furthermore, the area of the bright blood was correlated to the number of labeled cells locally injected into the brain. This represents a first step for quantification essays using positive contrast sequences. However the debate between analyzing area of bright signal or the signal intensity remains open. During sequence implementation in the *in vitro* study (chapter III) we found that high iron concentrations that lead to complete signal loss on negative contrast did not induce a saturation of the positive contrast. However, direct proportionality between signal intensity and concentration was not obtained.

USPIO are now established markers of macrophages in atherosclerosis. It should be stated here that similar to macrophages, the superparamagnetic particles accumulate predominantly in ruptured and rupture-prone lesions. Thus their potential clinical application would be to enable *in vivo* differentiation between low- and high-risk plaques. Several methods are currently being used in scientific literature for assessing iron accumulation *in vivo* on T2*-w gradient echo images. One is the measurement of the spatial extent (in number of pixels with signal loss) of the susceptibility artifact and the other is contrast enhancement measurements.

We have seen that high iron concentrations lead to saturation of the contrast effect. In chapter IV, a logarithmic relationship was found between the number of pixels with signal loss and iron concentration measured by ICP-AES. For high iron concentrations the number

of pixels reached a plateau. To avoid this, shorter echo times should be used. However, this offers only one piece of the whole picture. The need for quantitative MR techniques becomes thus obvious for a more reliable assessment of concentrations and as stated through out this work, it is one of the main goals in today's research because it will lead to the improvement of the diagnosis value of (U)SPIO agents.

Iron concentration estimation is possible *in vivo* using non-invasive MRI methods in certain pathologies characterized by endogenous iron overload in specific organs like the liver and the heart (1-3). MR quantification techniques are well established in this field and iron calibration curves are used for clinical diagnosis and follow-up in these pathologies. The transfer of these quantitative techniques to (U)SPIO-enhanced MRI has been considered by several authors. *In vitro* studies performed on phantoms containing dispersions of free particles or magnetically labeled cells have shown good correlation between the measured MR parameters (T2/T2*) and number of cells or iron concentration (4, 5). However these studies have been performed on very low concentrations (generally lower than 1 mM Fe)

The *in vitro* quantification assay presented in chapter II was performed on a wide range of iron concentrations of the USPIO agent P904 because these concentrations would be expected *in vivo* in atherosclerosis (6). The purpose was contrast agent quantification based on its susceptibility effect in its free state and aggregated inside macrophages. A partial Fourier method was chosen to decrease the first available TE that enabled detection of high concentrations of up to 8.55 mM Fe. A field independent linear increase of 1/T2* was found with the increase of contrast agent concentration. Our results are in agreement with results by Brisset et al. that show similar values of r2* of free particles (Ferumoxtran-10, Sinerem® Guerbet, Paris, France) between 4.7 and 7T (4). Intra-cellular aggregation resulted in a ~3.5 fold decrease of T2* for similar concentration intervals.

The obtained calibration curves for the T2* values of P904 can not be applied directly *in vivo* since a mixture of extracellular particles and aggregated inside cells is present, as discussed in the contrast agent theory chapter. It has been shown by Clark et al. that in the cases where there is compartmentalization of the transverse relaxation a multi-exponential analysis of the transverse magnetization decay is needed for an accurate quantification of proton transverse relaxation processes (7). A perspective for the study discussed above is considered in this direction. Data would have to be acquired in the same experimental conditions for phantoms containing a mixture of different fractions of free particles and magnetically labeled cells. Using the information previously obtained for free particles fitting

of the data would be performed using a bi-exponential equation. This study should improve iron concentration estimations for *in vivo* studies.

When trying to implement quantification methods developed *in vitro* to atherosclerosis one is faced with technical difficulties mainly related to the duration of the MR investigation, even more when gating of the acquisition is needed. We have applied T2* quantification to characterize the macrophage accumulation related to atherosclerosis lesion progression in ApoE$^{-/-}$ mice (chapter V) using USPIO-enhanced MRI. We reported the first T2* measurements *in vivo* in mice. Signal loss regions in the vessel wall were correlated to macrophage areas on histology slides. The significant differences between the calculated mean T2* values of the vessel wall indicated that the peak iron particle uptake in this mouse model is induced after 10 to 18 weeks of high cholesterol. One limitation for the quantification measurements was the minimum TE (5 ms) imposed by the chosen spatial resolution used for the GE acquisitions. This limits the T2* that can be measured. To compensate for this, a condition was set for the goodness of fit during the T2* calculations and only pixels with a T2* equal or higher than 1 ms were taken into account.

The advances in knowledge and the developed tools in our previous work allowed us to perform a drug evaluation study. The last chapter presents this follow up study, carried out at higher field strength (7T) on the same animal model and using the same contrast agent. To improve T2* quantification with respect to the above mentioned study, we used a partial Fourier acquisition that shortened the echo time to 2.1 ms. Another improvement in this technique of T2* mapping for post-USPIO MRI would be to use ultra short echo time sequences (UTE). However, certain limitations need to be overcome in order to successfully apply UTE to plaque imaging, especially the spatial resolution, essential in vessel wall imaging. A recently developed spin echo based technique allows the measurement of very short T2* of species with relatively long T2, adapted for magnetically labeled cell imaging. However, the long scan time is not compatible with *in vivo* applications.

In vivo quantification remains a challenge because of the non-linear effects of T1 and T2/T2* of particles accumulated in tissue (8). Cell aggregation and concentration redistribution will lead to estimation errors. Gathering more knowledge on the effects of (U)SPIO on the MR signal will lead to the improvement of dedicated imaging techniques. Furthermore, ongoing research on macrophage trafficking and polarisation inside

atherosclerotic lesions will provide more insight for new combined imaging and therapeutic strategies.

References

1. Clark PR, St Pierre TG. Quantitative mapping of transverse relaxivity (1/T(2)) in hepatic iron overload: a single spin-echo imaging methodology. Magn Reson Imaging 2000; 18:431-438.

2. St Pierre TG, Clark PR, Chua-Anusorn W. Measurement and mapping of liver iron concentrations using magnetic resonance imaging. Ann N Y Acad Sci 2005; 1054:379-385.

3. Wood JC, Enriquez C, Ghugre N, et al. MRI R2 and R2* mapping accurately estimates hepatic iron concentration in transfusion-dependent thalassemia and sickle cell disease patients. Blood 2005; 106:1460-1465.

4. Brisset JC, Desestret V, Marcellino S, et al. Quantitative effects of cell internalization of two types of ultrasmall superparamagnetic iron oxide nanoparticles at 4.7 T and 7 T. Eur Radiol 2009.

5. Kuhlpeter R, Dahnke H, Matuszewski L, et al. R2 and R2* mapping for sensing cell-bound superparamagnetic nanoparticles: in vitro and murine in vivo testing. Radiology 2007; 245:449-457.

6. Sigovan M, Boussel L, Sulaiman A, et al. Rapid-clearance iron nanoparticles for inflammation imaging of atherosclerotic plaque: initial experience in animal model. Radiology 2009; 252:401-409.

7. Clark PR, Chua-Anusorn W, St Pierre TG. Proton transverse relaxation rate (R2) images of liver tissue; mapping local tissue iron concentrations with MRI [corrected]. Magn Reson Med 2003; 49:572-575.

8. Bjornerud A, Johansson L. The utility of superparamagnetic contrast agents in MRI: theoretical consideration and applications in the cardiovascular system. NMR Biomed 2004; 17:465-477.

Publications and Communications

Articles in Journals

1.   Rapid-Clearance Iron Nanoparticles for Inflammation Imaging in Atherosclerotic Plaque: Initial Experience in Animal Model
M. Sigovan, L. Boussel, A. Sulaiman, D. Sappey-Marinier, H. Alsaid, C. Desbleds-Mansard, D. Ibarrola, D. Gamondes, C. Corot, E. Lancelot, J-S. Raynaud, X. Violas, P. Douek, E. Canet-Soulas
Radiology. 2009 Aug;252(2):401-9.

2.   Assessment of age modulated vascular inflammation in ApoE-/- mice by USPIO-enhanced MRI
Monica Sigovan, Amine Bessaad, Hasan Alsaid, Claire Corot, Bruno Neyran, Magalie Breisse, Nicolas Provost, Zouher Majd, Emmanuelle Canet-Soulas
Submitted in Investigative Radiology

3.   Positive contrast with therapeutic iron nanoparticles at 4.7T
M. Sigovan, M. Hamoudeh, A. Al Faraj, H. Fessi, E. Canet-Soulas
To be submitted in European Radiology

4.   Dynamic M1 macrophages migration inside aortic atherosclerotic plaques: In vivo preclinical MRI study in ApoE2 Knock In mice
A.Bessaad, M. Sigovan, H. Alsaid, G. De Souza, N. Provost, Z. Majd, C.Menager, J .Honnorat, F. Lagarde, N.Nighoghossian, S. Nataf and E.Canet-Soulas
Submitted in Investigative Radiology

5.   Modified electrocardiograph-triggered black-blood turbo spin-echo technique to improve T1-weighting in contrast-enhanced MRI of atherosclerotic carotid arteries.
L. Boussel, G. Herigault, M. Sigovan, R. Loffroy, E. Canet-Soulas, PC Douek
J Magn Reson Imaging. 2008 Aug;28(2):533-7

International Conference Proceedings

1.   Assessment of age modulated vascular inflammation in ApoE-/- mice by USPIO-enhanced MRI
<u>Monica Sigovan</u>, Amine Bessaad, Hasan Alsaid, Eric Lancelot, Claire Corot, Bruno Neyran, Nicolas Provost, Zouher Majd, Magali Breisse, Emmanuelle Canet-Soulas
Contrast Media Research Meeting, Copenhagen, Denmark, 2009 [O]

2.   MRI Simulation Framework for Atherosclerosis Inflammation with USPIOs.
O. Addy, D. Charpigny, <u>M. Sigovan</u>, E. Canet-Soulas, H. Benoit-Cattin, D. Nishimura
In Proc. EMIM 2009: 4th European Society for Molecular Imaging, 2009. [P]

3.   Comparison of USPIO-enhanced MRI and magnetically labeled cell tracking for Inflammation detection in ApoE mice
<u>M. Sigovan</u>, A. Bessaad, H. Alsaid, G. De Souza, C. Corot, N. Provost, Z. Majd, C. Menager, N. Nighoghossian, S. Nataf, E. Canet-Soulas
17th International Society for Magnetic Resonance in Medicine, #1837, Honolulu, Hawaii, USA: April 18-24, 2009. [P]

4.   Inflammation Imaging of Atherosclerosis Tracking of Iron Oxide-Labeled Macrophages in ApoE2 (KI) Mice
A. Bessaad, <u>M. Sigovan,</u> H. Alsaid, G. De Souza, N. Provost, Z. Majd, C.Menager, N. Nighoghossian, S. Nataf, E.Canet-Soulas
17th International Society for Magnetic Resonance in Medicine, #926, Honolulu, Hawaii, USA: April 18-24, 2009. [P]

5.   Pulmonary Perfusion-Weighted Regional Measurements in Mouse – Primarily Results
Magdalena Zurek, Katarzyna Cieslar, <u>Monica Sigovan</u>, Amine Bessaad, Emmanuelle Canet-Soulas, Yannick Crémillieux
17th International Society for Magnetic Resonance in Medicine, #2005, Honolulu, Hawaii, USA: April 18-24, 2009. [P]

6.   Positive Contrast with Therapeutic Iron Nanoparticles at 4.7T.
<u>M. Sigovan</u>, M. Hamoudeh, A. Al Faraj, H. Fessi et E. Canet-Soulas
The European Conference on Contrast Agent Science - EMRF, Valencia, Spain 2008. [O]

7.   In-vivo USPIO's follow-up and optimized MRI protocol for Inflammation Imaging in Atherosclerotic Plaques
<u>M. Sigovan</u>, L. Boussel, A. Sulaiman, D. Sappey-Marinier, C. Desbleds-Mansard, D. Ibarrola, D. Gamondes, C. Corot, E. Lancelot, J-S. Raynaud, X. Violas, P. Douek and E. Canet-Soulas
Contrast Media Research - CMR*, Banff, Canada, 2007.* . [O]

National Conferences and Meetings

1. IRM de l'inflammation vasculaire avec un USPIO à pharmacocinétique rapide
M. Sigovan, L. Boussel, A. Sulaiman, D. Sappey-Marinier, H. Alsaid, C. Desbleds-Mansard, D. Ibarrola, D. Gamondes, C. Corot, E. Lancelot, J-S. Raynaud, X. Violas, P. Douek, E. Canet-Soulas
12ème Congrès du GRAMM, Lyon, France 2008. [O]

2. Suivi in vivo avec les nanoparticules de fer par le contraste positif à haut champ
M. Sigovan, M. Hamoudeh, A. Al Faraj, H. Fessi, E. Canet-Soulas
JRIM, Dijon, France 2007. [O]

3. Evaluation de l'inflammation vasculaire chez la souris ApoE par IRM post USPIO
M. Sigovan, A. Bessaad, H. Alsaid, C. Corot, N. Provost, Z. Majd, M. Breisse, E. Canet-Soulas
RITS, Lille, France 2009. [O]

4. Cartographie R2* in vitro d'un USPIO à 1.5T, 3T et 7T
M. Sigovan, E. Kaye, M. Alley, K. Butts Pauly, E. Canet-Soulas
RITS, Lille, France 2009. [P]

[O]: oral communication; [P]: poster presentation